MEASUREMENT OF COMBUSTION AIR FLOW INTO BURNERS IN COAL FIRED PLANTS

Submitted by

Gladwell Sizwe Manqele

Student number: 919004

School of Mechanical, Industrial and Aeronautical Engineering

In partial fulfillment of the requirements of the degree of Master of Science (MSc)

University of Witwatersrand

Johannesburg, South Africa

October 2024

DECLARATION

I declare that this research report is my own, unaided work except where otherwise acknowledged. The research report is submitted for a Master of Science degree (MSc) in Mechanical Engineering to the University of Witwatersrand in Johannesburg, South Africa. It has not been submitted before for any degree or examination at other institutions.

Signed this 10th October 2024.

Sizwe Manqele

ACKNOWLEDGEMENTS

I would like to thank my supervisors Prof Walter Schmitz, Mr. Reshendren Naidoo, as well as their assistant, Mr. Ayodimeji Biobaku for their unrelenting support, expert advice, guidance, and encouragement throughout the research study. It truly is an honor and a privilege to have worked under your guidance and supervision. Thank you for sharing your immense wisdom with me.

I express my gratitude to Mr. Shaun Riekert, Mr. Mabudulle Norman Kgasago, Mr. Andrew Heydenrych, Mr. Zwavho Netshisaulu, Mr. Venondran Parumal, Mr. Klass Paka, Mr. Peter Radebe, and Mr. Adam Ndhlovu; all from the Mechanical Engineering Laboratory at the University of Witwatersrand. Thank you for your time, expert technical skills, and technical support. Your valuable input eased the research study and made it possible. Thank you.

I would like to thank my industrial supervisor Mr. Ivan Hartman and Mr. Jan-Louis Human. You made this study possible. Thank you.

Further thanks to my colleagues Mr. Sibonelo Nzama, Mrs. Faith Mokhonoana, Mr. Riaz Vajeth, Mr. Neo Ramonyalioa, Mr. Timothy Sibi, Dr Bertie Jacobs, Mrs. Mantu Mamashela and Mr. Mduduzi Mthethwa. Thank you for your support, understanding and encouragement throughout the study.

Thank you to my friend Mr. Percy Dube for supporting and encouraging me throughout the research study. Thanks buddy, you are the best.

Finally, I would like to thank my family for their consistent understanding, patience, and support during the research study. Thank you, you made it possible.

ABSTRACT

This research study is aimed at achieving accurate measurement of mass flow rates in large square industrial square ducts at Eskom's boiler plants. For safe and efficient operation of Fossil Fuel Firing Boiler Plants, the utility has put in place the Fossil Fuel Firing Regulation Standard which requires that the Total Combustion Air flow be measured at exit from the air heaters, into the ducts.

In this study, a sophisticated airflow measuring probe was acquired, herein the current study referred to the 14-hole Omniprobe. The accuracy was found to be within 5% in a free stream flow field. A Five-hole probe was calibrated in the free-stream wind tunnel. The calibration process enabled the derivation of the probe specific polynomials of Pitch, Yaw, Total Pressure, Static Pressure coefficients and velocity components.

A prototype air duct was designed for the study to simulate air flow through square ducts with a 90º bend as an abrupt flow disturbance. To achieve the objectives of the study, 6 planes were identified where air flow velocity profiles were generated using the equal area method. The modeling of the velocity profiles was conducted numerically, using CFD (Ansys Fluent), and experimental, using Pitot-static probe, Omniprobe, and a Five-hole probe.

The mass flow rates as measured by the Pitot-static tube were found to be consistent at planes 1, 2, 5, and 6. The mass flow rate as calculated from the Pitot-static probe varied by 2.1% through the duct. This justified the selection of the Pitot-static probe as the reference for this study. The velocity profiles generated from the traverse measurements using the 14-hole Omniprobe showed an error in velocity measurements which are in the proximity of the wall. This can be attributed to the the wall effect. The mass flow rates of air calculated from the Five-hole probe measurements were found to be within 4% of the mass flow rate as calculated from the results of the reference probe in the 1^{st} and 2^{nd} planes upstream of the bend. After the 90º flow disturbance bend, the accuracy drops to 13% at plane 5 and improved slightly at plane 6 to 11.7%. This is attributed to complex flow pattern at these planes.

The study concludes that the Pitot-static tube remains the preferred instrument for use in measuring flow rates using the equal area method in large square ducts. The Five-hole probe can be applied where the flow field is not distorted in conjunction with CFD. The Omniprobe's accuracy in measuring the velocity magnitude, and the angularity of the flow field was verified in an open stream wind tunnel. This study recommends exploring the use of an L-type 14-hole Omniprobe for application in large square industrial ducts.

TABLE OF Contents

TABLE OF FIGURES

LIST OF TABLES

1. INTRODUCTION

Eskom, a South African power utility supplies about 90% of South Africa's electricity and generates about 30% of electricity used in the Africa [1,2]. The utility uses various technologies to generate electricity to meet demand, the combination of which is called plant mix.

At the heart of the Eskom's plant mix are thermal power stations, fueled by coal which make up the largest portion of the utility's plant mix. The utility's generation division has 15 coal-fired power stations with an installed capacity of 44 602 MW of power [2]. Majority of these coal-fired stations are composed of six generating units with each generating unit comprising of a boiler, turbine, generator and auxiliary systems [2].

The utility's coal fired power plant operation is based on Rankine Cycle. Figure 1 illustrates a typical arrangement of a coal-fired power plant where electricity is produced by burning coal in a boiler to transform water to steam at a high temperature and pressure. The heat energy contained in the steam drives the turbine, converting heat energy into mechanical energy. The shaft of the turbine is coupled to that of the generator therefore spinning the rotor in a stator to produce electrical energy as per Faraday's law of electromagnetic induction [3].

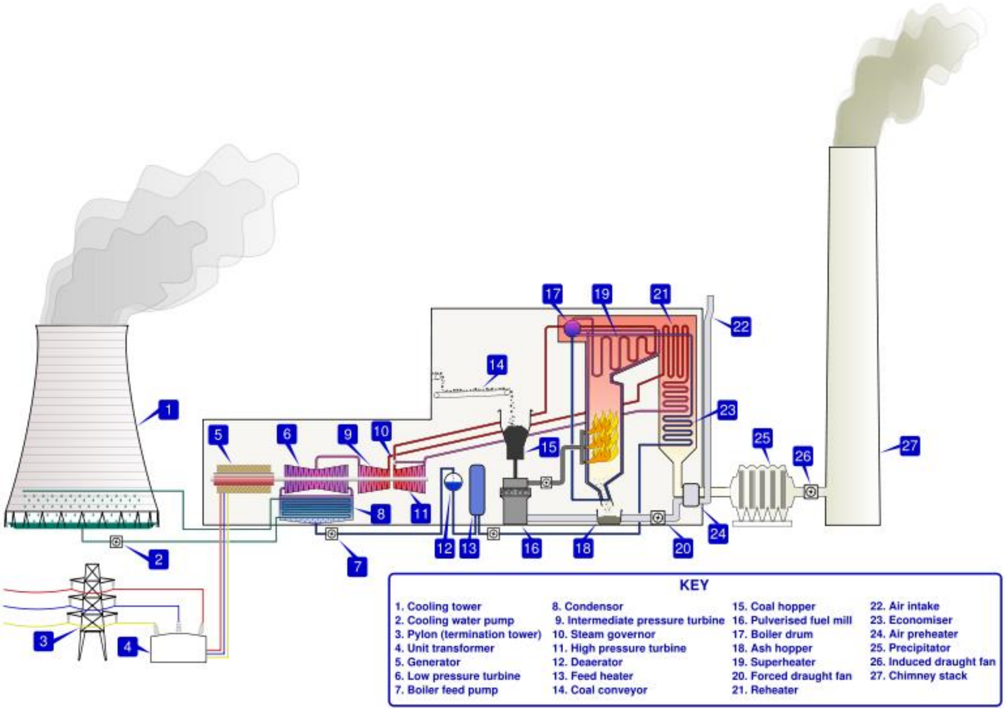

Figure 1: Thermal power plant [4]

2. RESEARCH BACKGROUND

With the transition to cleaner energy, adaptation of thermal power plants is required to reduce impact on the environment. Though reliable and efficient, coal-fired power plants are a major source of air polluting gases such as sulfur dioxide, nitrogen oxides, and greenhouse gases like carbon dioxide. These gases are products of combustion of fossil fuels and are emitted directly into the air.

Hydrocarbons are primary constituents of fossil fuels namely natural gas, petroleum, and coal. NASA's Glenn Research Center defines combustion as a chemical process in which a fuel reacts rapidly with oxygen in air and gives off heat energy [5].

In the context of coal-fired power station, coal is a fossil fuel that reacts with oxygen in air resulting in the generation of heat. The heat generated efficiently converts water to steam which at high temperature and pressure drives the turbine. Combustion and the conversion of water to steam takes place inside the boiler [4].

During complete combustion of pure fossil fuels, the products are water (H_2O) and carbon dioxide (CO_2). However, in practice fossil fuels are not pure hydrocarbons but contain substances nitrogen, sulfur, oxygen and minerals. During combustion, new chemical substances are formed, and these are called exhaust. When a hydrocarbon-based fossil fuel like coal burns, the exhaust includes water, carbon dioxide, carbon monoxide, sulfur dioxide, and nitrous oxide also known as NO_X [4].

Incomplete combustion occurs when insufficient oxygen is supplied to the boiler. The presence of carbon monoxide in the exhaust indicates incomplete combustion. The nitrogen in nitrous oxide (NO_x) results from the nitrogen in air which does not take part in combustion and excess oxygen from excess air. The nitrogen yields nitrogen dioxide (NO_2) and nitric oxide (NO) and sulfur yields sulfur dioxide (SO_2). To adhere to regulation, utilities strive to reduce carbon emissions as best as possible [6].

The three elements required for combustion to take place are fuel, air and heat. Inadequate air supply to the boiler may lead to boiler explosion and poor combustion. It is desirable by utilities to achieve good combustion, to achieve proper combustion of fuel elements, calculated excess air is often supplied into the boiler through air ducts. To achieve proper mixing of air and fuel, the boiler requires draught which is a pressure difference necessary to draw the required quantity of air into the boiler and to remove flue/exhaust gases via chimneys/stack [7].

Figure 2 illustrates a draught plant where combustion air is drawn from the atmosphere by means of forced draught fans, forced through large industrial ducts, air heaters and into the boiler. Induced draught fans draw exhaust gases and emit through the stack [11].

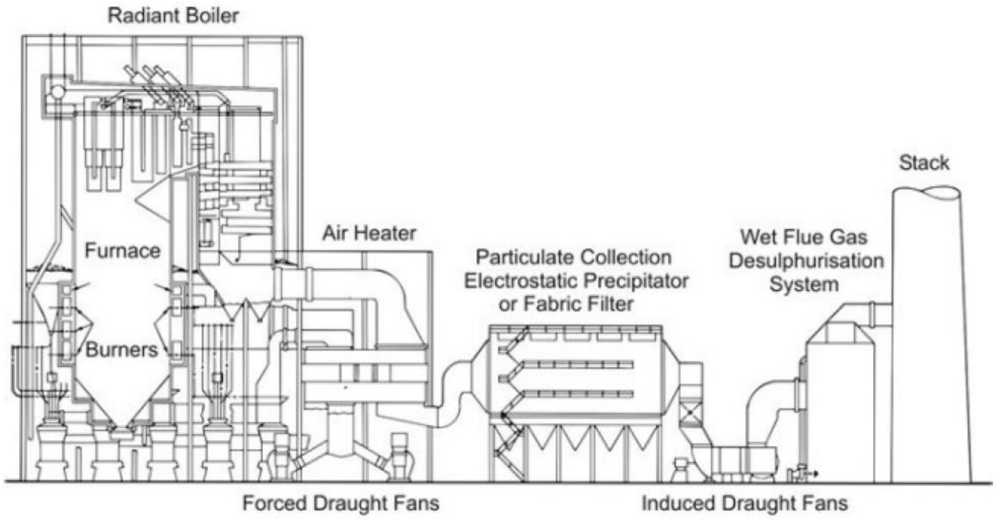

Figure 2: Draught plant [11]

Figure 3 is a schematic demonstration the flow path of combustion air which consists of primary air and secondary air. Primary air is separated from the secondary air after the air heater and directed to the mills and secondary air is directed into the boiler. The primary air stream also serves to transport the pulverized coal into the burners, hence separate ducting and primary air fans [11].

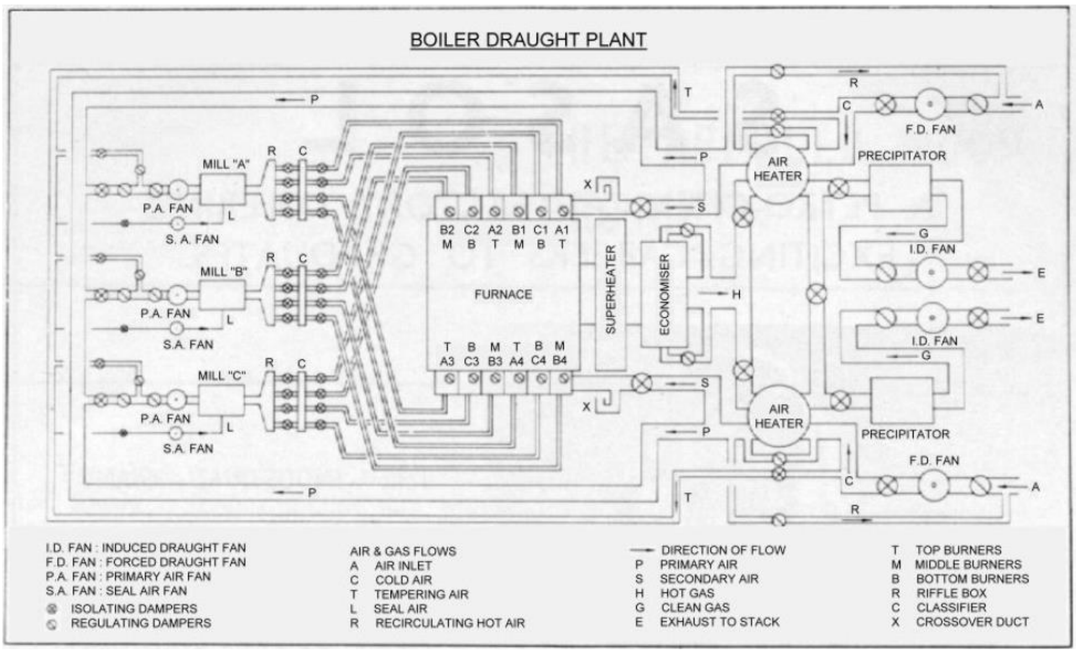

Figure 3: Boiler Draught Plant [11]

In South Africa, emissions are regulated by the National Environmental Management: Air Quality Act 39 of 2004 [32] by the South African government to reform the law regulating air quality and provide measures for prevention of pollution of ecological degradation. Facilities are required to monitor, limit, and report emissions to the Department of Environmental Affairs (DEA) as required by the act.

Optimizing the efficiency of a boiler plant in a coal-fired power plant is critical for the purpose of reducing carbon emissions, safety and for cost effective operation. To adhere to regulations and for safe and efficient operation of Eskom's fossil fuel firing boiler plants, the utility has put in place regulations to prevent explosions of Boiler Plants and Auxiliary Boilers through safe and sound operating, maintenance and engineering methods.

These regulations also contain minimum requirements for effective prevention of uncontrolled fires, explosions and extensive furnace damage to the boiler plant and auxiliary boilers. These regulations are documented in the Fossil Fuel Firring Regulation Standard [9] also known as the FFFR.

The FFFR lists boiler operation procedures and essential instrumentation requirements required for safe operation of a boiler plant; among these instruments are instruments to measure total combustion air flow just after the air heaters.

The regulation requires that during boiler operation, Total Combustion air flow shall be always adjusted to maintain the correct air/fuel ratio. Combustion air flow shall be measured by accurate air flow measuring devices whereas fuel input shall be established from the fuel flow calculation or estimated from the load on the mills.

The regulation requires that [9]:

- The total combustion air required by the boiler be measured after air heaters.
- Proper calibration of the Total Combustion air flow metering device in kg/s be performed with an approved independent mass flow measuring device every 72 months.
- Verification of the distributed control system/historical readings be performed with an approved independent mass flow measuring device every 24 months.
- Each site shall prepare a procedure to maintain the total combustion air flow measurement calibration to an accuracy of three percent at boiler Maximum Continuous Rating (MCR).

3. RESEARCH MOTIVATION

This study focuses on Arnot Power Station which is situated 50 km East of Middelburg in Mpumalanga. Constructed in 1968, this power station has six 350 MW units with a total installed capacity of 2100 MW [12].

The current installation utilises flue gas analysers to control combustion air flow. Oxygen analysers are installed at the economiser to measure the content of oxygen in the exhaust gas. Excess oxygen would indicate excess combustion air is supplied to the burners, and presence of unburnt carbon, mainly carbon monoxide (CO) would indicate incomplete combustion; hence carbon monoxide is also monitored to ensure that the maximum allowable CO value is not exceeded as per regulation.

The oxygen analyser technique gives a good indication of combustion performance, but it must be appreciated that the presence of tramp air due to leakages into the combustion chamber can lead to corresponding readings. Arnot Power Station is looking to install a measurement device that will measure the air flow rate in kg/s of combustion air as required by the FFFR.

The draught plants at Arnot Power Station consist of large ducts and flues of varying cross-sectional area, expansion joints, bypass stack, service doors and dampers. Additional conditions such as limited available straight duct runs, low flow rates, leakages, high concentration of fly ash and rectangular cross-section contribute to a complex velocity and temperature profiles. Sudden turns and turbulence result in flow separation and multidirectional flow.

As part of this study, a scaled duct was modelled using Solidworks and imported to Ansys-Computational Fluid Dynamics (CFD) to analyse the airflow in the ducts and establish a cross-section where the flow pattern is consistently one directional and parallel to the axis of the duct as recommended by ISO 3966 [10]. It is at this cross-section that the measurement device will be installed for the purpose of measuring airflow.

Figure 4 illustrates an overview of unit 3 at Arnot power station, with combustion air flow path coloured in yellow. The FFFR requires proper calibration of the total combustion airflow metering devices in kg/s be performed with an approved independent mass flow measuring device every 72 months.

Each site is required to maintain the total combustion airflow measurement calibration to an accuracy of three percent at the boiler Maximum Continuous Rating (MCR). The three percent

(3%) is required to be referenced to the ‘as calibrated’ parameters obtained from the calibration done with the approved independent mass flow measurement device [9].

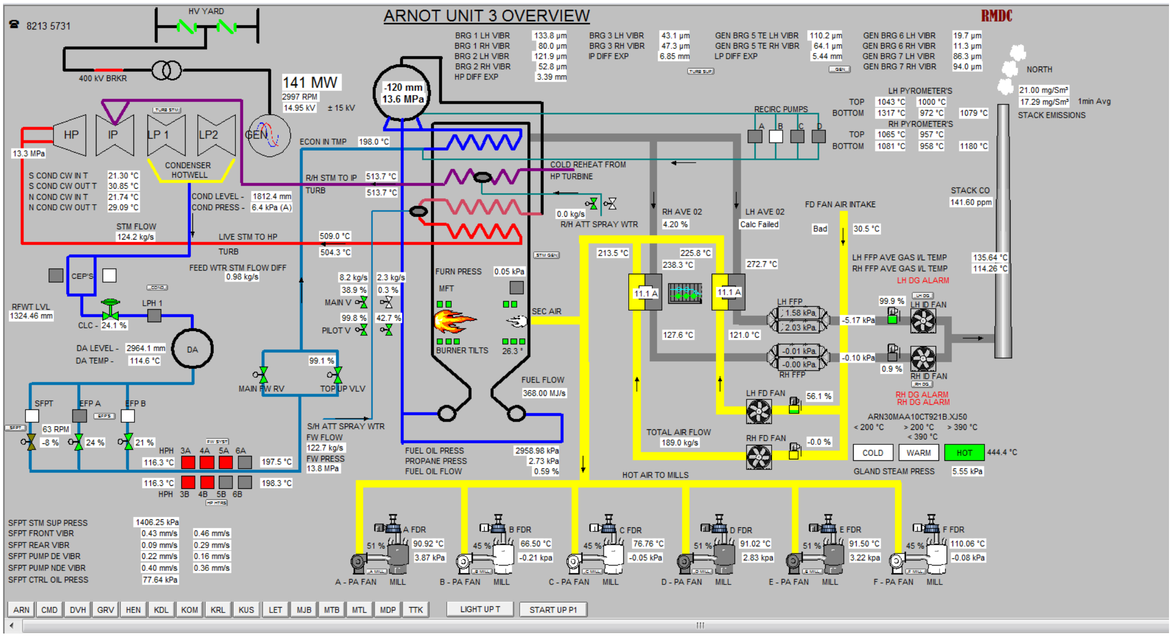

Figure 4: Unit 3 at Arnot PS

Traditional coal fired power stations are designed to use venturis and aerofoils for the purpose of measuring and maintaining correct combustion air flow. Eskom is looking to improve the techniques of combustion air flow measurements by developing and testing new techniques.

It is important to operate boiler plants efficiently and to reduce carbon emissions. For this reason, measuring air into the boiler is important in maintaining the required air/fuel ratio, thus ensuring complete combustion of combustibles in the boiler plant.

With the current configuration of ducts, to achieve accurate and reliable fluid flow measurements, a steady flow pattern is required. The steady state flow pattern requires constant cross-section over a sufficiently long length of duct referred to as the hydraulic diameters of the duct.

In the context of large square industrial ducts, it is mostly impossible to achieve fully developed flow profiles. This is due to the sudden changes in cross-sectional areas, short duct runs, constrictions, sudden turns and air infiltration in joints and expansion joints. Figure 5 illustrates the intricate duct configuration at Eskom’s Arnot Power Station. The cross-sectional of duct closest to burner entry is 2.286*1.524 m^2 and 8.7 m length.

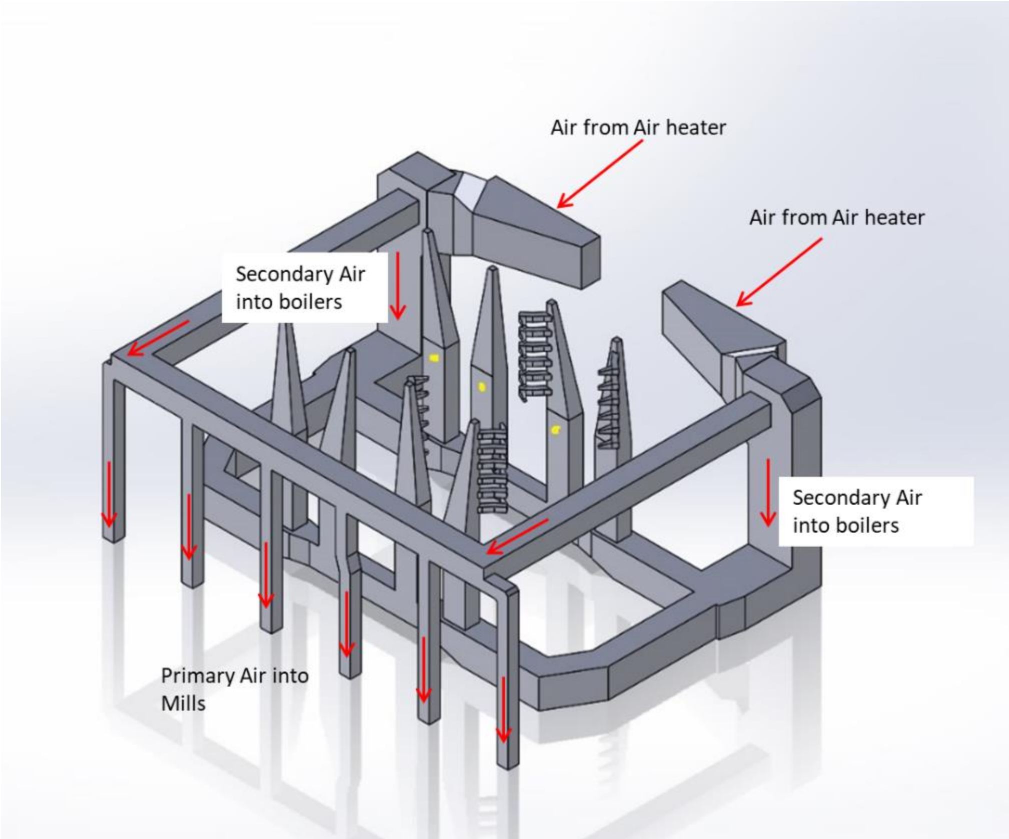

Figure 5: Combustion Air Ducts at Arnot PS

As required by the Fossil Fuel Firing Regulation, this study is aimed at investigating air flow measurements in complicated unsteady flow patterns in large industrial duct work after the air heaters and before entry into the boiler. It also investigates the performance and reliability of the proposed state of the art, mass flow measuring device that is proposed to be used for calibrating the online metering devices installed in the ducts; an Omniprobe with 14-holes, capable of measuring reverse flow in recirculation zones has been identified for this purpose.

This study will contribute to finding a feasible method for measuring in unsteady airflow conditions thus improving the efficiency of boiler operation. The equal area method as per ISO 10780 of 1994 [13], extensively used in industry is employed in this study to analyze complicated flow fields.

The amount of secondary air flow after the air heaters and into the boiler will be measured accurately thus ensuring adequate air is supplied to the boiler for complete combustion. The boiler operator will be able to measure the mass air flow into the boiler.

4. PROBLEM STATEMENT

Standard fluid flow measurements are normally taken in steady fluid flow patterns and require a fully developed and stabilized flow profile achieved over a long path. Studies have been conducted for flow through circular ducts with sufficient hydraulic diameter. The problem statement for this study is as follows:

- Achieve a measurement accuracy of 3% in large square ducts that are of varying large square cross-sectional area and have sudden turns. In some instances, there are bracing members.

5. AIM

For this study a prototype air duct with a square cross-sectional area is developed to simulate ducts with square cross-sectional area and with a 90º bend to simulate flow conditions that can be encountered in actual industrial ducts.

The aim of the study is to:

- Simulate and analyze distorted flow patterns resulting from complicated square/rectangular duct configuration and sudden turns.
- To identifying cost effective, advanced technologies that can accurately and reliably measure fluid flow properties in complex flow patterns.
- Verify the accuracy and precision of measurements of the identified measurement instrument.
- Compare the performance of the identified technology with other technologies.
- Establish possible zones in a duct where the fluid flow is recovering from a disturbance and investigate the accuracy of measurements at the identified zone using the identified technology and the use of Computational Fluid Dynamics (CFD).
- Establish an accurate calibration technique to ensure the correction factors of the online instruments will result in accurate measurement of the actual airflow.

6. RESEARCH QUESTIONS

Technology advances with time. The research questions for this study are:

- Is there technology capable of measuring mass airflow in highly distorted flow field to an accuracy of 3%?

- Can existing technologies be adapted to carry out accurate air-flow measurements in distorted air flow patterns?

7. LITERATURE REVIEW

7.1 Combustion Air

Combustion is a continuous chemical reaction during which the combustible elements in a fuel combine with oxygen and in so doing, release energy in the form of heat [14]. In combustion reactions, rapid oxidation of combustible elements of the fuel results in energy release as combustion products are formed [15]. Combustion air is the air that reacts with fuel in a combustion reaction. Fuel and air must mix intimately for combustion to be complete.

Fuels are essentially hydrocarbons, that is, compounds made up of carbon and hydrogen atoms. Fuels also contain relatively small percentages of other substances such as sulphur [14,15]. Combustion is complete when all the carbon present in the fuel is burned to carbon dioxide, and all other combustible elements are fully oxidized.

The oxygen necessary for the combustion of fuel is obtained from the atmospheric air which is a mixture of oxygen and nitrogen. The inert, incombustible nitrogen serves no purpose in combustion and in fact is a source of direct loss in that it absorbs and carries off energy that could have otherwise been used [14,15].

Primary air, secondary air, and over-fire air flow measurements are commonly used in these coal plants to properly control the coal and air mixture at the burners and meet environmental regulations. Accurate primary air flow measurement is required to properly dry and convey the coal particles to the burner. Accurate secondary air flow measurement to the burners is critical for maintaining the proper air-to-fuel ratio that results in more complete and stable combustion, creates better heat rates, helps avoid mill puffs, and supports lower emissions [11].

The amount of air in which there is theoretically just sufficient oxygen to burn all the combustible elements in a fuel completely is called theoretical amount of air. No free oxygen appears in the products [15].

For complete combustion, excess air is needed, but too much excess air is not a good thing as it absorbs some of the energy liberated and wastes it by being carried away in exhaust gases

[14]. Knowing the amount of air that is supplied to the boiler is critical for ensuring efficiency of the combustion process.

7.2 Ducts

The term to describe all parts in the air and gas flow circuit outside the main heat transfer surface is the Draught Plant. Ducts which are part of the draught plant provide a channel for the combustion air flow. The ducts are constructed of metal sheets that can prevent air leakages substantially, but it is in the expansion joints that leakages may occur.

Air leakages have been reduced to about 5% in large modern boilers with full membrane walls and welded ductwork; this is from the furnace to induction fan [11]. Majority of Eskom's coal-fired power plants are old as they have been around for decades.

7.3 Aerofoils

Some of the newly designed plants rely on older technologies (venturi and aerofoil) for combustion airflow measurement. Figure 6 illustrates Aerofoil probe specially designed to measure flow through a square or rectangular duct. The aerofoil name relates to the shape of the aircraft wing which creates an obstruction.

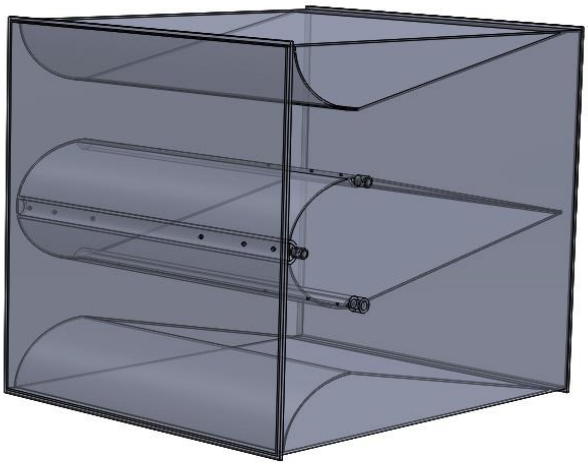

Figure 6: Aerofoil [17]

Inside the aerofoil is a Piezometric ring connection arrangement, which gives the averaged pressure reading for high-pressure and low-pressure side as depicted in the Figure 7. The difference between the 2 readings gives the differential pressure and in turn flow reading [17].

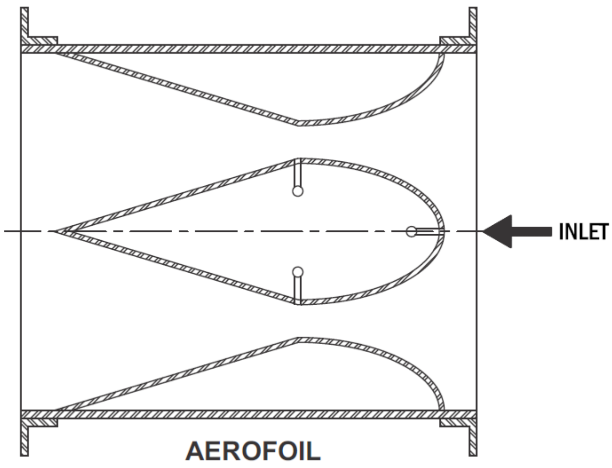

Figure 7: Aerofoil Cross Section [17]

The aerofoil shape creates an acceleration of fluid towards the throat and the throat pressure also sense by a series of pressure ports. This gradual and smooth inlet of aerofoil makes a less pressure loss across the element and the aerofoil tail will recover most the pressure drop at the throat [17].

Applications

Aerofoil probes are mainly applied for flow measurement in;

- Primary, Secondary and Tertiary air flow in the boiler plants.
- Flue gas measurement in large ducts.

The aerofoil shaped restriction in the flow helps to linearize the velocity profile and for the high recovery of pressure drop. And the location of the pressure ports helps to avoid the chocking due to the small dust particles in the air and this reduces the necessity of purging [17].

The aerofoil has the following advantages and disadvantages [17]:

Advantages

- A standard design for flow measurement.
- Can be used for fluids containing little amounts of dust.
- Less susceptible to erosion.
- Less maintenance since there are no moving parts.
- Applicable in rectangular or square ducts.
- Easy installation.

Disadvantages

- High non-recoverable pressure loss; approximately 30% of the differential pressure.
- Requires a minimum of 4 duct runs upstream and 1 duct run downstream.
- Requires in situ calibration to determine a flow coefficient (K-factor). The resulting accuracy is therefore subject to the limitations of the calibration instrument such as the S-Type Pitot, and the human factor of the traverse process.
- K-factors tend to be non-constant over a broad range of the velocity.

For square or rectangular ducts, conventional differential pressure flow meters cannot be used effectively. Only rectangular Venturi and Pitot tube can be used, but these have a limitation where long straight long ducts are required.

Flow restring devices in the flow stream prior to the combustion chamber create a pressure drop that produce lower output from the boiler. This pressure drop is a direct result of the restricted flow. To adjust for this pressure drop, facilities frequently oversize or overwork the air blowers, compressors, or fans to increase upstream flow or use heaters to preheat the upstream air [18]. These methods for increasing the air flow rate and temperature also lead to increased costs of fuel, equipment, and maintenance.

An advantage to removing the pressure drop caused by flow restrictors is that low NO_x burners can operate more efficiently and demonstrate better performance at reducing NO_x levels. The low-NO_x concept includes staged air combustion, staged fuel combustion, and external flue gas recirculation, which are all based on the principle of breaking down the combustion to reduce prolonged high temperatures [18].

The goal of any power plant modifications is to implement a change that improves efficiency, reduces maintenance, reduces operating costs, supports rapid installation, or enhances reporting capabilities for a cost that pays for itself through reduced fuel usage or accurate emissions records [18].

7.4 Measurement in closed conduits

Various methods exist for the determination of fluid flow rates. For this study the intention is to determine flow rate in a large square industrial duct. The ISO 3966:2008 “Measurement of fluid in closed conduits – Velocity area method using Pitot Static Tubes” [10] standard has been adopted for this purpose.

The International Standard is applicable to regular flow of a fluid running full in a conduit or duct, of substantial constant density or corresponding to Mach number not exceeding 0.25 and with substantially constant stagnation temperature.

The method of measurement and the requirements defined in the standard aims at reaching 95% confidence level, and uncertainty level no greater than ±2%. The ISO 10780 of 1994 [13] standard specifies manual methods of measuring the velocity and volumetric flowrate of gas streams in ducts. It specifies the two types of probes, namely L and the S type for determining the velocity.

The International Standard ISO 10780 [13] states that rectangular ducts should be divided into equal areas at the sampling point by line parallel to the sides of the duct and the sampling points are in the centre of each area.

Ostrowski et al. [19] conducted a study to measure gas flow through rectangular duct with short straight sections and large cross section. The study makes use of an inset in the duct which limited the cross-section area to 33%.

An addition of a baffle plate before the inset was allowed for. Measurements were conducted at the neck of the inset. A device used for the single point measurement method was a Prandtl tube. Figure 8 shows the experimental setup [19]:

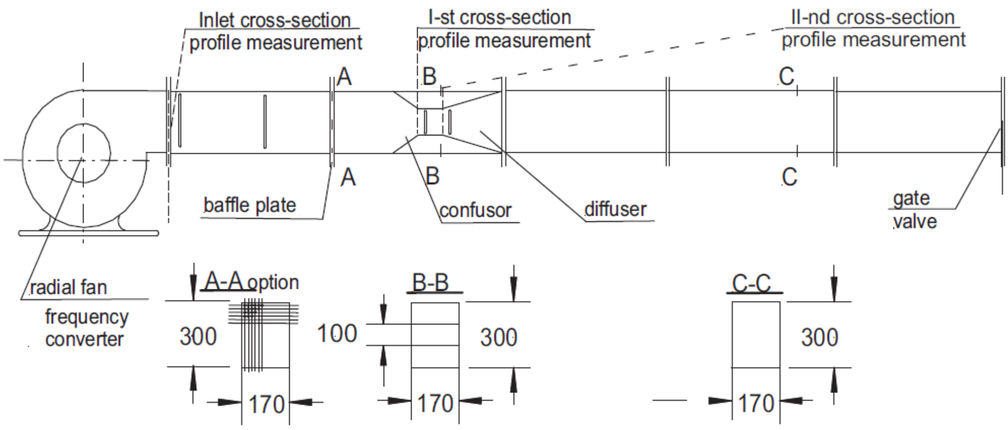

Figure 8: Experimental Setup [19]

The shape and the dimensions of the measuring section were initially studied using numerical models and the results (Figure 9) were used to design the test stand.

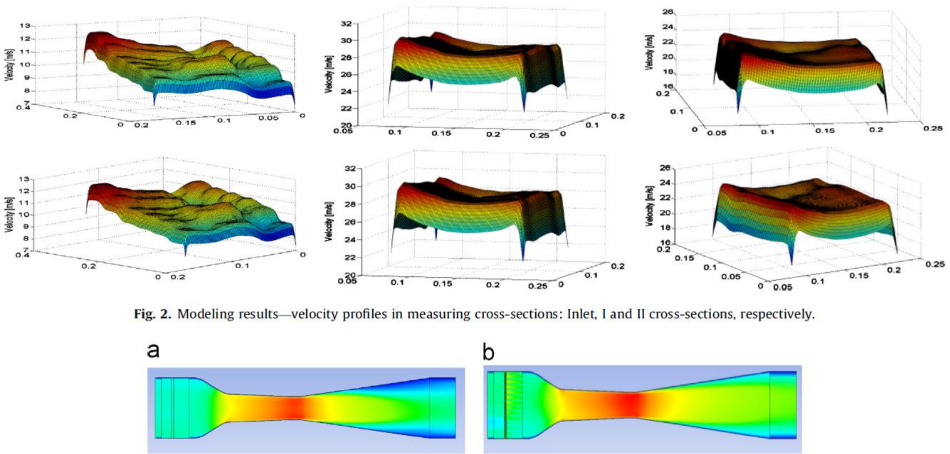

Figure 9: Modelling results-velocity profiles in measuring cross-sections [19]

Ostrowski states that the proposed method of a single-point air measurement, incorporating the correction factor k, satisfies the requirement of industrial measurement and that it may be used in short ducts with rectangular cross-section with an equivalent diameter greater than 1000 mm [8].

A study conducted by E. Rieschel [8] investigates velocity profile of a fluid (water) flowing through a straight, square duct (50 mm x 50 mm), 5m in length using a non-intrusive technique called Particle Image Velocimetry (PIV) and comparing the resulting velocity profiles with those generated from the calculated results using Navier-Stokes Equations. Figure 10 illustrates the planes studied for entrance length.

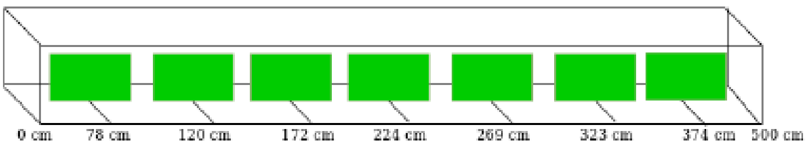

Figure 10: Measurement entrance length [8].

The results of the study at a hydraulic diameter of 374 cm and flow rate of 3.5 litres/min showed that the flow is asymmetric in laminar regime. The Navier-Stokes equations yielded a symmetric velocity profile as illustrated in Figure 11(a) which did not coincide the velocity profile generated from experimental results as in Figure 11(b) [8].

The velocity profile generated from experimental results was found to be asymmetric with the peak 5 mm off the centre of the duct. The study could not identify the source of error on the experimental results [8].

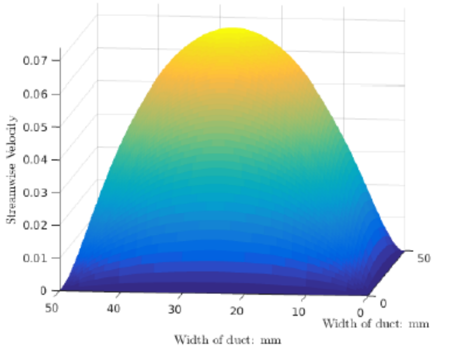

(a) Navier Stokes Theoretically Dimensionless Velocity Profile.

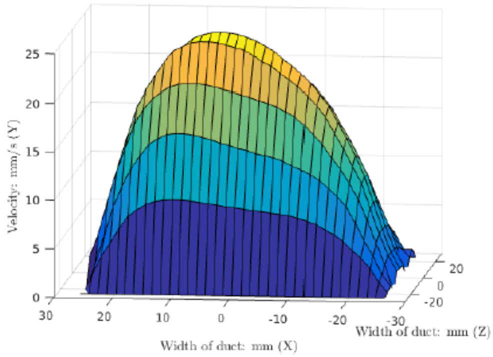

(b) Laminar Flow Velocity Profile

Figure 11: Velocity Profiles at 374 cm from the entrance [8].

A paper by Norfleet et al. [21] discusses the impact of wall effects on flue gas velocities in rectangular ducts and found that the equal area method results in an overestimation of the actual average velocity because it does not account for viscous shear effects and neglecting the significant velocity drop off as the velocity approaches zero at the stack wall as illustrated in Figure 12.

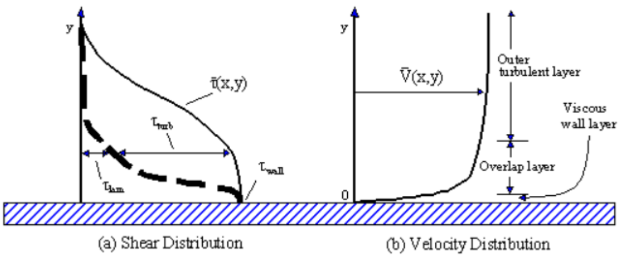

Figure 12: Typical Velocity and Shear Distribution in Turbulent Flow near the wall [21]

The theoretical mathematical model used to determine the wall velocities in circular stacks varies logarithmically with the distance from the wall and is expressed as equation [21]:

$$\frac{u}{u^*} = \frac{1}{K} ln \frac{yu^*}{v} + B \tag{1}$$

For fully turbulent flow equation (1) is simplified since the viscosity term disappears making equation (1) Reynolds number independent, resulting in equation (2).

$$\frac{u}{u^*} = \frac{u^*}{0.41} ln \frac{y}{\varepsilon} + 8.5 \tag{2}$$

Where u = velocity of near the wall measurement

u* = friction velocity

y = distance from the wall

ε = wall roughness

S. K. Norfleet et al. [21] suggest that neglecting the wall effects introduces bias that ranged from 1.7% to 3% for circular ducts. The bias is expected to be greater for square ducts because there is more wall surface for square ducts compared to circular ducts, wall effects are intense in the corners, and traverse points are further from the wall. The study concluded that the calculated wall effect adjustment factors for square ducts ranged from 4-5% in contrast to the 2-3%factor for circular ducts [21].

C Zhou [23] conducted a study to estimate volumetric flow rate through a circular duct, comparing equal area (experimental) and Log-Tchebycheff method (numerical). In the study performed 2-dimensional numerical simulations of air at a uniform velocity entering a straight duct of 60D was performed. The study found that the equal area method estimates volumetric flow rate better in a laminar regime. An experiment was conducted for Re of 24400, 54800 and 99400 where a Pitot-static tube was used to determine point velocities (Figure 13).

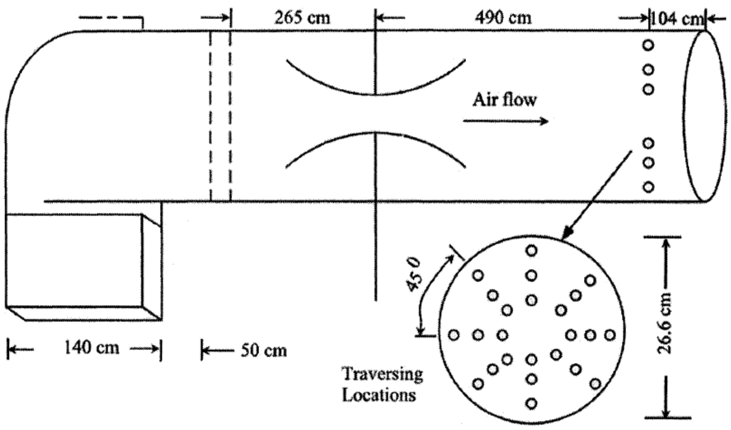

Figure 13: Schematic of the duct and measuring grid [23].

The study found that the Equal Area method predicted the flow rate by 2 to 4%, whereas the Log-Tchebycheff's value fell within ±1% of the reference value measured by a venturi meter. The study suggests that the Log-Tchebycheff's method could give more accurate volumetric flow rates in the tested turbulent regime [23].

7.5 Flow principles

Fluid flow can be either laminar, when the flow is streamlined and in ordered motion; or turbulent, when the flow has high velocity fluctuations in disordered motion [20]. In the 19th

century, Osborn Reynolds studied fluid flow patterns and defined an essential dimensionless parameter that can be used to determine if a flow pattern is laminar, turbulent or in transition. The parameter is known as Reynolds number [20]:

$$Re = \frac{Inertial\ Forces}{Viscous\ Forces} = \frac{\rho V D}{\mu} \tag{3}$$

Where ρ is the density of the fluid, μ is the dynamic viscosity, V is the velocity in the conduit and D is the pipe diameter. The flow regime can be predicted using Reynolds number (Re).

For square ducts the Reynolds number is calculated by a Hydraulic Diameter, which is a function of the Area (A) and Perimeter (P). For a duct with square cross-sectional area of a height h and width w the Hydraulic Diameter is determined as follows [20]

$$A = w \cdot h \tag{4}$$

$$P = 2w + 2h \tag{5}$$

$$D_h = \frac{4 \cdot A}{P} \tag{6}$$

The Reynolds number at which flow becomes turbulent is called the critical Reynolds number (Re_{cr}) and the value is different for different geometries and flow conditions. For internal flow, the accepted value of Re_{cr} is 2300 [24]. Transition flow from laminar to turbulent flow also depends on the geometric properties of the duct or pipe and the degree of the disturbance. Transitional flow occurs when $2300<Re<4000$. At this range, the increase in fluid flow velocity causes mixing between layers [24].

Turbulent flow ($Re>4000$) occurs at higher fluid velocity. The laminar layers break down and formation of eddies and swirls which results in a flatter velocity profile are the most favourable condition for predictable and accurate flow metering [23].

7.6 Bernoulli's Principle

In industry, a wide range of fluid-flow measurement applications exists and cannot be understated. From the control of fuel into the engine system of a train to measuring the air speed in aircrafts, the application of flow measurements is necessary and considerable. Fluid flow measurements involve the calculation of mass flow ($\dot{m}$) or volumetric flow rate ($\dot{Q}$).

The velocity of the fluid can be measured using different techniques including the use of Pitot tube, Venturi meter, and Orifice plate to mention a few. The basic principle of most of these instruments is based on Bernoulli's principle which relates the pressure, speed, and height of any 2 points in a steady stream flow field of constant density ρ [22].

$$P_1 + \frac{1}{2}\rho v_1^2 + \rho g h_1 = P_2 + \frac{1}{2}\rho v_2^2 + \rho g h_2 \quad (7)$$

The variables P_1, v_1, and h_1 refer to the pressure, speed, and height of fluid at point 1, whereas variables P_2, v_2, and h_2 refer to the pressure, speed, and height at point 2 as illustrated in the Figure 14 [23]. Conservation of mass states that the mass flow rate is constant. The mass flow rate in each point (1 and 2) in a duct is given by:

$$Mass\ flow = q_m = \rho q_v = \rho VA \quad (8)$$

$$\rho_1 V_1 A_1 = \rho_2 V_2 A_2 \quad (9)$$

Where q_m is the mass flow rate in kg/s and q_v is the volumetric flow rate in m^3/s.

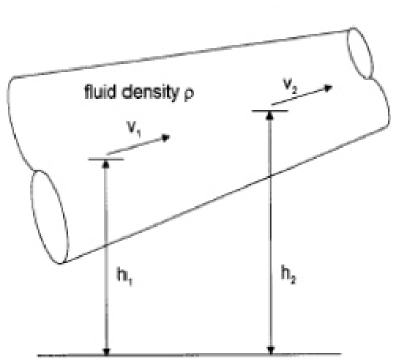

Figure 14: Bernoulli's principle [23]

Assuming the changes in height h is negligible and that the flow is brought to rest, the resulting pressure p_0 is the total or stagnation pressure. The dynamic pressure is given by [24]:

$$\Delta P = \frac{1}{2}\rho V^2 \quad (10)$$

The principle of most differential pressure devices is based on Bernoulli's principle. For this study the density is assumed to be constant and is determined using the equation of state, Ideal Gas Law equation:

$$\rho = \frac{p}{RT} \quad (11)$$

Where:

p is the local static pressure,

R is the l gas constant specific to the fluid, and

T is the local static temperature.

7.7 Pitot Static Tube

The International Standard ISO-3966 defines the Pitot-static tube as a tubular device of a cylindrical head attached perpendicularly to a stem allowing the measurement of differential pressure from which the flow rate of the fluid in which it is inserted can be determined, and which is provided with static pressure tapping holes (drilled around the circumference of the head at one or more cross-sections) and with a total pressure hole (facing the flow direction at the tip of the axially symmetrical nose of the head) [10].

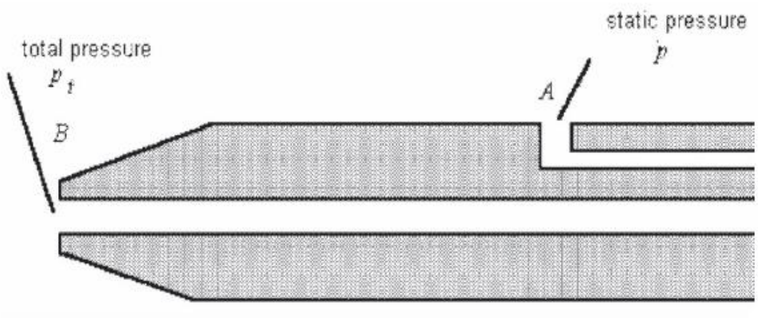

Figure 15: Section View of Pitot-static probe tip [25]

Figure 15 illustrates the Pitot-static probe tip. The holes around the circumference (A) measure the static pressure p whereas the hole in-line with the flow (B) measure the total pressure p_t.

The principle of the Pitot-static tube is outlined in Bernoulli's principle section above. The point velocity (V) in a flow field is given by [22]:

$$V = \sqrt{\frac{2\Delta p}{\rho}} = \sqrt{\frac{2(p_t - p)}{\rho}} \qquad (12)$$

Where p is the static pressure, p_t is the total pressure, ρ is the fluid density, and Δp is the dynamic pressure also known as the differential pressure.

W.H. Howe et al. [26] found that the static pressure errors depend on the fluid viscosity, fluid velocity, and compressibility of the fluid. The Pitot-static tube is sensitive to flow direction and must be aligned to face the flow, and this can be challenging when the flow is turbulent.

The volumetric flow rate ($\dot{Q}$) can be determined using the equation 4:

$$\dot{Q} = AV = A\sqrt{\frac{2\Delta p}{\rho}} = A\sqrt{\frac{2(p_t - p)}{\rho}} \qquad (13)$$

Where A is the cross-sectional area of the duct.

For coal plant application, combustion air contains fly ash particulates which are prone to plug the Pitot-static tube holes and may affect the accuracy of the flowrate readings.

7.8 Orifice Meter

An orifice plate consists of a flat plate that has a sharp-edged machined hole. The plate is placed concentrically in a pipe as shown in Figure 16. As fluid flows through the pipe, the flow suddenly contracts as it approaches the orifice and then expands after the orifice back to full pipe diameter. This forms a throat immediately past the orifice. The reduction in flow pattern through the throat causes increased velocity and hence a lower pressure at the throat [23].

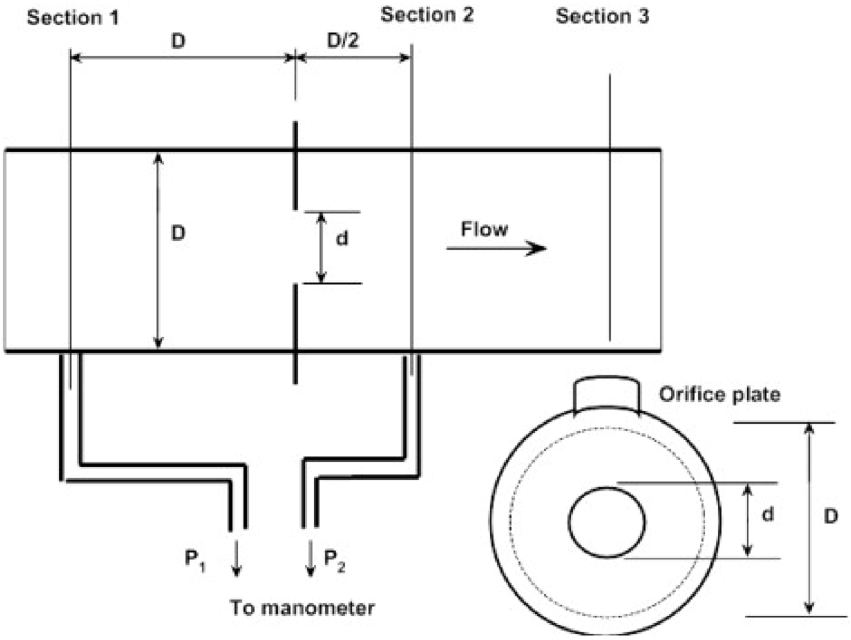

Figure 16: Orifice Meter [23]

The pressure difference between the section before the orifice and the section after the orifice can be used to calculate the fluid flow rate. The coefficient of discharge is a dimensionless number used to characterize the flow and pressure loss behavior of orifice plates in the fluid system [23].

The coefficient of discharge impacts the accuracy or the overall uncertainty in the determination of the flow rates. The coefficient value is a function of the orifice bore to the pipe diameter ratio (B), pressure tap location, and the operating Reynolds number [23].

For best results, the flowmeter is calibrated to determine the discharge coefficient. However, the calibration of each meter may be expensive, impractical, and unnecessary if published values based on dimensions and good installation exist.

The proposal of a universal orifice equation was presented to ISO/TC30/SC2 in 1975 based on the paper presented by Stolz at an NEL Flow Conference in April 1975 [23]. Stolz equation was presented with the idea that two or more identical orifice meters should have the same coefficient, with different identification serial numbers.

The **Stolz equation** as it appears in ISO/5167 [29]:

$$C = 0.5959 + 0.0312B^{2.1} - 0.184B^{8} + 0.0029B^{2.5}\left[\frac{10^{6}}{R_D}\right]^{0.75} + 0.09L_1B^{4}(1-B_4)^{-1} - 0.0337L'_2B^{3} \quad (14)$$

Where [29]:

- C is the discharge coefficient (dimensionless),
- B is the orifice bore to the pipe diameter ratio,
- R_D is Reynolds number based on the pipe diameter,
- R_d is Reynolds number based on the orifice bore diameter,

The term L_1 denotes the location of the upstream pressure tap with respect to the face of the orifice plate and L'_2 denotes the location of the downstream tap with respect to the downstream face of the orifice [23].

$L_1 = 0$ for corner taps

$L_1 = 1/D$ for flange taps

$L_1 = 1$ for D and D/2

When $L_1 >= 0.4333$, use 0.0390 for a coefficient term of $B^{4}(1-B_4)^{-1}$

$L'_2 = 0$ for corner taps

$L'_2 = 1/D$ for flange taps

$L'_2 = 0.47$ for D and D/2 tapings

The volumetric flow rate $(\dot{Q})$ from Eq. (13) becomes:

$$\dot{Q} = CA\sqrt{\frac{2\Delta p}{\rho}} = CA\sqrt{\frac{2(p_t - p)}{\rho}} \quad (15)$$

7.9 Five-Hole Pressure Probes

Though Eq. (12) is applicable for Pitot-static probe and is valid for flow where the flow is mostly parallel to the axis of flow. Experiments have shown that as the angle between the flow and the Pitot-static probe tip increases beyond 10º, the pressure read by the central hole begins to decrease as a larger component of the incident flow is not brought down to stagnation.

The actual pressure is a complex function of the flow angle and the probe tip geometry, for a particular probe the flow angle may be related to the pressure by a single function which may be obtained by calibration [24].

A paper by Birch [10] considered a fluid flow with magnitude U at some Yaw angle β relative to the probe axis. If $\beta=0^{o}$, then the pressure P_1 recorded by the tube will be stagnation pressure P_0. Similarly, if $\beta=90^{o}$, P_1 would be static pressure P_s. For all the angles where $0^{o}<\beta<90^{o}$, then $P_0>P_1>P_s$. the relationship between P_1 and β may be expressed as [24]

$$\beta = f_1\left(\frac{2P_1}{\rho U^2}\right) \tag{16}$$

Where f_1 is continuous function defined for a range $0^o \le \beta \le 90^o$, and the pressure has been normalized against the local dynamic pressure to render function f_1 insensitive to the velocity. For range $\beta<0$ or $\beta>90^o$, the hole will be in the wake of the body of the tube, as such P_1 will not yield meaningful value for local pressure, and f_1 will be undefined for this range. A five-hole probe is configured by attaching four tubes ground, each ground to an angle of 45^o as illustrated in Figure 17[24].

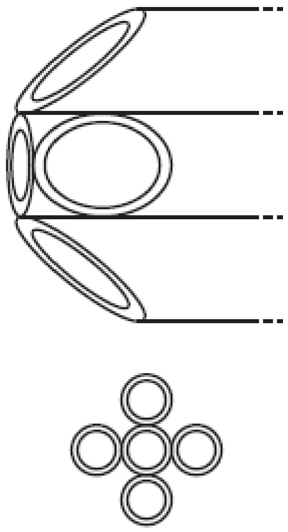

Figure 17: Five-Hole probe [24]

In this configuration, the top tube will be sensitive to flows between 0^o and 45^o, whereas the bottom tube will be sensitive to flows between -45^o and 0^o, the yaw β may then be expressed by piecewise as [24]:

$$\beta = f_1\left(\frac{2P_1}{\rho U^2}\right) \qquad -45<\beta<0^o,\ (P_1>P_2) \tag{17}$$

$$\beta = f_2\left(\frac{2P_2}{\rho U^2}\right) \qquad 0<\beta<45^o,\ (P_2>P_1) \tag{18}$$

Where f_1 and f_2 are arbitrary functions determined by calibration. This concept may be extended to a five-hole probe to include pitch angles α. The calibration space of the five-hole probe may be expressed as [24],

$$\alpha = f_1\left(\frac{2P_1}{\rho U^2}\right) \qquad -45<\beta<0^o,\ (P_1>P_2) \tag{19}$$

$$\alpha = f_2\left(\frac{2P_2}{\rho U^2}\right) \qquad 0<\beta<45^o,\ (P_2>P_1) \tag{22}$$

Where β is the yaw angle and α is the pitch angle. Furthermore, the static and stagnation pressures may be approximated as

$$P_0 \approx P_5 \tag{21}$$

$$P_s \approx \bar{P} = \frac{1}{4}\sum_{i=1}^{4} P_i \tag{22}$$

It is then necessary to obtain four independent piecewise functions through calibration. While the pressure holes are sensitive to changes in Yaw and Pitch, the pressure difference in adjacent holes is sensitive to flow angularity [10]. The Yaw (Cp_α) and Pitch (Cp_β) coefficients are defined as [24]:

$$Cp_\alpha = \frac{P_5 - P_1}{P_5 - \bar{P}} \tag{23}$$

$$Cp_\beta = \frac{P_4 - P_2}{P_5 - \bar{P}} \tag{24}$$

Equation (23) and (24) will be more sensitive to the flow angles. To address the error between approximate static and stagnation pressures used, the difference between approximate and actual static and stagnation pressures may be obtained through calibration, normalized against the approximate dynamic pressure, and expressed as nondimensional coefficient, so that:

$$Cp_o = \frac{P_5 - P_0}{P_5 - \bar{P}} \tag{25}$$

$$Cp_s = \frac{\bar{P} - P_s}{P_5 - \bar{P}} \tag{26}$$

Where P_0 and P_s are obtained elsewhere on the measurement plane by pitot tube.

The probe is calibrated by positioning it at a series of known angles (α and β) in flow field with a fixed velocity magnitude U and recording the coefficients Cp_β, Cp_α, Cp_0, and Cp_s at each α and β.

From the calibration data set, independent piecewise functions may be defined such that [24]:

$$\alpha = f_\alpha(Cp_\beta, Cp_\alpha) \tag{27}$$

$$\beta = f_\beta(Cp_\beta, Cp_\alpha) \tag{28}$$

$$Cp_0 = f_0(Cp_\beta, Cp_\alpha) \tag{29}$$

$$Cp_s = f_s(Cp_\beta, Cp_\alpha) \tag{30}$$

Given any set of pressured measured in a flow of unknown angularity and magnitude the coefficients Cp_β and Cp_α may be calculated using equation (25) and (26). The flow angles α and β, and the coefficients Cp_0, and Cp_s may be obtained by curve interpolation. The velocity magnitude may be calculated using the interpolated values of Cp_0, and Cp_s [24]

$$|V| = \left(\frac{2}{\rho}(P_5 - \bar{P})(C_{ps} - C_{p0} + 1)\right)^{1/2} \tag{31}$$

With reference Figure 18, the relationship between the velocity components (V, U, W), and the flow angles (α, β, φ, θ) is such that [24]:

$$U = |V|cos\alpha \cos\beta = |V|cos\theta \tag{32}$$

$$V = |V|sin\alpha = |V|sin\theta sin\varphi \tag{33}$$

$$W = |V|cos\alpha cos\beta \tag{34}$$

Where θ is the conical angle and φ is the probe roll.

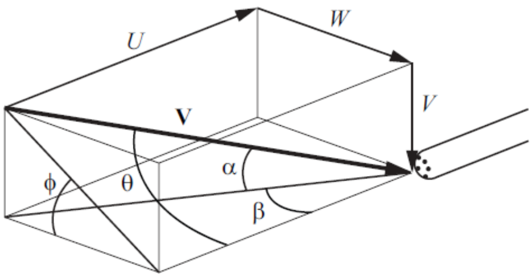

Figure 18: Graphical representation of velocity components Yaw, Pitch and Roll angles [24].

7.10 14-hole Omniprobe

Figure 19 illustrates the 14-hole Omniprobe identified for this study. The probe length can be extended to 2.5 m using extensions.

Figure 19: 14-hole Omniprobe (Straight type) [26]

Like the concept of five-hole probe, the use of 14-hole Omniprobe is a precise way to measure fluid flow velocity and flow angles up to ±160º. By measuring the port pressures at the probe's head, the following values can be determined [26]:

- Total and static pressure
- Angle of attack
- Velocity of flow
- Derived thermodynamic quantities.

Figure 20: 14-hole Omniprobe tip [26]

The 14-hole Omniprobe identified for this study can measure reverse flow. Figure 20 illustrates the tip of the probe tip machined for best aerodynamic accuracy and performance. Each probe is calibrated in a wind tunnel (Figure 21) since the dependence of the port pressures on the flow angle is different from probe to probe due to manufacturing tolerances [27].

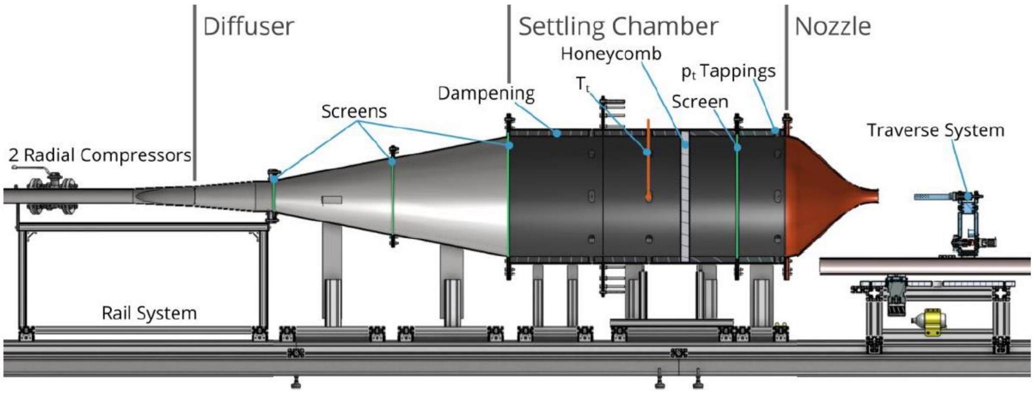

Figure 21: Open Jet Calibration Wind Tunnel [27]

The calibration of the 14-hole Omniprobe comprises of [27]:

- measuring different port pressures depending on flow speed and in known flow conditions.
- Determination of calibration coefficients Cp_β, Cp_α, Cp_0, and Cp_s from total, static and port pressures. Coefficients depend on the flow angle with respect to the port with the highest pressure. The probe uses a sectorial method which allows the exclusion of port pressures on a separate zone.
- Curve fitting is then applied to Cp_β, Cp_α, Cp_0, and Cp_s distribution.

7.11 Uncertainty in Experimental Data

Engineering properties or variables are rarely known to an extreme degree of accuracy. The uncertainty of data is normally indicated by percentage (%) confidence that the true value lies in the band or range. Uncertainty results from systematic error due to the instrument and environment and due to a random error resulting in repeated readings. For a desired result P which depends on variable x. If x has an uncertainty of δx, the uncertainty δP is estimated from the calculus [20]:

$$\delta P \approx \frac{\partial P}{\partial x}\delta x \tag{35}$$

If P depends on multiple variables, $P=P(x_1,x_2,x_3,\ldots,x_n)$, the uncertainty δP is calculated as the root mean square estimate [20]:

$$\delta P \approx \left[\left(\frac{\partial P}{\partial x_1}\delta x_1\right)^2 + \left(\frac{\partial P}{\partial x_2}\delta x_2\right)^2 + \cdots \left(\frac{\partial P}{\partial x_n}\delta x_n\right)^2\right]^{0.5} \tag{36}$$

If the quantity P is a simple power expression of variables $x_1^{n_1}$, $x_2^{n_2}$ ...., then [20]:

$$\frac{\partial P}{\partial x_1} = \frac{n_1 P}{x_1},\ \frac{\partial P}{\partial x_2} = \frac{n_2 P}{x_2},\ \frac{\partial P}{\partial x_3} = \frac{n_3 P}{x_3} \tag{37}$$

Thus from Eq. (37) [20],

$$\frac{\delta P}{P} = \left[\left(n_1\frac{\delta x_1}{x_1}\right)^2 + \left(n_2\frac{\delta x_2}{x_2}\right)^2 + \cdots \left(n_n\frac{\delta x_n}{x_n}\right)^2\right]^{0.5} \tag{38}$$

7.12 Computational Fluid Dynamics (CFD)

7.12.1 CFD Governing Equations

According to ANSYS learning, computational fluid dynamics produces quantitative predictions of fluid-flow phenomena based on the conservation laws of mass, conservation of momentum, and conservation of energy governing fluid motion [28]. The governing equations of fluid dynamics are called the Navier-Stokes equations. These equations form the basis of Computational Fluid Dynamics. These are applicable for fluid flow assuming the following [28]:

- Pure translation or rigid body rotation.
- Newtonian fluid.
- The fluid flow is isentropic.

- Viscous forces act tangentially to the fluid element, and its normal is zero.

Conservation of mass equation in Cartesian form for 3D field is given by [28]:

$$\frac{\partial\rho}{\partial t}+\frac{\partial\rho u}{\partial x}+\frac{\partial\rho v}{\partial y}+\frac{\partial\rho w}{\partial z}=0 \tag{39}$$

Conservative form of momentum equation is [28]

$$\rho\left(\frac{\partial u}{\partial t}+u\frac{\partial u}{\partial x}+v\frac{\partial u}{\partial y}+w\frac{\partial u}{\partial z}\right)=-\frac{\partial\rho}{\partial x}+\frac{\partial}{\partial x}\left[2\mu\frac{\partial u}{\partial x}-\frac{2}{3}\mu\left(\frac{\partial u}{\partial x}+\frac{\partial v}{\partial y}+\frac{\partial w}{\partial z}\right)\right]+\frac{\partial}{\partial y}\left[\mu\left(\frac{\partial u}{\partial y}+\frac{\partial v}{\partial x}\right)\right]+\frac{\partial}{\partial z}\left[\mu\left(\frac{\partial u}{\partial z}+\frac{\partial w}{\partial x}\right)\right]+F_{b,x} \tag{40}$$

$$\rho\left(\frac{\partial v}{\partial t}+u\frac{\partial v}{\partial x}+v\frac{\partial v}{\partial y}+w\frac{\partial v}{\partial z}\right)=-\frac{\partial\rho}{\partial y}+\frac{\partial}{\partial x}\left[\mu\left(\frac{\partial v}{\partial x}+\frac{\partial u}{\partial y}\right)\right]+\frac{\partial}{\partial y}\left[2\mu\frac{\partial v}{\partial y}-\frac{2}{3}\mu\left(\frac{\partial u}{\partial x}+\frac{\partial v}{\partial y}+\frac{\partial w}{\partial z}\right)\right]+\frac{\partial}{\partial z}\left[\mu\left(\frac{\partial z}{\partial z}+\frac{\partial w}{\partial y}\right)\right]+F_{b,y} \tag{41}$$

$$\rho\left(\frac{\partial w}{\partial t}+u\frac{\partial w}{\partial x}+v\frac{\partial w}{\partial y}+w\frac{\partial w}{\partial z}\right)=-\frac{\partial\rho}{\partial z}+\frac{\partial}{\partial x}\left[\mu\left(\frac{\partial w}{\partial x}+\frac{\partial u}{\partial z}\right)\right]+\frac{\partial}{\partial z}\left[2\mu\frac{\partial w}{\partial z}-\frac{2}{3}\mu\left(\frac{\partial u}{\partial x}+\frac{\partial v}{\partial y}+\frac{\partial w}{\partial z}\right)\right]+\frac{\partial}{\partial y}\left[\mu\left(\frac{\partial w}{\partial y}+\frac{\partial v}{\partial z}\right)\right]+F_{b,z} \tag{42}$$

CFD applies the conservative form of the momentum equations i.e., M_x (Eq. 34), M_y (Eq. 35), and M_z (Eq. 36) [33].

Conservation of energy equation is given by [28]:

$$\frac{\partial(\rho e_t)}{\partial t}+\nabla.\left[\rho\vec{V}\left(e_t+\frac{p}{\rho}\right)\right]=\nabla.\left[k\nabla T+(\overline{\overline{\tau}}.\vec{V})\right]+\dot{s_g} \tag{43}$$

The Navier stokes equations are applied to a mathematical model. Depending on the flow conditions and physics to be analyzed, the Navier-Stokes equations for the analysis can be any of the partial differential equations [28].

A mathematical model is setup to define the geometry of the fluid to be analyzed. This is followed by defining the boundary conditions and initial conditions. Initial conditions and boundary conditions provide a unique solution for the mathematical model.

7.12.2 Mesh/Grid

A mesh divides the geometry into many elements which are to be used by the CFD solver to construct control volumes. The volumes are referred to as cells with faces, edges and nodes as illustrated in Figure 22 [29].

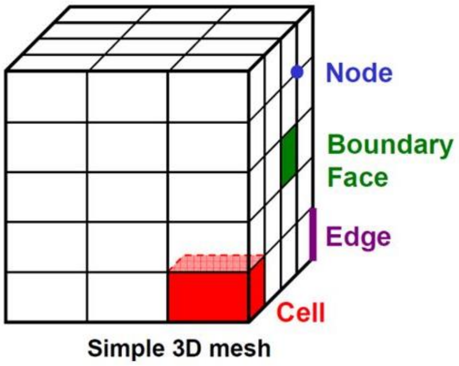

Figure 22: Mesh illustration [29]

When generating a mesh, the mesh type as illustrated in Figure 23 is to be considered. The purpose of the mesh generator is to decompose the flow domain into control volumes [29].

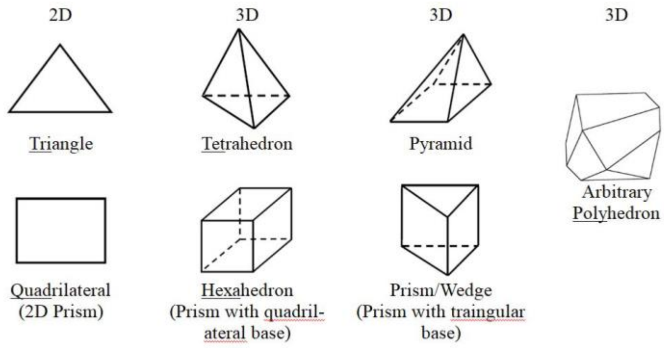

Figure 23: Types of Meshes [29]

For 3D model, this study compares tetrahedron (Tet) with hexahedron (Hex).

For flow aligned problems [29]:

- Hex can provide higher quality solutions with fewer cells/nodes than a comparable Tet.
- Quad meshes show reduced numerical diffusion when the mesh is aligned with the flow.
- It requires more effort to generate Hex than it does Tet.

For complex geometries [29]:

- It is practical to go for Tet than Hex where the flow is not aligned.
- Tet saves meshing effort and is quicker to generate.

In some instances, hybrid meshes are applied to combine Tet elements with other elements in selected regions.

8. RESEARCH METHODOLOGY

The main aim of this quantitative study is to establish a procedure of conducting accurate, reliable, and repeatable air-flow measurements in large square industrial ducts. Due to sudden changes in the duct cross-sectional areas and the shortness of duct runs affecting the hydraulic gradient, the fluid flow profile does not get to recover in time from a flow disturbance to allow for accurate measurements.

It is for this reason the study needed a flow measuring instrument capable of measuring reverse flow in complex flow conditions in square or rectangular ducts.

8.1 14-Hole Omniprobe

For this study, a probe capable of measuring reverse flow would allow for modeling complex velocity flow profiles in the cross-sections of interest in the duct. The study identified a 14-hole Omniprobe capable of measuring reverse flow around its spherical probe head, see Figure 24. The shape of the probe is straight and is about 285 mm in length which can be extended by means of a 2 m extension.

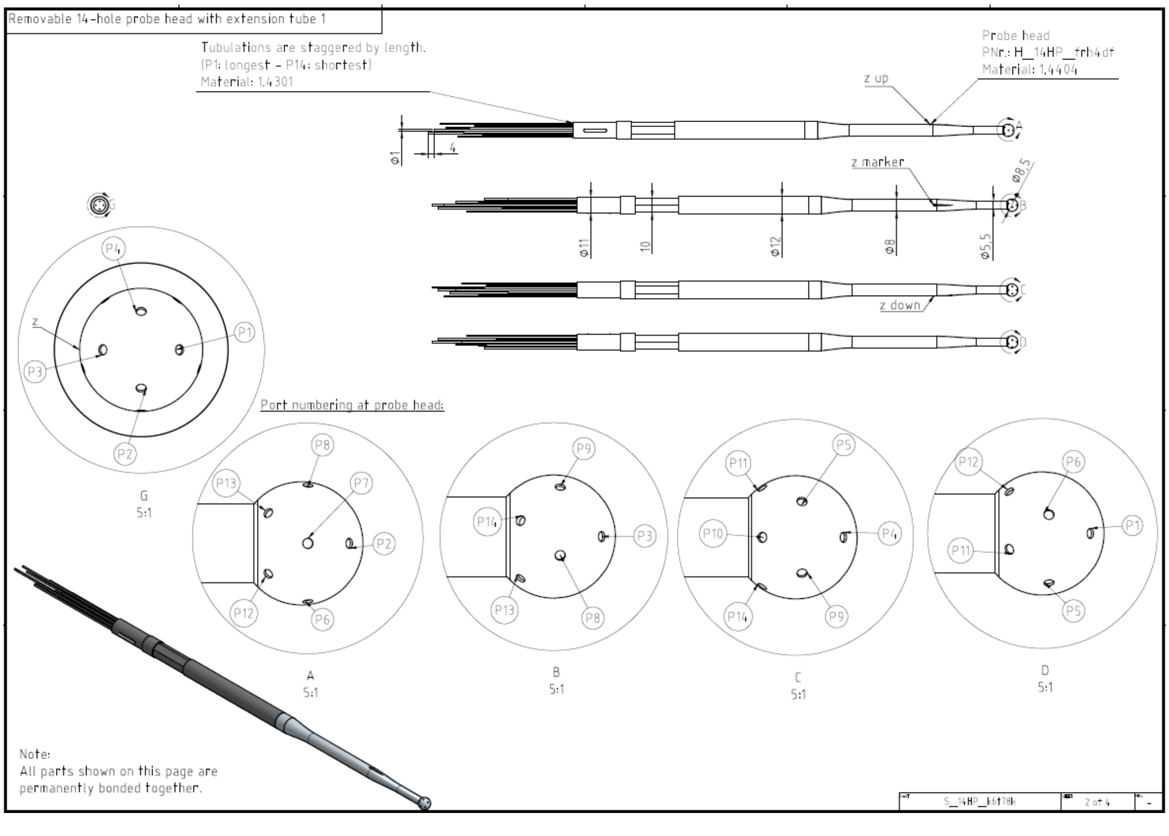

Figure 24: 14-hole Omniprobe [27]

The probe has a reference face, and the coordinate system with the output velocity components and angles are illustrated in Figure 25.

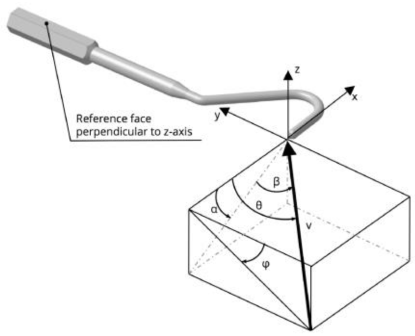

Figure 25: Coordinate system and standard reference face location [27]

The output results from the Omniprobe:

- Pressure readings by 14-holes to determine the total and static pressure.
- Angle of attack θ, Yaw β, Pitch α, and Roll φ.
- Velocity of flow components along the (x-axis – u), (y-axis – v), and (z-axis -w)
- Derived thermodynamic quantities.

The measurement zone of the 14-hole Omniprobe is illustrated in Figure 26.

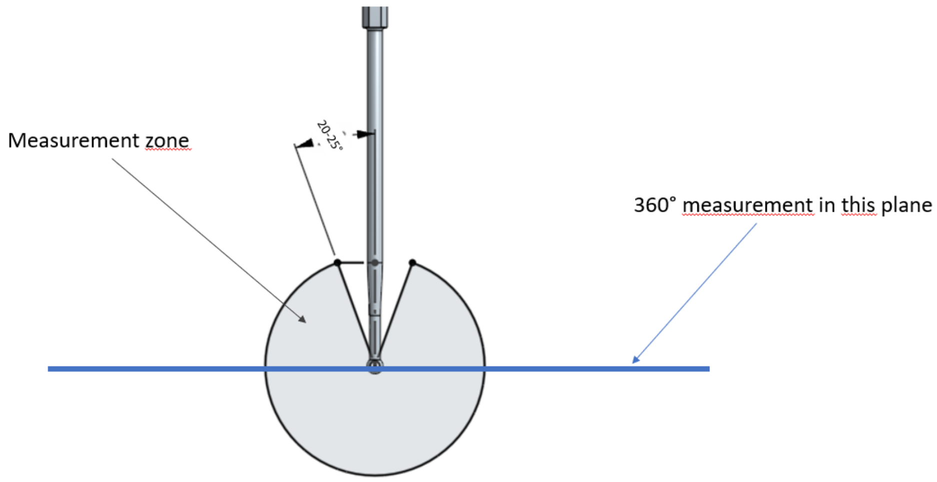

Figure 26: 14-hole Omniprobe zone of measurements [27]

The 14-hole Omniporbe was supplied with VectoVis Pro 1.0 computer program for post-processing raw data.

8.2 Pressure scanner

The PSC16 Multichannel Pressure Scanner with full-scale accuracy of 0.1% (Figure 27) enables the simultaneous acquisition of up to 16 differential pressures. Temperature compensated transducers feature high accuracy and minimal offset drift.

Each pressure measuring channel capacity ranges from 125 Pa and 15 kPa with the transmission rate of up to 50 Hz. For the current study, 14 channels were necessary in the application of the 14-hole Omniprobe [30].

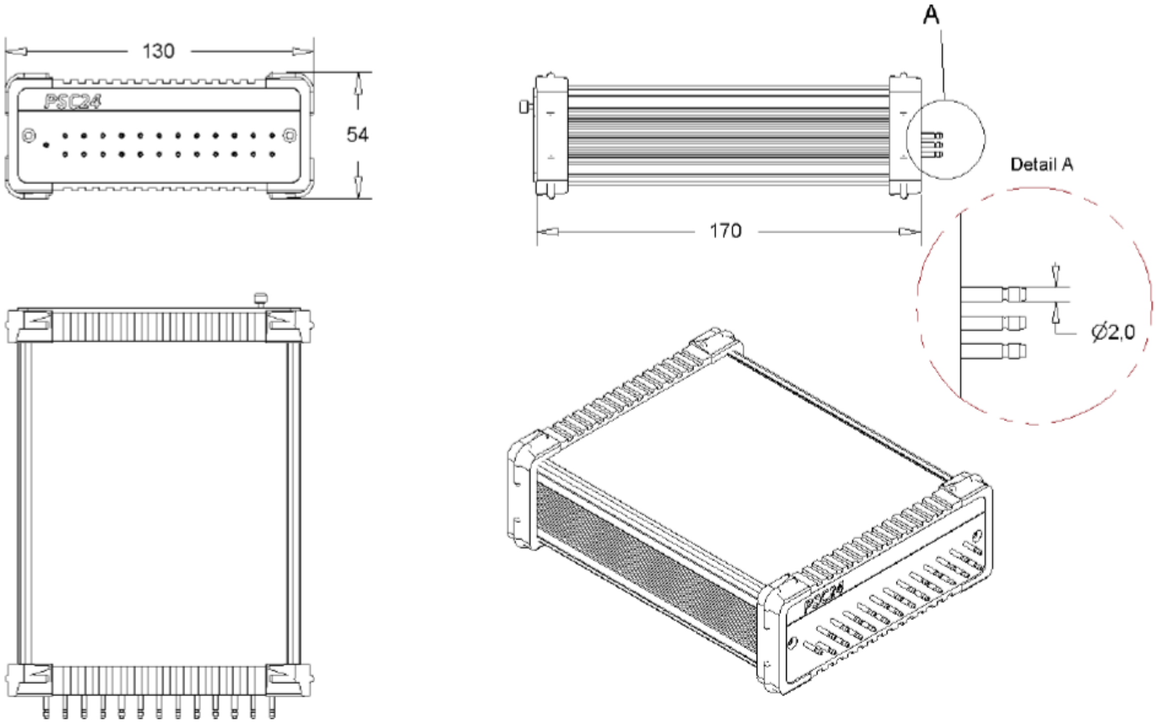

Figure 27: PSC24 pressure scanner [30]

8.2.1 Verification of Omniprobe's velocity accuracy - procedure

The 14-hole Omniprobe was calibrated by the supplier and supplied with calibration files. This study involved verification of the accuracy of the probe in terms of velocity of flow magnitude and flow angles. This activity was carried out in an open stream wind tunnel laboratory. The manufacturing tolerance of the probe support was at ±0.25º.

The verification required the design of a variable probe support system which would allow varying angular alignment of the probe with the flow field at the exit from the wind tunnel. The designed variable probe support allowed for the Yaw (β), Pitch (α) and Roll (φ) of the probe to be varied in 10º intervals with respect to the wind tunnel axis.

The verification process involved the use of the Pitot static tube positioned at the exit of the wind tunnel (Figure 28), the Orifice plate fitted in the wind tunnel and the 14-hole Omniprobe positioned at the wind tunnel exit.

The wind tunnel is fitted with a centrifugal fan at inlet, air flow straightener (honeycomb) and orifice plate. The mass air-flow rate through the tunnel was varied using a potentiometer to a maximum velocity of 29 m/s at exit of the wind tunnel.

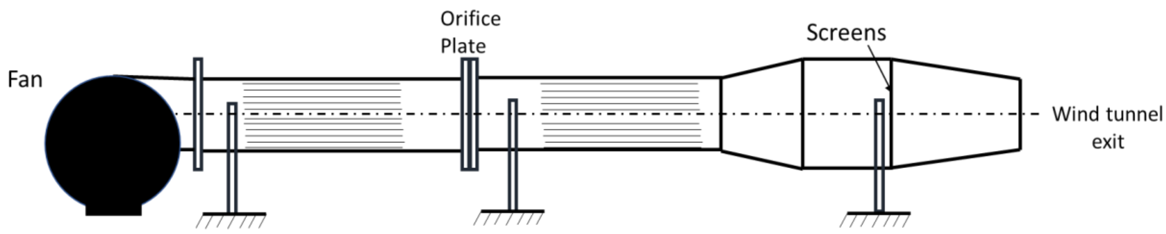

Figure 28: Open Stream Wind Tunnel

Using a Pitot-static tube, the velocity flow measurements were carried out across the exit diameter (152.5 mm) of the wind tunnel. The aim was to confirm that the velocity profile at the wind tunnel exit is even, at a constant fan speed. Figure 29 graphically illustrates the velocity profile at exit to the wind tunnel. The velocity profile was found to be well developed and even with the velocity varying by 0.4% across the diameter of the exit plane, along the horizontal and vertical axes.

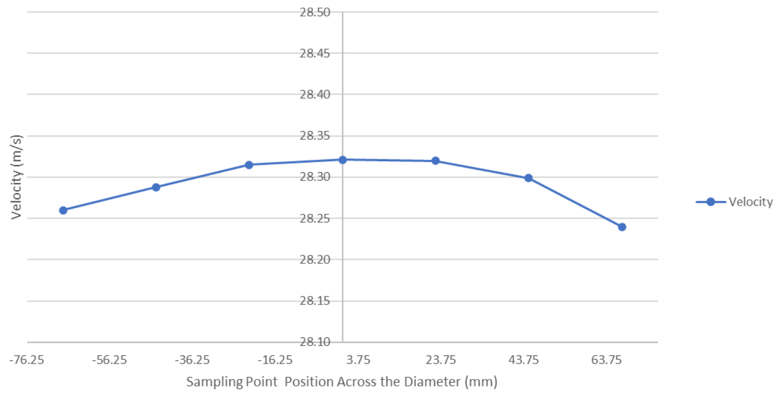

Figure 29: Velocity profile along the exit diameter of the wind tunnel

Figure 30 illustrates the experimental setup for verifying the accuracy of the velocity magnitude measured by the 14-hole Omniprobe against the standard Pitot static tube and Orifice.

1. The probe was mounted in the variable probe support and positioned at the exit plane of the wind tunnel, with the probe tip exposed to the exiting stream of air.
2. The 14-hole Omniprobe axis were aligned with the axis of the wind tunnel. This position was varied to verify the accuracy at different probe alignment relative to the wind tunnel axis.
3. The Pitot-static tube was fixed into position next to the omniprobe with the tip aligned to the axis of the wind tunnel. A digital manometer was used to measure the pressure difference.
4. The Orifice was also connected to a digital manometer to measure the differential pressure across the Orifice.
5. The fan was started and left to run until the flow stabilized. Stability was reached when the pressure difference measured by the Pitot-static tube and Orifice stabilised.

6. The atmospheric pressure read from the barometer was recorded together with temperature read by digital manometer.
7. Record the position of the probe with reference to the wind-tunnel axis.
8. The fan speed was adjusted by means of the potentiometer.
9. For a specific speed, the differential pressures connected to the Pitot-static tube and Orifice were recorded. At the same time, the 14-hole Omniporbe would sample the pressures on all 14 holes via the VectoVis program. 100 pressure readings were sampled per second for 10 seconds.
10. For the next Run, adjust the fan speed to the next increment and repeat steps 5 to 9. This is repeated until the maximum fan speed is reached. For this study, the air flow velocity was varied from 10 m/s to 29 m/s.
11. Switch off the wind tunnel and configure the 14-hole Omniprobe for the next orientation of the Omniprobe.

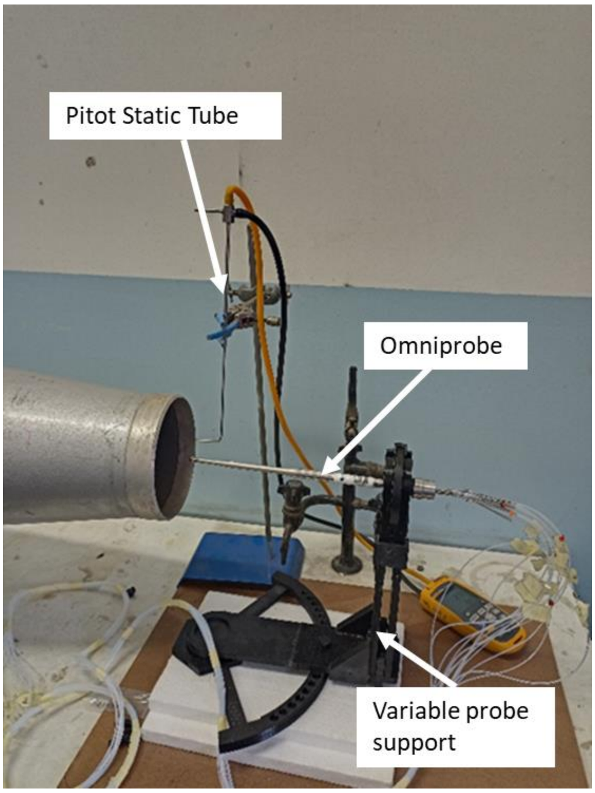

Figure 30: Variable probe support system, 14-hole Omniprobe and Pitot Static Tube at exit to wind tunnel

The aim of this experiment was to verify the accuracy of the probe at various angles of attack of the flow field with reference to the probe axis. The verification was conducted for a wide range of orientations of the 14-hole Omniprobe with reference to the wind tunnel axis.

8.2.2 Comparison of the results

8.2.2.1 Omniprobe orientation - Roll 30° and Yaw 155°

For this verification, the 14-hole Omniprobe was orientated such that the probe Roll was 30° and the Yaw was 155°, with respect to the wind tunnel axis. The velocity magnitude of the air flow at exit to the wind tunnel was varied from 10.6 m/s to 27.3 m/s for this experiment using the potentiometer. Figure 31 illustrates the mass-flow rates calculated from the velocity measurements by the Pitot-static tube, Orifice and 14-hole Omniprobe.

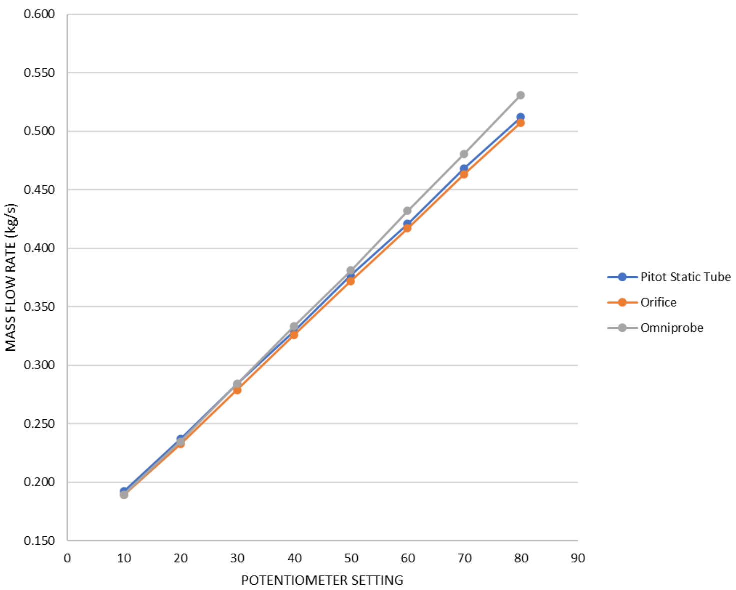

Figure 31: Mass flow rate at tunnel exit

Considering the Pitot Static tube and Orifice as a reference, the discrepancy of the Omniprobe measurement when compared with those of the Pitot-static tube and Orifice was found to be 3.68% at most (Table 1) at a potentiometer setting of 80.

Table 1: Mass flow comparison

Potentiometer Setting	Mass Flow rate - Pitot tube (kg/s)	Mass Flow rate - Orifice (kg/s)	Mass Flow rate - Omniprobe (kg/s)	Orifice vs Pitot tube (%)	Orifice vs Omniprobe (%)	Pitot tube vs Omniprobe (%)
10	0.192	0.189	0.189	-1.8	-1.6	-1.6
20	0.237	0.233	0.235	-1.9	-1.0	-1.0
30	0.284	0.279	0.284	-1.8	0.0	0.0
40	0.329	0.326	0.334	-0.9	1.3	1.3
50	0.377	0.372	0.381	-1.4	1.1	1.1
60	0.421	0.417	0.432	-0.9	2.6	2.7
70	0.468	0.463	0.481	-1.1	2.5	2.6
80	0.512	0.508	0.531	-0.9	3.6	3.7

8.2.2.2 Omniprobe orientation - Roll 0º and Yaw 55º

For this verification, the omniprobe was orientated such that the probe Roll was 0º and the Yaw was 55º, with respect to the wind tunnel axis. The velocity of the air flow at the wind tunnel exit was varied from 10.6 m/s to 28.3 m/s for this experiment using the potentiometer. Figure 32 illustrates the mass-flow rates calculated from the velocity measurements by the Pitot-static tube, Orifice and 14-hole Omniprobe.

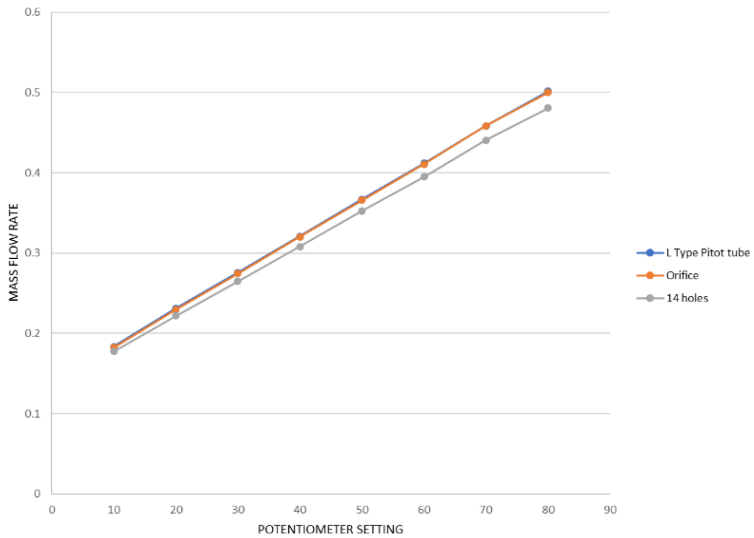

Figure 32: Mass flow rate at tunnel exit

Considering the Pitot Static tube as a reference, the discrepancy of the Omniprobe measurement when compared with those of the Pitot-static tube and Orifice was found to be -4.4% at most at a potentiometer setting of 80. The resulting mass flow rates for this configuration are tabulated in Table 2.

Table 2: Mass flow rate comparison

Potentiometer Setting	Mass Flow rate - Pitot tube (kg/s)	Mass Flow rate - Orifice (kg/s)	Mass Flow rate - Omniprobe (kg/s)	Orifice vs Pitot tube (%)	Orifice vs Omniprobe (%)	Pitot tube vs Omniprobe (%)
10	0.1835899	0.1824604	0.1775707	-0.6	-3.4	-3.3
20	0.23136955	0.2296772	0.222019	-0.7	-4.2	-4.0
30	0.27568466	0.2743699	0.2648753	-0.5	-4.1	-3.9
40	0.32108941	0.3203541	0.3079596	-0.2	-4.3	-4.1
50	0.36717979	0.3656717	0.3524784	-0.4	-4.2	-4.0
60	0.41212622	0.4105436	0.3949693	-0.4	-4.3	-4.2
70	0.45843445	0.458484	0.4406605	0.0	-4.0	-3.9
80	0.50179482	0.5002353	0.480747	-0.3	-4.4	-4.2

8.2.2.3 Omniprobe orientation - Roll 60º and Yaw 135º

For this verification, the Omniprobe was orientated such that the probe Roll was 60º and the Yaw was 135º with respect to the wind tunnel axis. The velocity of the air flow at the wind tunnel exit was varied from 9.95 m/s to 27.3 m/s for this experiment using a potentiometer. Figure 33 illustrates the mass-flow rates calculated from the velocity measurements by the Pitot-static tube, Orifice and 14-hole Omniprobe.

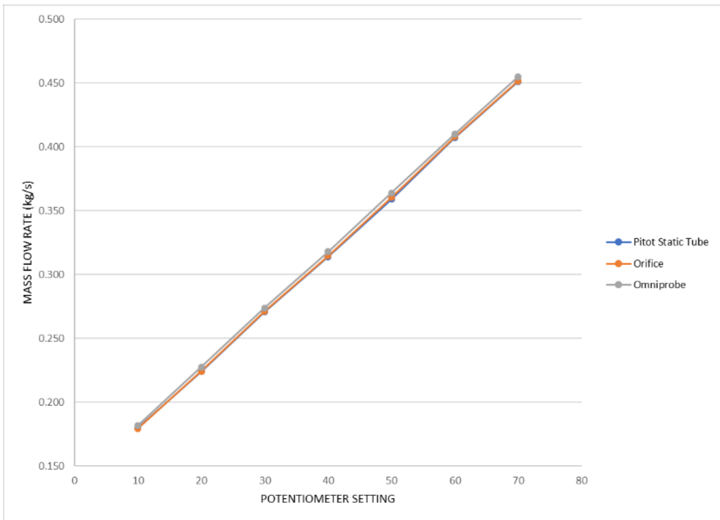

Figure 33: Mass flow rate at tunnel exit

Considering the Pitot Static tube and orifice as a reference, the discrepancy of the Omniprobe measurement when compared with those of the Pitot-static tube and Orifice was found to be 1.6% at most at a potentiometer setting of 20. The resulting mass flow rates for this configuration are tabulated in Table 3.

Table 3: Mass flow discrepancies – Roll 60º and Yaw 135º

Potentiometer Setting	Mass Flow rate - Pitot tube (kg/s)	Mass Flow rate - Orifice (kg/s)	Mass Flow rate - Omniprobe (kg/s)	Orifice vs Pitot tube (%)	Orifice vs Omniprobe (%)	Pitot tube vs Omniprobe (%)
10	0.180	0.179	0.182	-0.3	1.1	1.1
20	0.224	0.224	0.228	0.1	1.5	1.6
30	0.271	0.271	0.274	0.1	1.1	1.1
40	0.314	0.315	0.318	0.3	1.3	1.3
50	0.359	0.360	0.364	0.4	1.3	1.3
60	0.407	0.408	0.410	0.2	0.7	0.7
70	0.451	0.452	0.455	0.1	0.8	0.8
80	0.494	0.498	0.500	0.7	1.0	1.0

8.2.3 Verification of Omniprobe's angular accuracy - procedure

For this experiment, the probe support mechanism allowed to rotate about the probe head tip (i.e., origin of the coordinate sytem on the x-y plane refering to Figure 25) in intervals of 5º and 10º and the rotation of the probe about its Y-axis, i.e., varying the Roll in intervals of 10º.

Procedure:

1. The probe was mounted on the variable probe support and then connected to the pressure scanner via the air tubes (Figure 30).
2. Set the Roll of the Omniprobe to a fixed angle for the Yaw of 0º.
3. The atmospheric pressure was recorded from the barometer and temperature recorded from the digital manometers.
4. The axis of the Omniprobe were then aligned to align with the axis of the wind tunnel at the exit.
5. Zero (TARE) the pressure scanner.
6. Start the wind tunnel and let it run until the flow is stabilized i.e., the differential pressure measured by the Pitot-static tube and Orifice stabilised.
7. Adjust the fan speed using the potentiometer to a fixed value for the experiment.
8. Sample the pressure readings for this orientation.
9. The Roll was set to a specific value and remained unchanged for each run.
10. Vary the Yaw of the probe with respect to the wind tunnel axis in intervals of 10º, from 0º to 140º. At each succeeding interval, sample the pressure data.
11. Switch off the wind tunnel and configure the Omniprobe for the next orientation.

8.2.4 Verification of the angularity - Omniprobe

Verification of the angles as measured by the omniprobe was achieved by comparing the angles resulting from the Omniprobe's measurement with the calculated angles for a specific orientation of the Omniprobe with reference to the wind tunnel axis.

The variables of interest for verification were the:

- Yaw (β)
- Pitch (α)
- Roll (φ)
- Angle of attack (θ) also known as the conical angle.

Figure 34 illustrates the resulting Yaw (β), Pitch (α), Roll (φ) and the angle of attack (θ) from the Omniprobe's measurement. For this experiment, the Roll was fixed at 45º, and Yaw was varied from 0º to 150º at intervals of 10º, with reference to the wind tunnel axis at the exit plane. The pressure data was sampled at each interval and post-processed to yield the velocity magnitude (V), velocity components (u, v, w), Yaw, Pitch, Roll and Conical angle using VectoVis Pro 1.0 program. A sample of the results is included in Appendix 6 and 7.

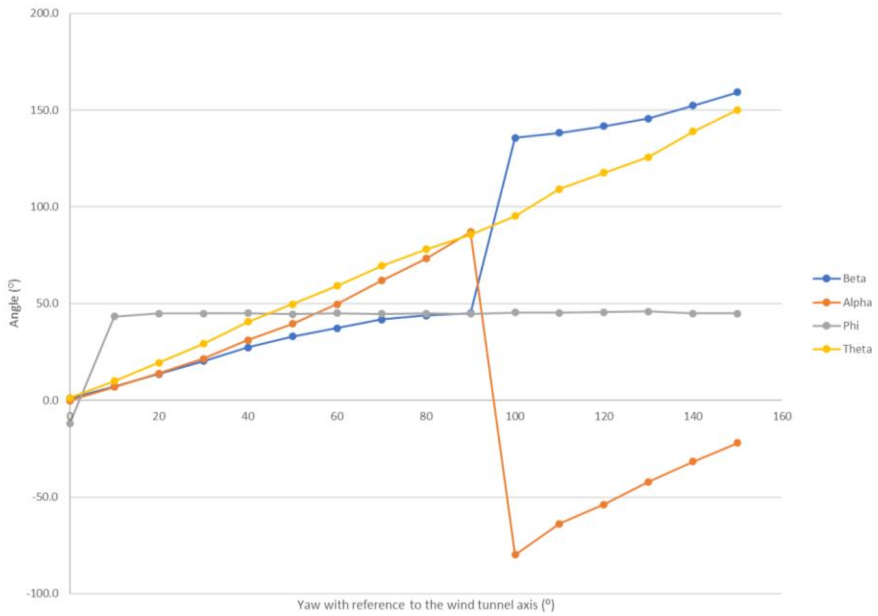

Figure 34: Angles as measured by the Omniprobe with Roll fixed at 45º

Figure 35 graphically illustrates the calculated Yaw, Pitch, Roll and Conical angle for a specific orientation of the Omniprobe with reference to the wind tunnel axis.

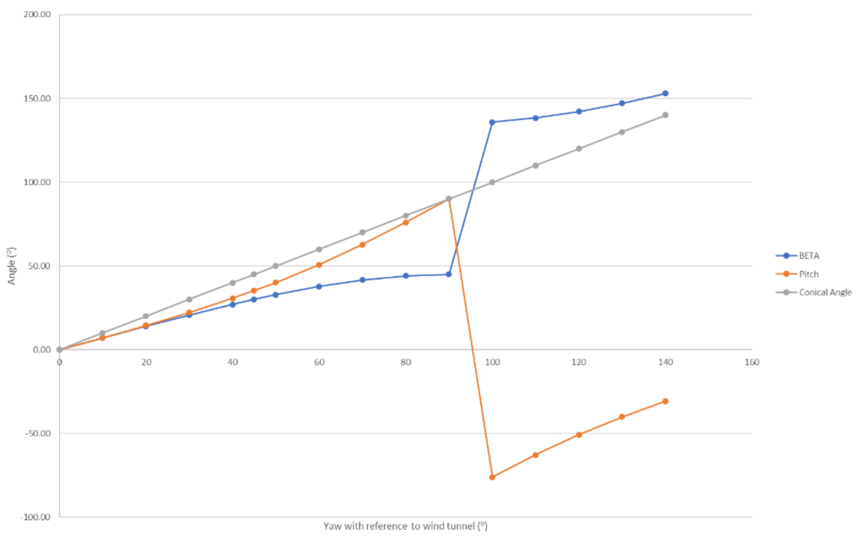

Figure 35: Angles as calculated with Roll fixed at 45º

The angles as measured by the Omniprobe and the angles from calculations are tabulated in Table 4. The table lists the Yaw and Pitch. The Roll was kept constant at 45º for this experiment.

Table 4: Angular Comparison – Rolled fixed at 45º

Wind Tunnel Yaw	YAW			PITCH		
	Yaw (Omniprobe)	**Yaw (Calculated)**	**Yaw Discrepancy %**	**Pitch (Omniprobe)**	**Pitch (Calculated)**	**Pitch Discrepancy %**
0	0.0	0.0	**-**	-0.1	0.0	**-**
10	7.2	7.1	**2.6**	6.9	7.1	**-3.6**
20	13.6	14.0	**-3.0**	13.9	14.4	**-3.8**
30	20.2	20.7	**-2.3**	21.5	22.2	**-3.5**
40	27.3	27.0	**1.0**	31.1	30.7	**1.4**
50	33.0	32.8	**0.6**	39.6	40.1	**-1.4**
60	37.3	37.8	**-1.2**	49.7	50.8	**-2.1**
70	41.7	41.6	**0.2**	61.9	62.8	**-1.5**
80	43.9	44.1	**-0.6**	73.3	76.0	**-3.7**
90	45.1	45.0	**0.2**	87.0	90.0	**-3.4**
100	135.6	135.9	**-0.2**	-79.8	-76.0	**4.8**
110	138.3	138.4	**-0.1**	-63.9	-62.8	**1.7**
120	141.6	142.2	**-0.4**	-53.9	-50.8	**5.8**
130	145.6	147.2	**-1.1**	-42.1	-40.1	**4.7**
140	152.3	153.0	**-0.5**	-31.6	-30.7	**3.0**
150	159.3	159.3	**0.0**	-22.1	-22.2	**-0.5**

Comparing the calculated results with the results as measured by the Omniprobe, a Roll discrepancy is noticed when the probe is orientated to be in line with the flow field, i.e., Yaw with refence to the wind tunnel axis is 0º. This is due to the flow direction being head on to the probe and parallel to the flow field, i.e., Yaw and Pitch are 0º.

The trajectory is not reflected on the calculated graphical results in Figure 35 since the Roll is a constant input for the calculation for the Yaw range of 0º to 140º. The discrepancy between the measured angles and the calculated angles was found to be below 5º, acceptable for this experimental setup when considering possible misalignments, vibrations and manufacturing tolerances.

Figure 36 illustrates the resulting Yaw (β), Pitch (α), Roll (φ) and the angle of attack (θ) from the Omniprobe's measurement. For this experiment, the Roll was fixed at 20º, and Yaw was varied from 0º to 150º at intervals of 10º, with reference to the wind tunnel axis at the exit plane.

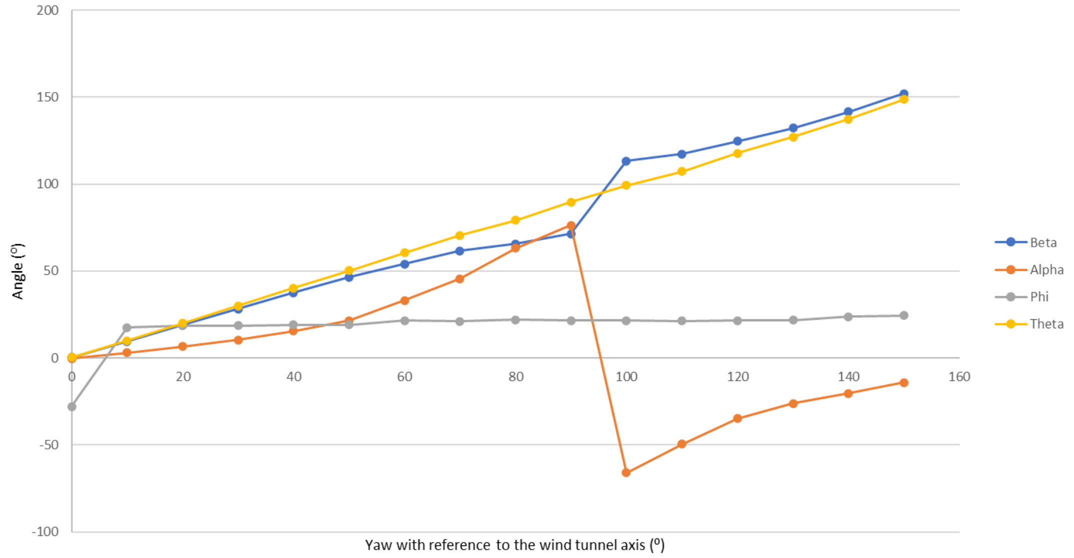

Figure 36: Angles as measured by the Omniprobe with the Roll is fixed at 20º

Figure 37 graphically illustrates the calculated Yaw, Pitch, Roll and Conical angle for a specific orientation of the Omniprobe with reference to the wind tunnel axis.

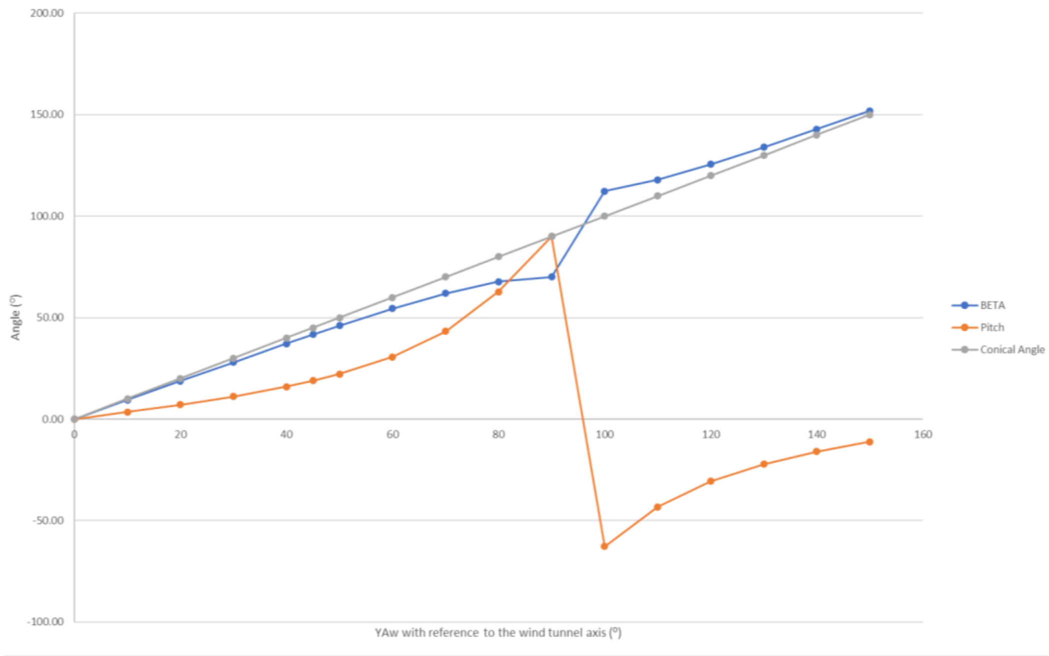

Figure 37: Angles as calculated with Roll fixed at 20º

The angles as measured by the Omniprobe and the angles from calculations are tabulated in Table 5. The table lists the Yaw and Pitch. The Roll was kept constant at 20º for this experiment.

Table 5: Angular comparison – Rolled fixed at 20º

Wind Tunnel Yaw	YAW			PITCH		
	Yaw (Omniprobe)	Yaw (Calculated)	Yaw Discrepency %	Pitch (Omniprobe)	Pitch (Calculated)	Pitch Discrepency %
0	0.0	0.0	**-**	-0.2	0.0	**-**
10	9.5	9.4	**0.7**	3.4	3.5	**-3.0**
20	18.9	18.7	**0.8**	6.9	7.1	**-2.8**
30	28.3	28.0	**0.9**	11.1	11.2	**-0.6**
40	37.5	37.2	**1.0**	15.4	16.0	**-3.8**
50	46.5	46.0	**1.0**	21.5	22.2	**-3.2**
60	54.1	54.5	**-0.7**	31.3	30.6	**2.1**
70	61.6	62.0	**-0.7**	43.3	43.2	**0.2**
80	65.7	67.7	**-3.1**	63.1	62.7	**0.6**
90	71.4	70.0	**1.9**	89.9	90.0	**-0.2**
100	113.3	112.3	**0.9**	-66.1	-62.7	**5.1**
110	117.3	118.0	**-0.6**	-43.1	-43.2	**-0.2**
120	124.6	125.5	**-0.7**	-30.5	-30.6	**-0.6**
130	132.2	134.0	**-1.3**	-21.9	-22.2	**-1.3**
140	141.7	142.8	**-0.8**	-15.8	-16.0	**-1.3**
150	152.0	152.0	**0.0**	-10.9	-11.2	**-2.5**

8.3 Five-hole Probe

This study also identified a five-hole probe and attempts to establish the viability of using it as a flow measuring device in highly distorted flows in comparison to the capability of the Omniprobe and the Pitot-static tube. Five-hole probes are designed and used for 3D flow field measurement of flow angles of +/-30º.

Five-hole probes are a robust and accurate tool that can measure the magnitude of all three velocity components. The probe also simultaneously measures the total and static pressure; all these variables can be obtained through calibration [31].

As part of this study, a five-hole probe with a “Cobra” shape had to be calibrated and verified to test its performance in highly distorted flow fields. The concept of a five-hole probe is like that of the fourteen-hole probe, the difference being the number of holes and how they are arranged.

For this reason, the measurement range of a five-hole probe is different from that of the fourteen-hole probe. Figure 38 illustrates of the actual Five-hole probe and Figure 39 is a schematic illustration of the five holes numbering.

Figure 38: Five-hole probe

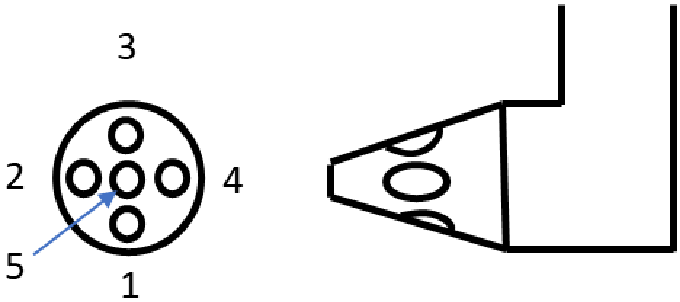

Figure 39: Hole numbering of the five-hole probe - Cobra shaped head

For the calibration process, a calibration rig (Figure 40) was designed and developed as part of the study. The calibration rig allowed for varying the Pitch in 5º intervals along the vertical plane coinciding with hole 1 and 3 and the Yaw in 10º intervals along horizontal plane coinciding with hole 2 and 4. The rig was manufactured to a tolerance of ±0.25º. The calibration process was carried out in the wind tunnel illustrated in Figure 34 for a range of +/-30º Pitch and Yaw directions with respect to the wind tunnel flow axis.

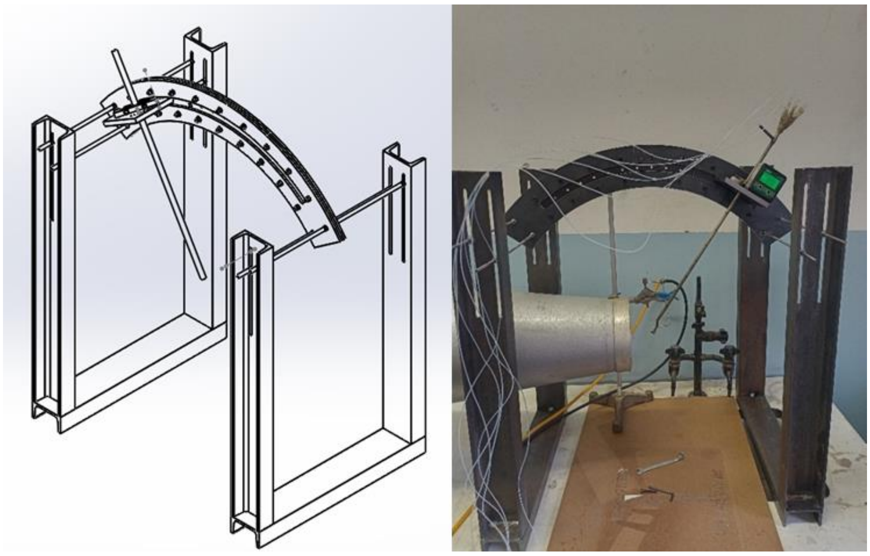

Figure 40: Calibration configuration of a five-hole probe

Before the calibration procedure, a traverse was conducted to confirm that the velocity flow profile at the wind tunnel exit along the x and y axis is flat using a Pitot-static tube as described in Section 8.2.1 of this report. A nun-nulling calibration technique which utilizes a database of calibration data, and a local interpolation technique is used for the interpolation of flow properties such as Cp_{β}, Cp_{α}, Cp_{0}, and Cp_{s}, Yaw coefficient (Cp_{β}) and Pitch coefficient (Cp_{α}), was used for this procedure. This type of calibration requires that the probe be exposed to a steady, uniform field of known velocity magnitude, flow direction atmospheric pressure, and temperature [31].

The calibration procedure involved positioning the probe in the flow field at defined set of angle combinations of Yaw (β) and Pitch (α) that cover the range of ±30º. At every angle combination of β and α, the pressures measured by the 5 holes together with the static and total pressures measured by a Pitot-static probe were recorded. The resulting data matrix was then used to calculate pressure and calibration coefficients of the Five-hole probe. Pressure measurements were carried out by using a Multichannel Scanner PSC16. The data sheet of this device is included in appendix 5.

The convention used for numbering the holes for this study is illustrated in Figure 39. Holes 1 and 3 lie on the Pitch plane and holes 2 and 4 lie on the Yaw plane.

8.3.1 Calibration procedure of a Five-hole probe

1. The Five-hole probe was mounted the calibration rig and connected to the pressure scanner to capture pressure data at each orientation of the probe. Five pressure channels were used for the Five-hole probe.
2. A Pitot-static tube was positioned next to the tip of the Five-hole probe. The Pitot tube was used to measure static and total pressures; two pressure channels were used for this probe.
3. The axis of the Five-hole probe were aligned with those of the wind tunnel at exit.
4. The atmospheric pressure and temperature were recorded.
5. Set the Yaw and the Pitch of the Five-hole probe at a particular configuration and record. For this study the initial Yaw and pitch were both set at -30°.
6. Zero or Tera the pressure scanner.
7. The wind-tunnel fan was started and ran until the flow is stabilized, i.e., the pressure difference as measured by the Pitot-static probe and Orifice stabilised.
8. The fan speed was set to a fixed starting value and pressure readings were sampled by the 2 probes for the configuration using VectoVis Pro 1.0 program.
9. The fan speed was increased in interval of about 5 m/s until maximum speed of 25 m/s was reached. In each interval, the pressures readings were sampled by the two instruments.
10. Vary the Pitch setting by 10° while the Yaw is remains unchanged and repeat steps 6 to 9.
11. When all the Pitch angle settings (i.e., from -30° to 30° in intervals of 10°) have been sampled, with the Yaw angle setting which remained unchanged so far. The Yaw angle was then changed by 10° (for this experiment the next Yaw setting was -20°) and repeat Stages 6 to 10.
12. The procedure was repeated for the Yaw and Pitch combination range.
13. Switch off the wind tunnel fan.

From the calibration data matrix, the Yaw Cp_β and Pitch Cp_α coefficients and can be calculated Equation 23 and 24.

To address the error between static and stagnation pressures used, the total pressure coefficient Cp_0 and static pressure coefficients Cp_s are calculated using Equation 25 and 26.

From the recorded four coefficients Cp_β, Cp_α, Cp_0, and Cp_s at each β and α setting or probe position, four piecewise functions may be derived from Equation 27-30.

From the plot of coefficients of Pitch and Yaw in Figure 41, fourteen polynomials to the order of 3 were derived by fitting a trendline for specific Yaw or Pitch setting from the calibration data. For the present study, Excel was used and 14 polynomials were derived from Figure 41.

These polynomials are specific for this probe only due to varying manufacturing tolerance for a specific probe.

Given any set of pressures in an unknown angle of attack and magnitude, the coefficients Cp_β and Cp_α can be determined using equation 23 and 24. With Cp_β and Cp_α, the flow angles β and α can then be obtained by curve fitting and interpolation.

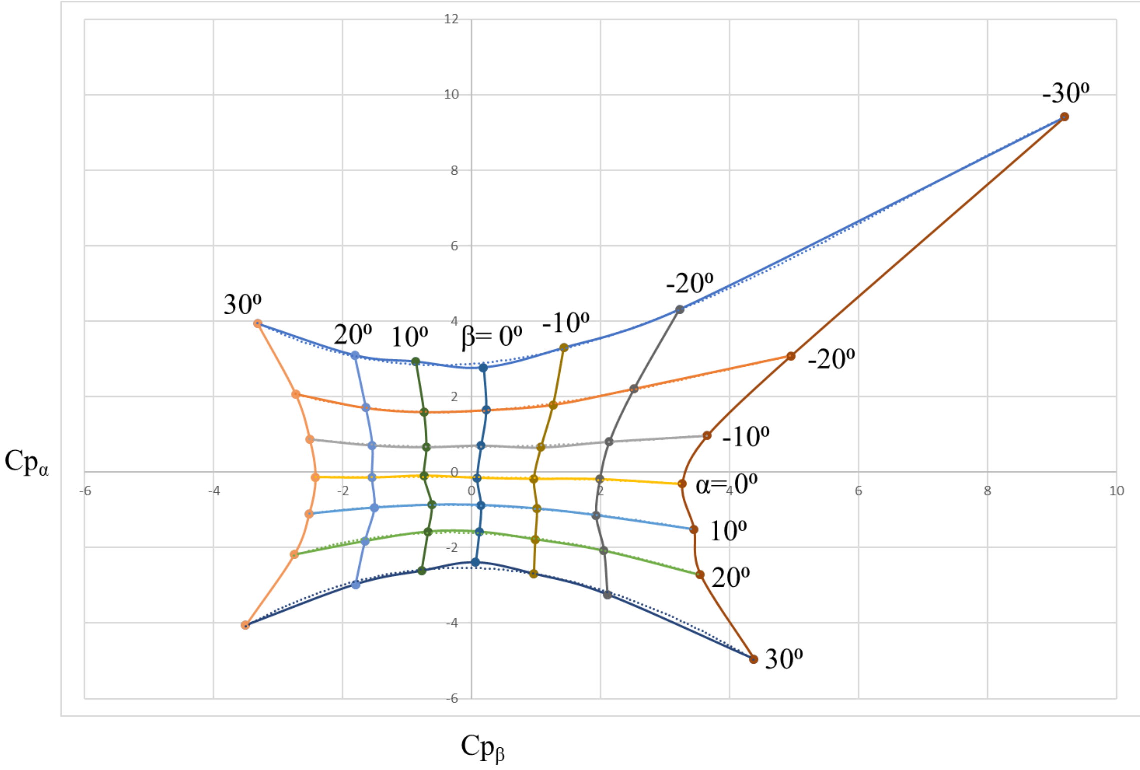

Figure 41: Coefficients of Pitch and Yaw for the Five-hole probe

To calculate the velocity magnitude for the given Yaw (β) and Pitch (α) as obtained above, Total Pressure Coefficient (Cp_0) and Static Pressure Coefficient (Cp_s) can be derived by curve fitting interpolation.

From Figure 42, seven polynomials can be derived for use in calculating Cp_0, through curve fitting and interpolation. Similarly, from Figure 43, seven polynomials can be derived for use in calculating Cp_s.

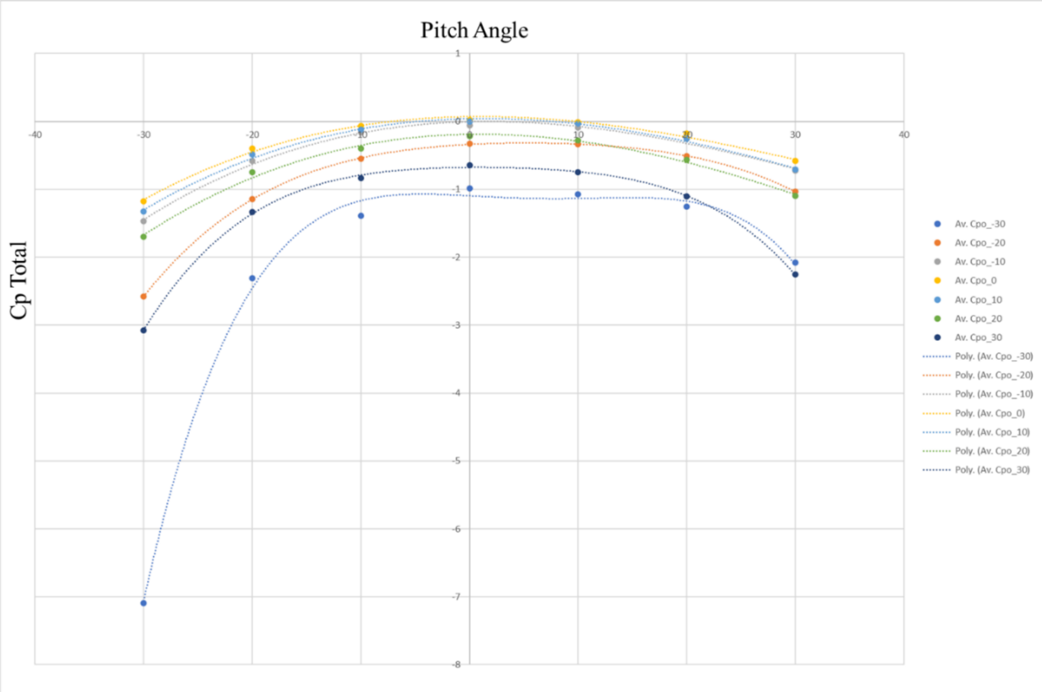

Figure 42: Total Pressure Coefficient vs Pitch Angles – lines of constant yaw

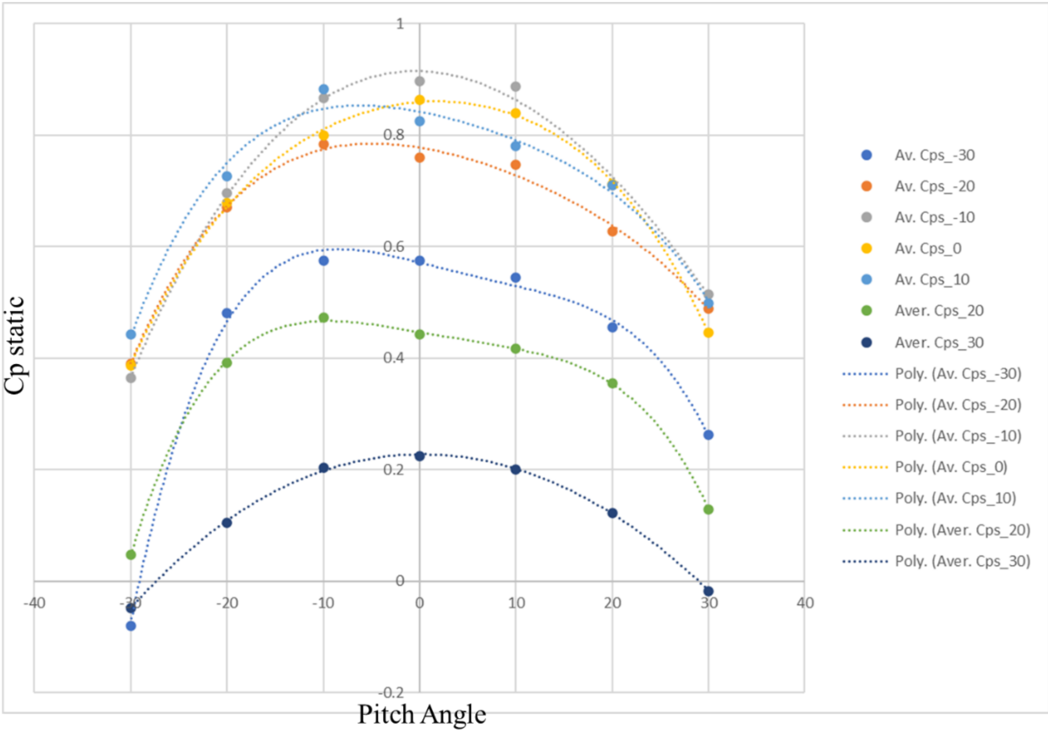

Figure 43: Static Pressure Coefficient vs Pitch Angles - lines of constant yaw

With the four coefficients calculated, the magnitude of the velocity can be calculated using equation 29 below (recalled from literature review), recalled from the literature review.

$$|V| = \left(\frac{2}{\rho}(P_5 - \bar{P})\left(C_{ps} - C_{p0} + 1\right)\right)^{1/2} \tag{31}$$

Equation 30, 31 and 32 recalled from literature review, the relationship between the velocity components (v, u, w), and the flow angles (α, β, φ, θ) is such that [31]:

$$u = |V|cos\alpha \cos\beta = |V|cos\theta \quad (32)$$

$$v = |V|sin\alpha = |V|sin\theta sin\varphi = |V|sin\alpha \quad (33)$$

$$w = |V|cos\alpha cos\beta \quad (34)$$

Where β is the Yaw, α is the Pitch, θ is the conical angle or angle of attack and φ is the probe roll. A sample calculation is included in the Appendix 2.

8.4 Air Flow Duct Prototype

The aim of the study is to establish the accuracy of the multi-hole probes in aligned flow fields, in turbulent sections and sections where the flow is recovering. This capability will assist in modeling velocity flow profiles in large square industrial ducts. With defined velocity profile, measurement planes, the calibration and application of online measuring instrument will be possible.

A scaled down air-flow duct model (Figure 44) was designed and fabricated to simulate highly uniform, recovering and distorted air-flow patterns for modeling and analysis. Highly distorted air-flow profiles are expected to be encountered in large-square industrial ducts in boiler plants and other industrial applications.

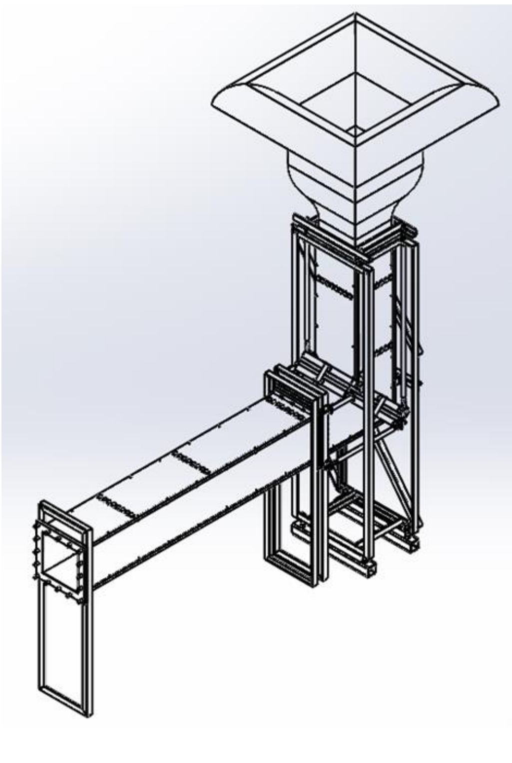

Figure 44: Air flow duct 3D Model

The model was designed such that there would be a section where the velocity profile would be uniform. This section of the duct would serve as a reference section for the mass flow rate through the duct model. The cross-sectional area of the duct model was designed to be of square section (305 mm x 305 mm).

A 90º bend was included in the design to disturb the uniform flow field. Downstream, post the 90º bend, a 2.3 m length of duct was designed to allow for the recovery of the air-flow velocity profile.

Figure 45 illustrates the assembly of the of the duct model. A centrifugal fan was connected at exit of the air duct prototype. Air would be drawn into the square duct by the centrifugal fan through the nozzle fitted at inlet. The nozzle was fitted with honeycomb for the purpose of aligning the flow at the duct inlet section. Perspex glass and wood were selected material for the walls of the wind tunnel.

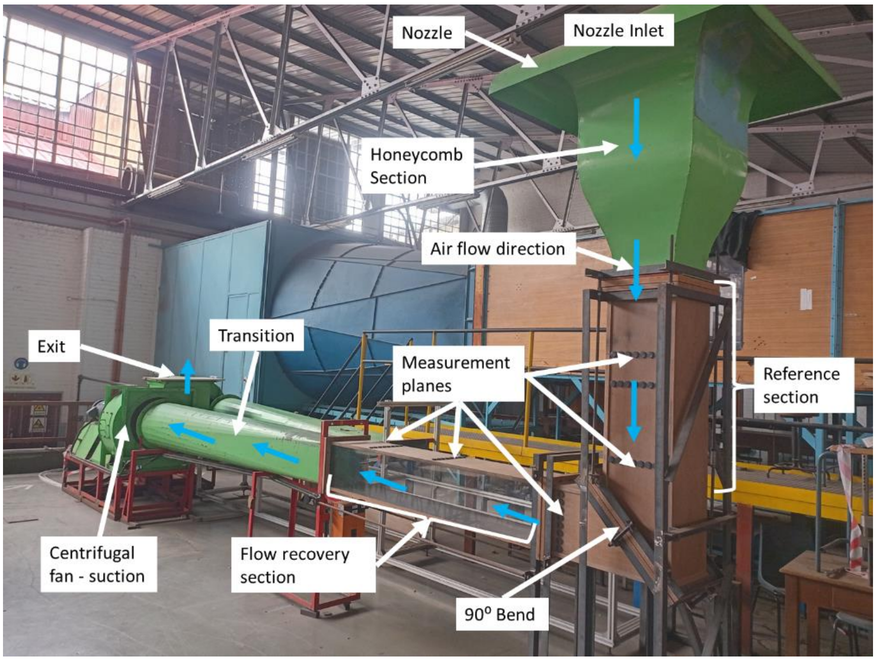

Figure 45: Air Flow Duct Prototype

The air flow duct model was designed with the aim of profiling the velocity profiles at six cross-sectional areas of the duct prototype; the 1st and 2nd cross-sectional areas are situated in a section where the flow is expected to be one directional and uniform. The 3rd and 4th cross-sectional areas are positioned just after the 90º bend, with the 5th and 6th planes positioned in the recovery section.

Figure 46 illustrates the six planes of interest for this study. The expected velocity flow profiles at the cross-sectional planes of interests are summarised as follows:

- At plane 1 and 2, the flow was expected to be uniform and mostly one-directional. The velocity profile was expected to be flat at these two planes.
- At plane 3 and 4 downstream, the flow was expected to be highly distorted and multi-direction due to the flow disturbance resulting from the 90º bend. Reverse flow was expected in some areas of the cross-sections. The Pitot-static tube would not applicable in these two planes due to the complex flow field.
- At plane 5, the flow is expected to be recovering with no reverse flow.
- At plane 6, the flow is expected to have improved, one direction with the velocity profile recovering.

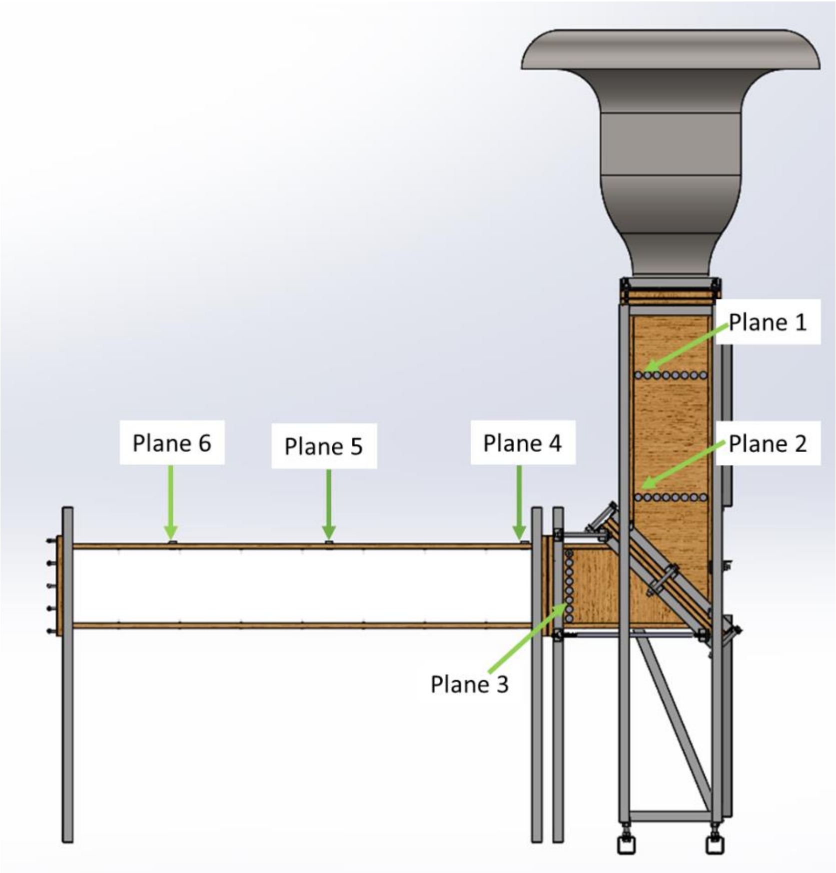

Figure 46: Cross-sectional planes of interest

Figure 47 illustrates the positions of the planes of interest for the current study.

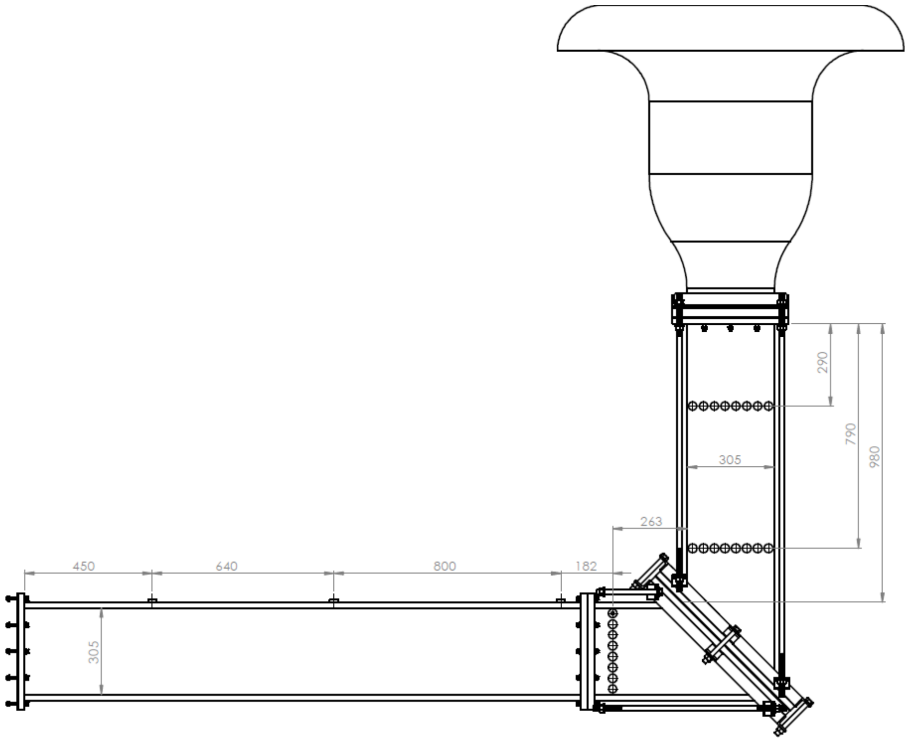

Figure 47: Six Traverse Planes Locations

The equal area method was adopted for this study. This involved dividing the cross-sectional area into equal areas. The traverse measuring grid consisted of 64 points for measurements as illustrated in Figure 48.

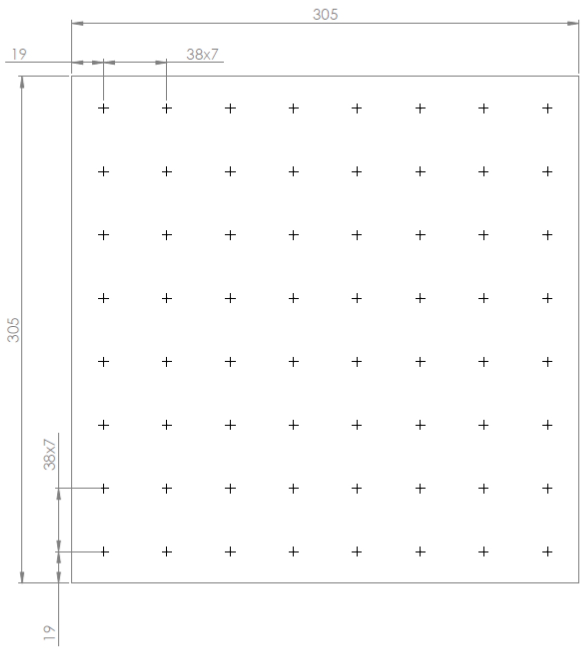

Figure 48: Sampling point positions in square duct

8.4.1 Procedure for taking measurements on the transverse points.

- It was ensured that all tapping holes were sealed using the supplied plugs.
- Ensured that there were no obstructions at inlet and exit of the air duct prototype.
- The probe was mounted on the probe supporting rig and the axis of the probe were set to be parallel with the axis of the air duct prototype by using levels, inclinometers and engineer's square.
- The pressure scanner was connected to the probe.
- Zero or Tera the pressure scanner.
- The wind-tunnel was set to a predefined value and fixed for the duration of the experiment.
- Pressure readings were sequentially sampled at all 64 points of the measuring grid.

Figure 49 below illustrates the setup of a traverse of plane 2 using the 14-hole Omniprobe.

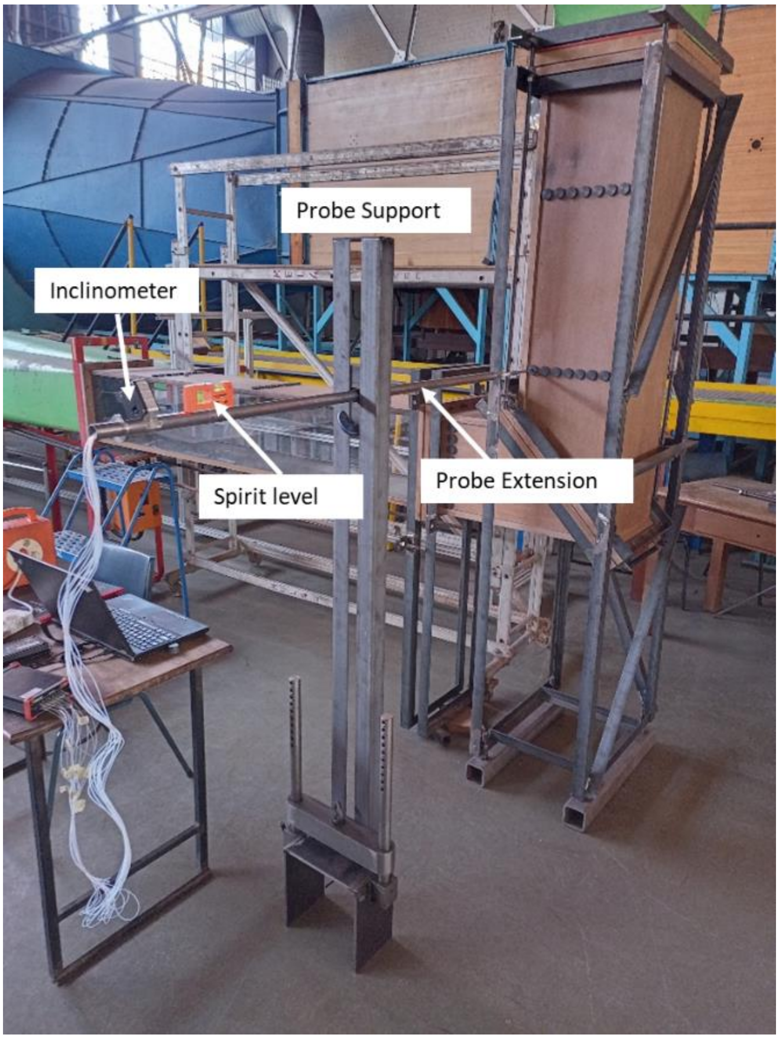

Figure 49: Experimental setup of 14-hole Omniprobe traverse of plane 2.

Figure 50 illustrates setup of the five-hole probe traverse of plane 5.

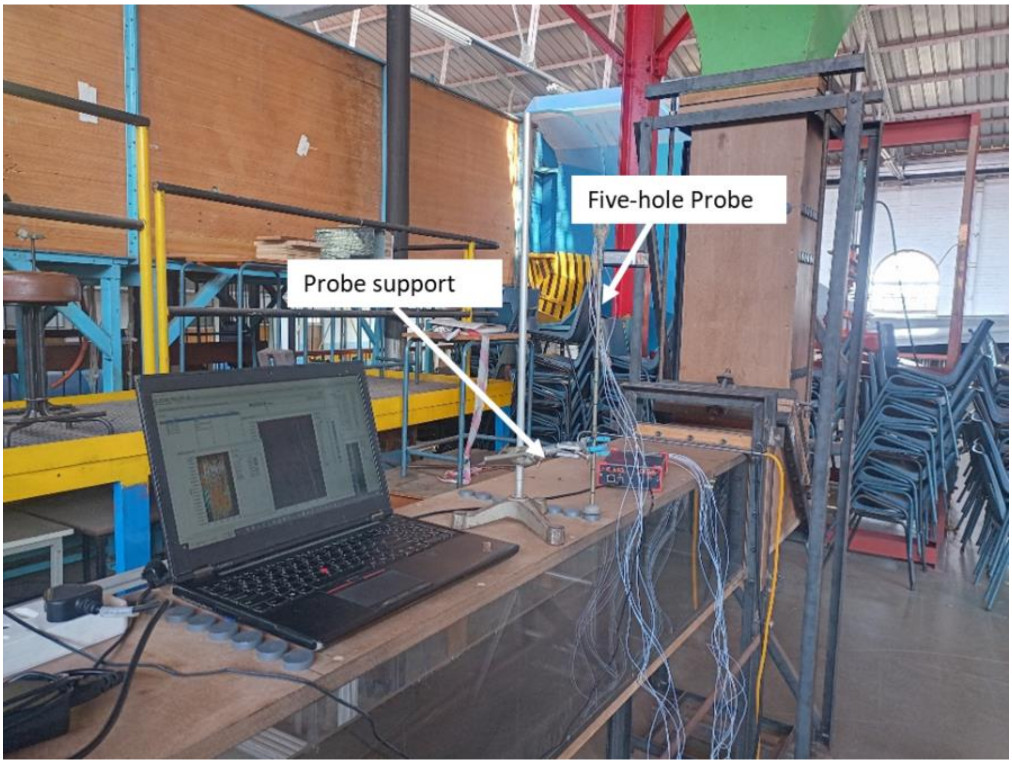

Figure 50: Experimental setup of Five-hole probe traverse of plane 5

Figure 51 illustrates the setup of a Pitot Static Tube traverse plane 2.

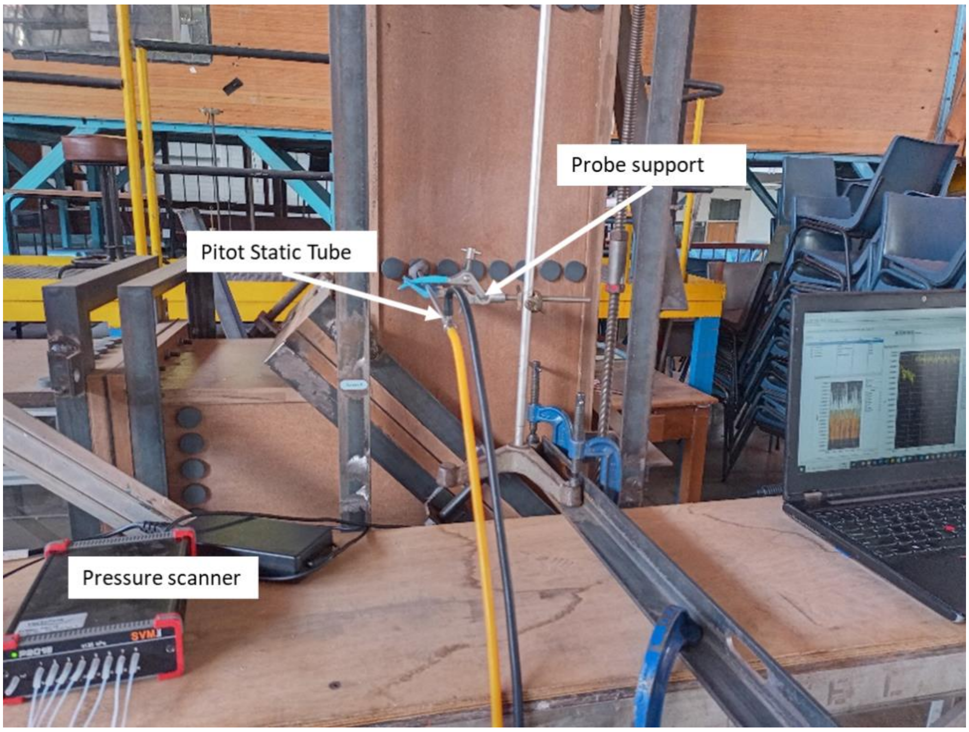

Figure 51: Experimental setup of Pitot Static Tube traverse plane 2

8.5 Computational Fluid Dynamics

The advancement in technology has seen Computational Fluid Dynamics being a well-established and efficient tool of choice in research and design, simulating and solving problems involving the electrostatics, stress analysis, acoustics, fluid dynamics, heat transfer, and chemical reactions to list just a few.

The present study involves a phenomena of fluid dynamics through an duct prototype. The geometry of the wind tunnel was generated using SolidWorks and imported into ANSYS Fluent for analysis. ANSYS meshing software was used to generate a mesh or grid suitable for simulating air fluid flow accurately and effectively through the air duct.

Generating a high-quality mesh or grid is the foundation of accurate engineering simulation as the quality of the mesh impacts the accuracy, precision, and speed of the convergence of the solutions. Figure 52 illustrates the computational fluid domain for the study.

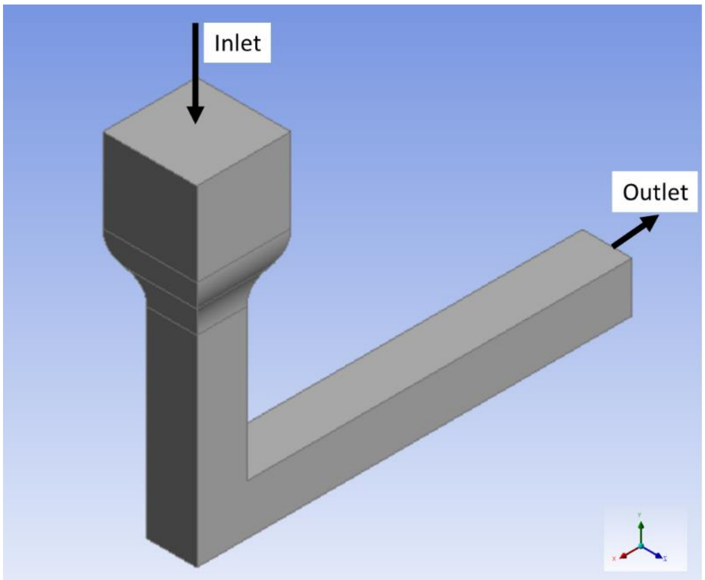

Figure 52: Computational fluid domain

The computational domain and governing equations were discretized through Meshing using Fluent. In generating the mesh for the geometry, Tetrahedrons were applied for the discretization of the domain. Due to the no-slip condition between the duct walls and air fluid flow, the flow field is non-uniform.

The Mesh was refined by Edge sizing the edges where the walls make a 90^{o} turn (Figure 53). This improved the quality of the mesh locally at these edges identified as challenging regions of the geometry.

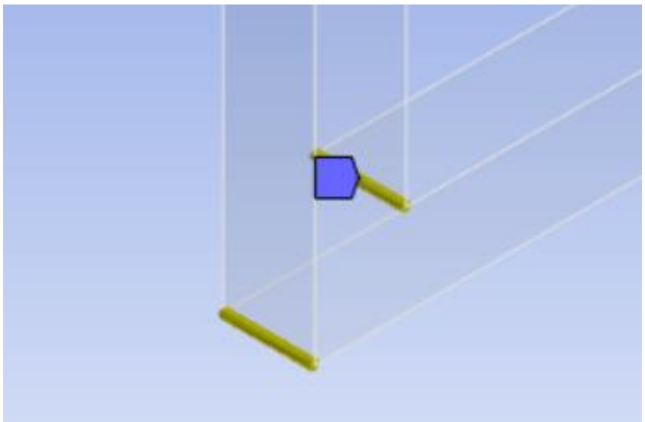

Figure 53: Edge sizing

The quality measure of a mesh is indicated by the skewness which indicates how close to ideal an element is. It is generally recommended to keep the skewness to below 0.7, best value being 0 (zero).

The orthogonal quality of the mesh was found to be 1.38301e-01 which is greater than the minimum threshold of 0.1, this indicated that the quality of the mesh was good.

To further improve the quality of the mesh, inflation with a maximum of 10 layers was added to the walls of the air duct model. The mesh spacing by the wall needs to be sufficiently fine to resolve the steep velocity gradient in the boundary layer closer to the walls.

For the current study, the k-ε turbulence model was selected. The enhanced wall function was selected as it extends the turbulence model beyond the viscous layer. Figure 54 illustrates the mesh.

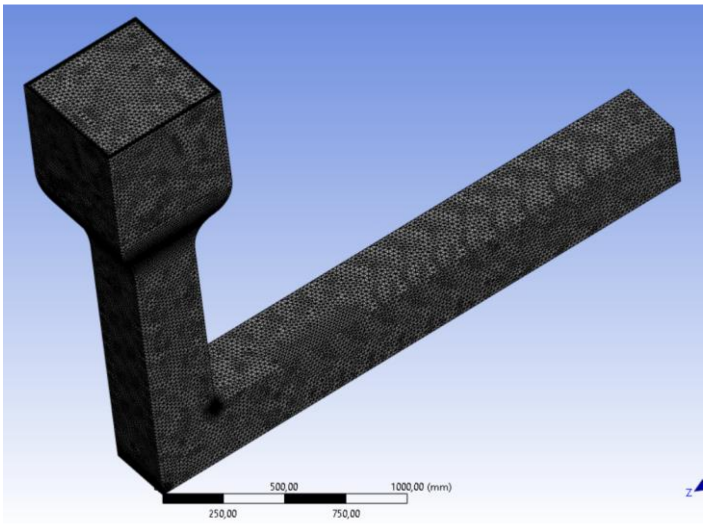

Figure 54: Mesh

For this study,

- Pseudo-transient formulation of pressure based coupled solver was used.
- The viscous model for the simulation is k-ε (epsilon) realizable. Near wall treatment was selected with curvature correction.
- Under materials, air was selected with constant density for the simulation.
- In the boundaries condition, the inlet velocity was set to 4.8 m/s. The walls of the wind tunnel are modeled as no slip, stationary wall.
- In the solutions tab, coupled scheme was selected. The turbulent Kinetic Energy and Turbulent Dissipation rate were set to second order upwind.
- In the controls tab, under pseudo time explicit relaxation factors, default values were unchanged.
- Default values were left unchanged under residual monitors.
- Under monitors, the mass flow rate was monitored through the simulation process at inlet.
- The simulation was initialized using hybrid initialization.
- The simulation ran successfully converging just at about 210 iterations.

Figure 55 illustrates the velocity vector plot derived from ANSYS Fluent through the wind tunnel. The flow is uniform and mostly one directional across plane 1 and 2. In plane 3 and 4, the flow is highly distorted due to the 90º bend as there is reverse flow in that region of the duct. In plane 5 the flow is recovering from the disturbance, though still highly distorted. At plane 6, the flow has not fully recovered but improved from the disturbance.

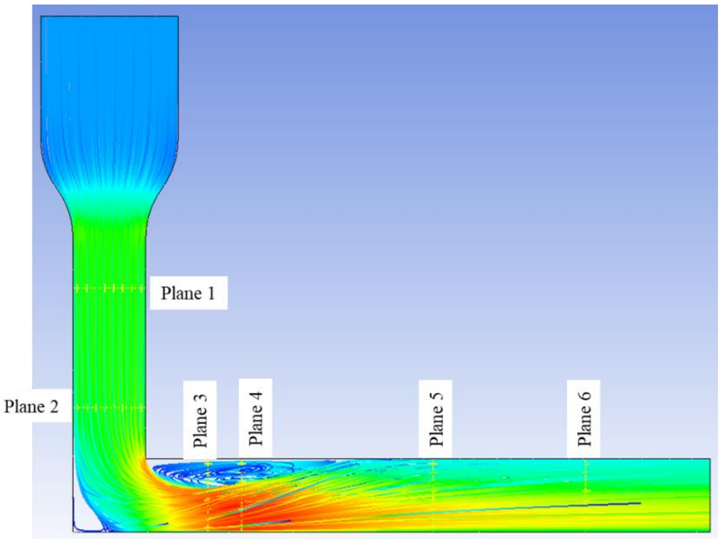

Figure 55: Flow streamline through the wind tunnel.

Figure 56 is a close-up view of the velocity vectors before and after the 90⁰ degree flow disturbing bend. From the figure. The Omniprobe will be tested at plane 3 and 4 for its capability to measure reverse flow. From Figure 56 of the CFD (ANSYS Fluent) postprocessing analysis, the flow in this region is highly distorted.

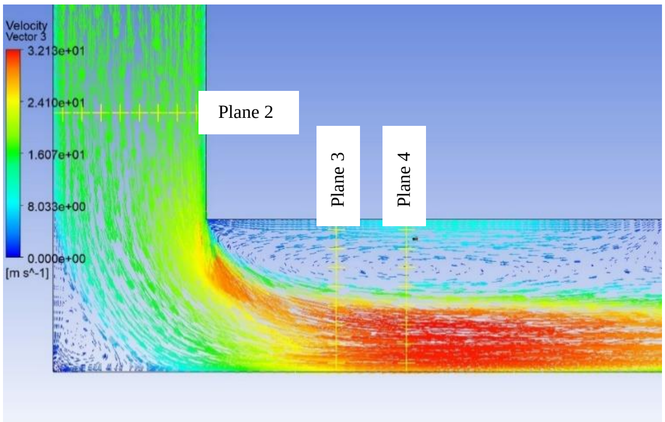

Figure 56: Close-up view of the velocity vectors at the 90⁰ bend

9. RESULTS AND DISCUSSIONS

For the present study, numerical and experimental investigations using Pitot-static probe, Five-hole probe and the14-hole Omniprobe were conducted. Plane 1 is located at 290 mm from duct entry, and Plane 2 is located at 500 mm from plane 1 and 100 mm from the 90⁰ flow disturbance. Plane 3 is located at 260 mm from the 90⁰ turn.

Plane 4 is 445 mm from the 90⁰ turn, Plane 5 is 1.245 m from the 90⁰ turn, and Plane 6 is 1.885 m from the 90⁰ turn and 450 mm before the wind tunnel exit as illustrated in Figure 46 above. At entry plane 1 and 2 the flow is even. A flow disturbance by means of a 90⁰ turn is introduced at $3D_h$ and the exit is at $6.2D_h$ from the disturbance. The flow is expected to be recovering from the disturbance towards the duct exit.

Figure 57 illustrates the model coordinate system adopted for the experiment and simulation for this study. With reference to the air duct axis, the velocity components u, v, and w are along the x, y, and z axis respectively. For plane 1 and 2, the velocity component of interest orthogonal to the x-z plane is "v". For planes 3, 4, 5, and 6 which are parallel to the x-y plane, the velocity component of interest is "w" which in orthogonal to the v-y plane.

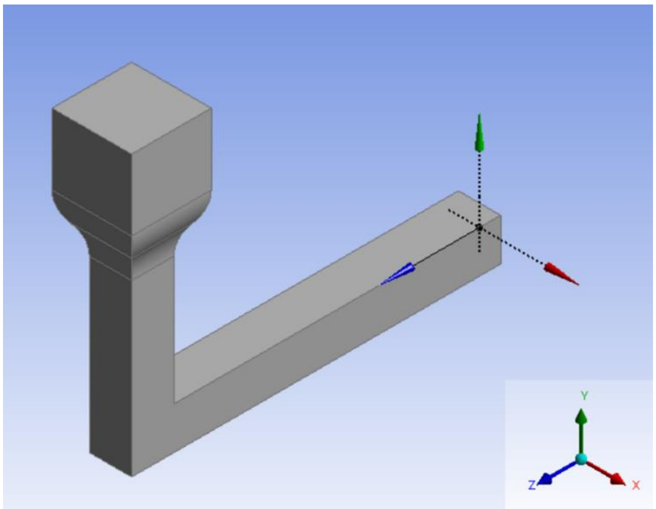

Figure 57: Coordinate system

The coordinate system of the probe differs from the coordinate system of the air duct prototype. The coordinate system of the Omniprobe is illustrated in Figure 25.

In this chapter, the planar CFD and experimental results are presented and discussed. The equal area method was applied experimentally and in ANSYS Fluent simulation at planes 1 to plane 6 to calculate the mass flow rate in kg/s for analytical comparison. The cross-sectional area was divided into an 8*8 grid of equal areas (38.125 mm x 38.125 mm) as described in Figure 48.

The velocity flow rate was monitored by means of a Pitot Static which was kept in position in plane 1 throughout the experiment to monitor drift. The resulting mass flow rates calculated from using the Pitot Static Probe in plane 1 and 2 would be a reliable indication of the air mass flow rate through the duct. With an uncertainty of +/-0.5%, the Pitot Static probe yields reliable and repeatable measurements in regions where the flow is uniform, for this reason the measurements by the Pitot Static Probe in plane 1 and plane 2 would yield reliable measurements which served as a reference flow rate for the current study.

The resulting mass flow rates downstream are calculated and the velocity profiles modelled from measurement results of the Pitot-static tube. These are analytically compared with the mass flow rates and velocity profiles derived from the measurement results of the traverse measurements by the Omniprobe, Five-hole probe, and CFD.

For plane 1 and 2, maximum velocity (v_{max}) and minimum velocity (v_{min}) are noted with mean velocity (v_{mean}). The maximum relative velocity difference $((v_{max})\text{-}(v_{min}))/v_{mean}$ is an effective factor to indicate the uniformity of the velocity profile in the cross-sectional area.

9.1 Plane 1 - Results

Plane one is located 290 mm from duct inlet and 700 mm from the 90° bend. Flow is expected to be uniform on this plane as it is aligned from the nozzle by the honeycomb. The 90° flow disturbing bend did not influence the velocity profile at this location (plane 1). The mass flow rate measured at this plane provides a good reference of the mass flow throughout the duct length and is expected to be constant due to conservation of mass.

The duct panel interfaces and joints were sealed with an air seal to avoid air leakages. Figure 58 illustrates the velocity vectors across plane 1, the yellow asterisks indicate the traverse points on this plane. From the simulation the flow was one directional and uniform across this plane.

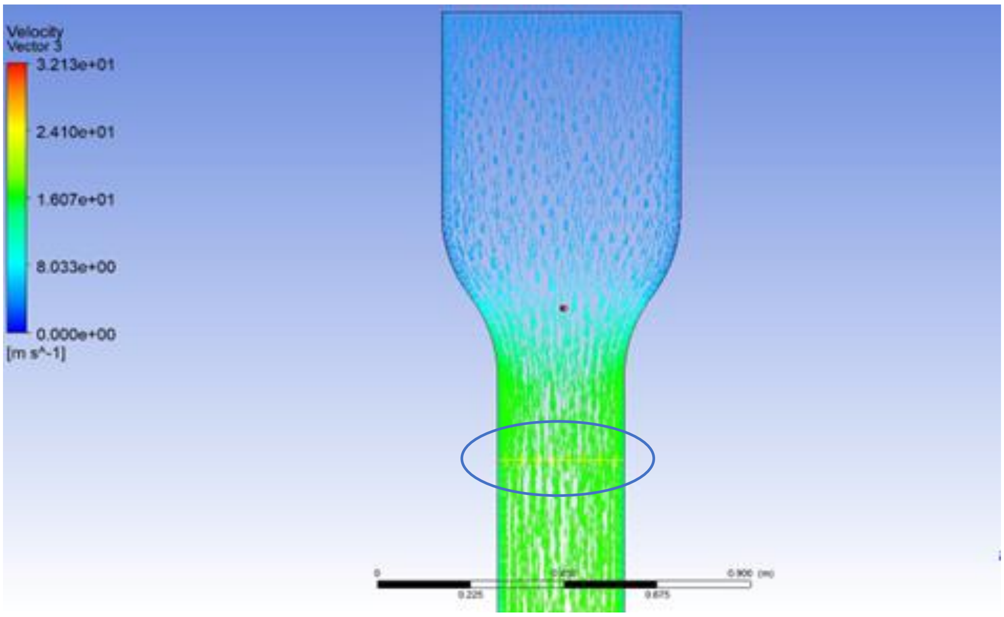

Figure 58: Velocity vectors at Plane 1

9.1.1 Pitot Static Probe Traverse results – Plane 1

Figure 59 illustrates the velocity profile resulting from the traverse measurements of plane 1 using a Pitot Static tube. The equal area method is applied at plane 1 and the velocity component of interest for the calculations is 90° to the plane 1.

The traverse velocities as measured by the Pitot Static Probe ranged between a minimum velocity $v_{min)}$ of 16.6 m/s to a maximum velocity ($v_{max)}$ of 17.1 m/s) with the mean velocity (v_{mean}) calculated to be 16.92 m/s; and the mass flow rate was calculated to be 1.54 kg/s. The velocity profile is flat considering the maximum relative velocity variance form the mean is calculated to be 2.9% and considering measurement uncertainties of the Pitot-static tube of +/- 0.8%.

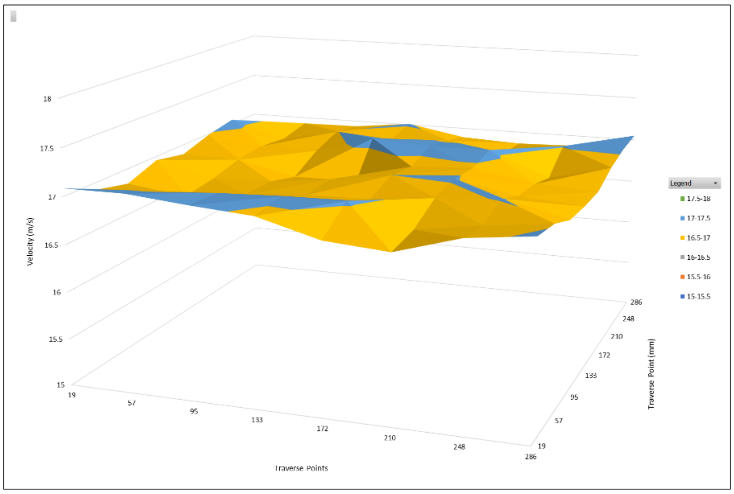

Figure 59: Velocity profile at Plane 1 using Pitot Static Tube

9.1.2 CFD – Plane 1

Figure 60 illustrates the velocity profile generated from ANYS Fluent. A traverse like that of the Pitot Static Probe above was conducted in ANSYS Fluent by probing the points in the CFD model. The velocity of interest for this experiment is the orthogonal to plane 1, this is the v-component from the simulation.

The velocity ranged from a minimum velocity (v_{min}) of 16.93 m/s to maximum velocity (v_{max}) of 17.02 m/s. The mean velocity (v_{mean}) was calculated to be 16.96 m/s and the mass flow rate was calculated to be 1.59 kg/s. The maximum relative velocity difference factor was calculated as 0.53% indicating a flat velocity profile on this plane.

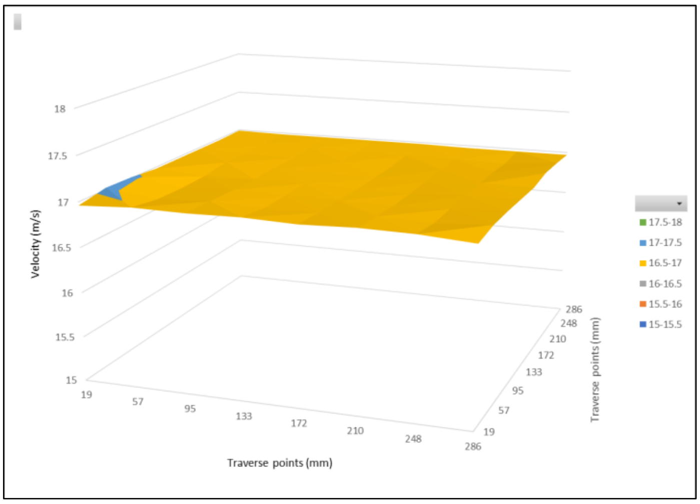

Figure 60: Velocity profile Plane 1 Ansys Fluent

9.1.3 Five-hole Probe – plane 1

A Five-hole pitot tube was used for traverse measurements of plane 1. Figure 61 illustrates the velocity profile obtained from the traverse measurements using the Five-hole Probe. The mass flow rate was kept constant throughout the experiment and monitored by means of a fixed Pitot Static Probe. The velocities measured by the Five-hole probe ranged from a minimum velocity of 15.14 m/s to a maximum velocity of 16.94 m/s with the mean velocity of 16.49 m/s and the mass flow rate of 1.5 kg/s.

One of the measured velocities from the data was found to be an outlier with a measurement of 15.14 m/s. This may have resulted from probe misalignment during the experiment. The maximum relative velocity difference factor is calculated to be 10.6%. A maximum relative velocity of 10.6% indicates a flat uniform velocity profile. By excluding the outlier velocity measurement, a better indication of the flat velocity profile was achieved.

When excluding the outlying velocity measurement point and focusing on the remaining 63 measured velocities, the minimum velocity becomes 16.17 m/s with the maximum velocity of 16.94 m/s. The mean becomes 16.51 m/s and the maximum relative velocity difference factor of is calculated to be 4.6% in plane 1, indicating a flat velocity profile.

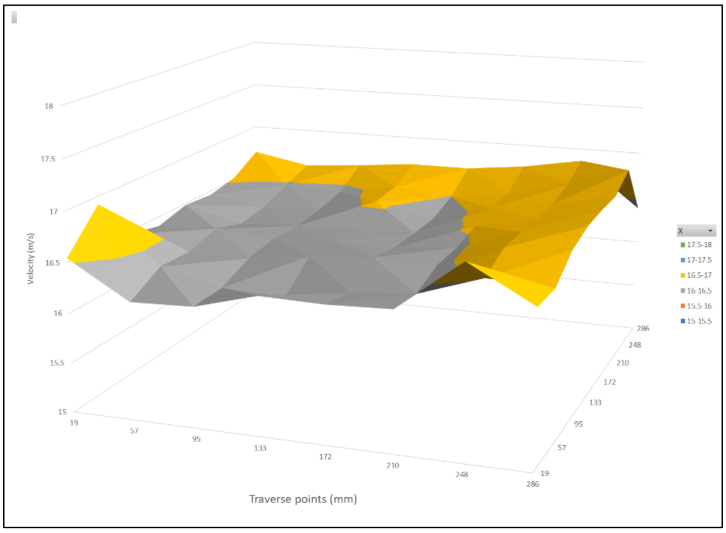

Figure 61: Velocity profile Plane 1 Five-hole probe

9.1.4 Omniprobe – Plane 1

Figure 62 illustrates the velocity profile of the flow field obtained from the traverse measurements results of an Omniprobe. The velocity ranged from a minimum velocity (v_{min}) of 15.04 m/s to a maximum velocity (v_{max}) of 18.19 m/s with the mean velocity calculated to be 17.33 m/s. The mass flow rate is estimated to be 1.63 kg/s. The maximum relative velocity difference factor is calculated to be 18.18%

The traverse measurements using the Omniprobe were on 60 days erlier than those measured using the Pitot-static tube and Five-hole probe. The fan settings were kept unchanged for all the measurements. However, some environmental factors such as temperature and atmospheric pressure had changed. The average temperature during this experiment was 19°C, whereas the experimental measurements using the Five-hole probe and the Pitot Static probe where conducted at an average tempeature of 28°C. These variables were recorded during the experiment.

The velocity profile was found to be flat except for the first points of each traverse where the velocity was measured slightly less, hence the tappering profile at traverse points of 19 mm. The drop in the velocity measured in close proximity to the wall could be a result of close proximity to the wall of the duct.

The probe manual indicates that a minimum distance of 4 times the diameter of the probe's sphere tip should be maintained to avoid wall proximity error [11]. The Omniprobe's sphere tip has a diameter of 8.5 mm and the recommended clearance to the wall is 34 mm, the 1st traverse points are at 19 mm.

When excluding the 1st traverse points from the analysis, the minimum velocity (v_{min}) becomes 16.93 m/s and the maximum velocity (v_{max}) becomes 18.19 m/s and the mean velocity is calculated to 17.58 m/s. The maximum relative velocty difference improves to 7.2%, indicating a flat velocity profile.

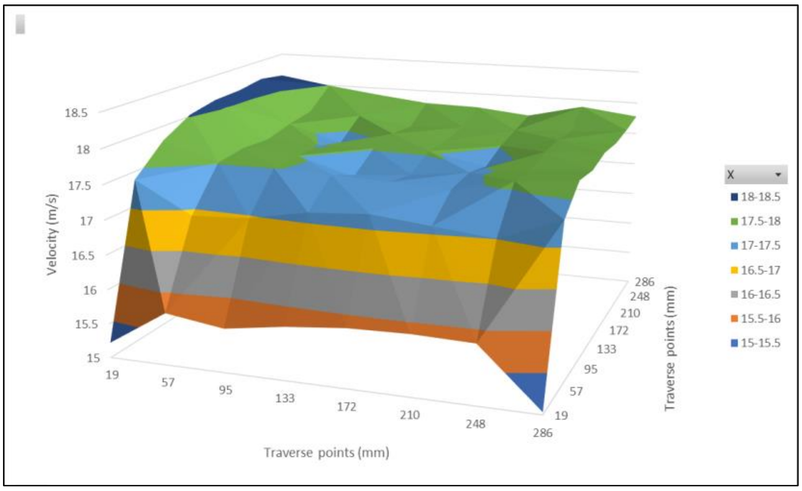

Figure 62: Velocity profile of plane 1 using Omniprobe

9.1.5 Discussion – Plane 1

Table 6 lists the results for an analytical comparison of the mass flow rates and the velocity profiles. The maximum relative velocity difference factor indicates the distribution of the velocity's uniformity across the plane. ANSYS Fluent yield a uniform velocity profile followed by the Pitot Static Probe, Five-hole probe and lastly the Omniprobe. As stated above, wall proximity affects the accuracy of the measurements of the probe. A minimum clearance of 34 mm to a wall is recommended by the probe supplier [11].

The comparison of the calculated mass flow rates from the traverse measurements indicates that the difference between ANSYS Fluent and Pitot Static Probe is 3.1%. The mass flow rates as measured and calculated from the Five-hole probe and the Pitot-static probe measurements, differ by 2.6%. The mass flow rate calculated from the measurements of the Omniprobe differ by 5.5% to those measured by the Pitot Static Tube.

From the experiment, the Omniprobe measured ±8% higher velocity in enclosed duct when compared to the Pitot Static Tube. The discrepancies require a thorough investigation.

Table 6: Plane 1 – Mass flow rates

	Mean velocity (m/s)	**Mass flow rate (kg/s)**	**Percentage difference**	**Maximum relative velocity difference**
Pitot Static Tube	16.92	1.54	Reference	2.9%
Ansys Fluent	16.96	1.59	3.1%	0.53%
Five-hole probe	16.5	1.5	2.6%	4.6%
Omniprobe	17.3	1.63	5.5%	7.2%

9.2 Plane 2 - Results

Plane 2 is 600 mm downstream of plane 1 and 200 mm from the 90º bend. The velocity profile at plane 2 is expected to be skewed due to proximity to the 90º bend.

Figure 63 illustrates the velocity vectors across plane 2, the yellow asterisks indicate the traverse points on plane 2. Due to the sudden 90º turn, the flow tends to rush to the bottom wall of the duct due to flow separation and recirculation of flow as in Figure 63.

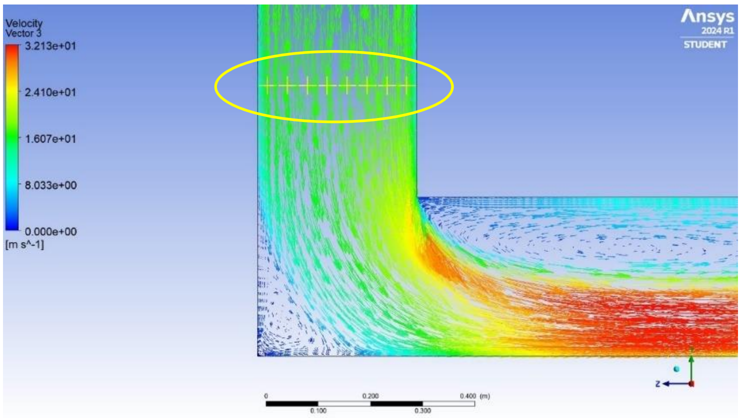

Figure 63: Velocity vectors across plane 2

9.2.1 Pitot-static probe Traverse results – Plane 2

Figure 64 illustrates the velocity profile resulting from the traverse measurements on plane 2 using a Pitot-static tube. The measured velocities by the Pitot-static tube ranged between a minimum velocity (v_{min}) of 13.85 to a maximum velocity (v_{max}) of 18.17 m/s and the mean velocity calculated as 16.96 m/s, the mass flow rate was calculated to be 1.54 kg/s.

The maximum relative velocty difference is calculated as 25.5%. This indicates that the velocity profile is not flat. The proximity to the 90^{o} turn distorts the velocity profile at plane 2. As the air particles separate from the boundary, the air speed on the wall where separation occurs increases due to adverse pressure gradient whereas on the adjacent wall the air speed is maintained. This results in a skewed profile as dipicted in Figure 64.

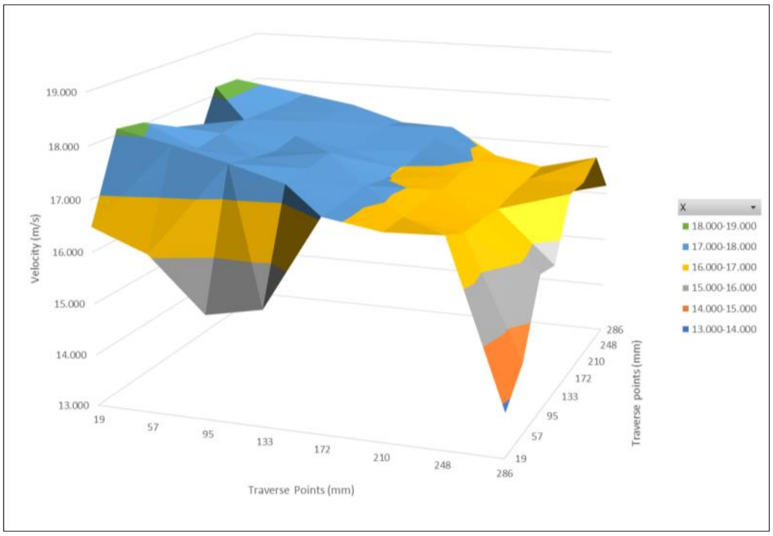

Figure 64: Velocity profile at plane 2 using Pitot Static Tube

The velocities measured at the corners of the duct were less than the rest of velocity measurements points in plane 2. This is due to the boundary layer effect of the 2 walls meeting at 90º.

9.2.2 CFD analysis – Plane 2

Figure 65 illustrates the velocity profile derived from ANYS Fluent simulation results. The velocity derived from the model on this plane ranged from a minimum velocity (v_{min}) of 15.84 to a maximum velocity (v_{max}) of 17.87 m/s The average velocity was found to be 17.15 m/s and the mass flow rate was found to be 1.54 kg/s. The maximum relative velocty difference is calculated as 11.8%. This indicates that the velocity profile is not uniform across the cross sectional area or plane 2. A pattern of fluid acceleration is noted on the wall where the fluid separates from the boundary due to the 90º bend.

Similar to the Pitot Static Probe results, the velocities measured at the corners of the duct measured less than the rest of velocity measurements points in plane 2. This is due to the boundary layer effect of the 2 walls meeting at 90º.

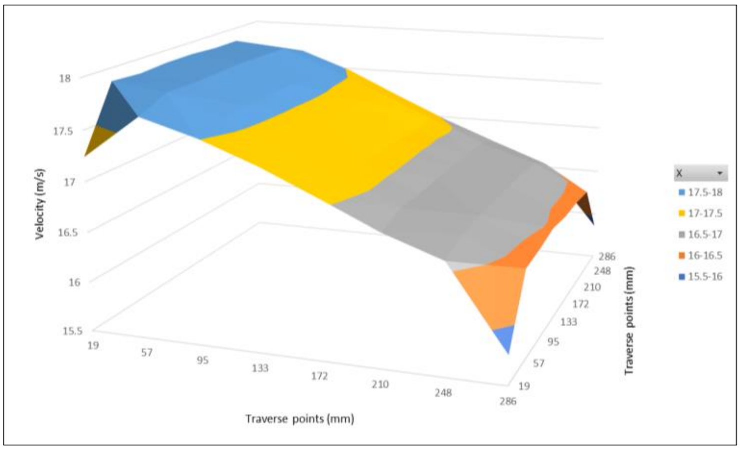

Figure 65: Velocity profile plane 2 – Ansys Fluent

9.2.3 Five-hole Probe – plane 2

Figure 66 illustrates the velocity profile derived from the traverse measurement results of plane 2 using the Five-hole probe. The measured velocity ranged from a minimum (v_{min}) of 15.5 m/s to a maximum (v_{max}) of 18.29 m/s; the mean velocity is 17.20 m/s. The maximum relative velocity difference is calculated to be 16.22%. Using the equal area method, the mass flow rate works out to be 1.54 kg/s.

The velocity profile generated from the Five-hole Probe compares well with the those generated from CFD (ANSYS Fluent) and Pitot Static probe in terms of the fluid velocity range, shape of the profile and the mass-flow. The traverse velocity measurements at the corners of the plane measured lower than the rest of the velocity measurements across the rest of the plane as expected. The traverse point at (210,19) distorts the velocity profiles unexpectedly; this can be a result of a measurement error.

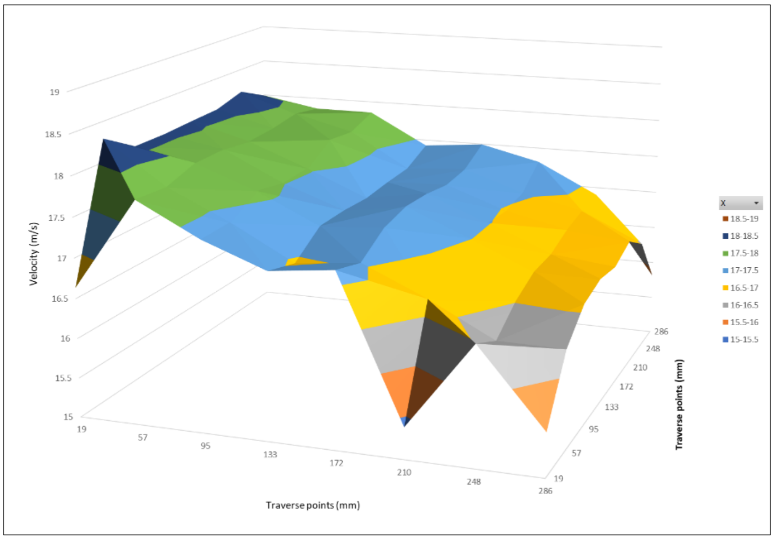

Figure 66: Velocity profile Plane 1 - Five-hole probe

9.2.4 Omniprobe – Plane 2

Figure 67 illustrates the velocity profile of the flow field at plane 2 generated from the results of the omniprobe traverse measurements. The velocity ranged from minimum velocity of 13 m/s to a maximum velocity of 19.95 m/s with the mean velocity calculated as 17.27 m/s.

The maximum relative velocity difference is calculated to be 40%. The mass flow rate calculated from the results of the omniprobe is 1.59 kg/s using equal area method.

The velocity profile illustrates the effect of wall proximity. At the 1st points in a traverse (i.e., at 19 mm) the velocity measurements are lower than the rest of the measurements across the rest of the plane. This can be attributed to the effect of proximity to the wall. A similar pattern is highlighted in plane 1.

The velocity profile indicates the skewness resulting form the 90^{o} bend, similar to the velocity profiles generated from ANSYS Fluent simulation, Pitot Static measurements, and Five-hole prbe.

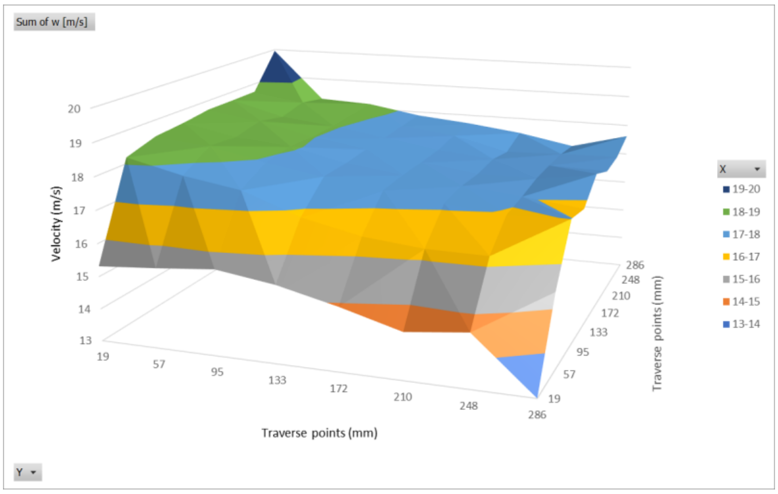

Figure 67: Velocity profile of plane 2 - Omniprobe

9.2.5 Discussion – Plane 2

Table 7Table 7 lists the resulting mass flow rates calculated from the results of the traverse measurements of the Pitot Static Probe, Five-hole Probe and Omniprobe. The mass flow rate calculated from the CFD simulation; the points of interest are like physical traverse points. The traverse points are inserted in the model and the probe function yields the required magnitude of the variable.

The mass flow rates compare well with mass flow rate calculated in plane 1 which serves as a reference plane for the experiment, using the Pitot Static Probe.

The mass flow rate as calculated from the Pitot Static Probe traverse measurements at plane 2 matches the mass flow rate calculated in plane1. This highlights the accuracy and reliability of the Pitot Static Probe.

From the results above, the velocity profile from at plane 2 is distorted by the effects of the 90º bend proximity. This effect is indicated by the notable from the calculated maximum relative velocity difference. Due to boundary separation at the bend, the velocity of the fluid along the wall where separation occurs accelerates and decelerates on the opposite wall.

The velocity profile of the Omniprobe illustrates the proximity of wall effect at 1st traverse points as this row of points is 19 mm from the wall of the duct; a minimum obstruction clearance of 34 mm is recommended for the Omniprobe [11].

Table 7: Plane 2 – Mass flow rates

	Average velocity (m/s)	Mass flow rate (kg/s)	Percentage difference	Maximum relative velocity difference
Pitot Static Tube	16.92	1.54	0%	25.5%
Ansys Fluent	17.15	1.54	0%	11.8%
Five-hole probe	17.2	1.54	0%	16.22%
Omniprobe	17.24	1.59	3.1%	40%

9.3 Plane 3 - Results

Plane 3 is 218 mm after the 90º bend; from the CFD simulation, the is a zone of recirculation. The five-hole probe and the Pitot-static tube are not applicable in this region due to highly distorted flow profile. Figure 68 illustrates the velocity vectors across the 90º bend. The regions of high speed are indicated by dense velocity vectors and the recirculation zone.

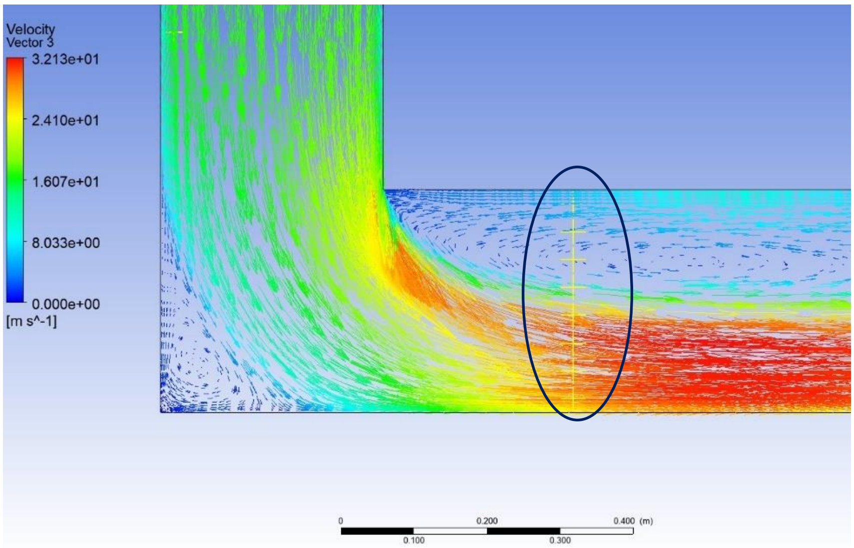

Figure 68: Velocity vectors across the 90⁰ bend

9.3.1 CFD - Plane 3

From the Ansys Fluent simulation, the velocity ranges from a minimum velocity of -5.76 m/s to a maximum velocity of 30.45 m/s with a mean velocity of 16.72 m/s. The minus indicates reverse flow in plane 3. The mass flow rate was calculated as 1.57 kg/s from the results of the traverse velocity measurements from CFD simulation.

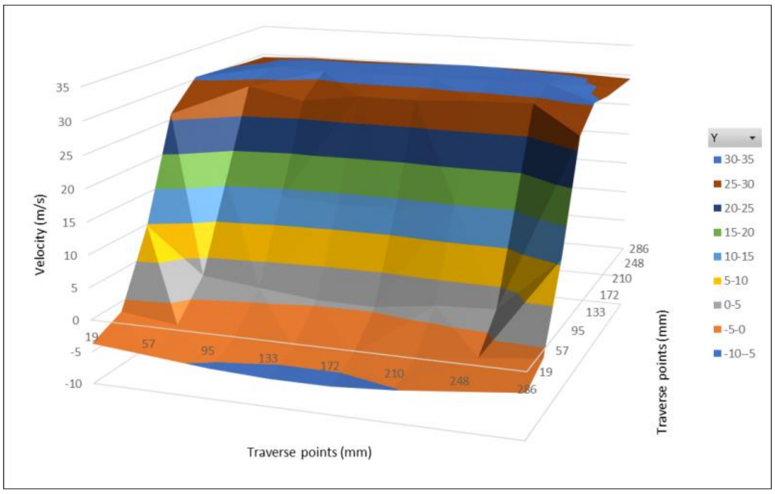

Figure 69: Velocity profile at plane 3 - Ansys fluent

9.3.2 Omniprobe – Plane 3

Figure 70Figure 70 illustrates the velocity profile generated from the traverse measurements of the Omniprobe on plane 3. The velocity was found to range from a minimum velocity of -7.6 m/s to a maximum velocity of 29.38 m/s with a mean velocity of 16.15 m/s. The mass flow rate calculated from the results of the measurements of the Omniprobe is 1.5 kg/s.

Reverse flow was measured by the Omniprobe on plane 3 in the region of reverse flow shown in Figure 68, indicating the capability of the Omniprobe to measure reverse flow in complex flow fields. The effect of wall proximity cannot be identified on this plane due to the complex velocity profile.

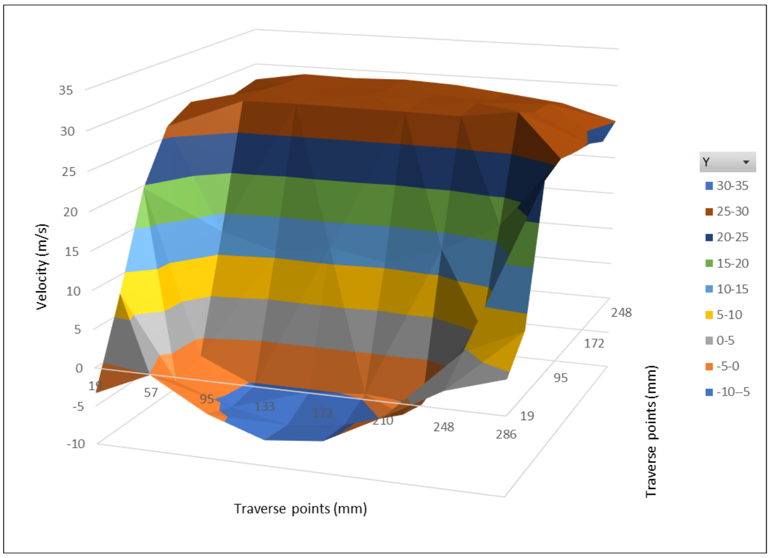

Figure 70: Velocity profile at plane 3 – Omniprobe

9.3.1 Discussion – Plane 3

The Pitot-static probe and the Five-hole probe are not applicable at plane 3 and 4 due to the complex nature of the flow being multi-directional at these 2 planes.

The Omniprobe was tested at these planes for its capability to measure reverse flow and its capability confirmed. The velocity profile extracted from ANSYS Fluent simulation is comparable with the actual experimental traverse measurements at plane 3.

Table 8 lists the calculated mass flow rates from CFD simulation and actual experimental measurements using the Omniprobe. These were compared to the mass flow rate derived using the Pitot-static tube in plane 1 and were found to be comparable to within the acceptable variance limit.

Table 8: Plane 3 – Mass flows rates

	Average velocity (m/s)	Mass flow rate (kg/s)	Percentage difference
Ansys Fluent	16.72	1.57	1.9%
Omniprobe	16.16	1.5	3.6%

9.4 Plane 4

Plane 4 is 182 mm from plane 3 and 445 mm from the 90º bend (Figure 71). This plane also falls in the complex flow field zone where the velocity profile is highly distorted and multi-directional.

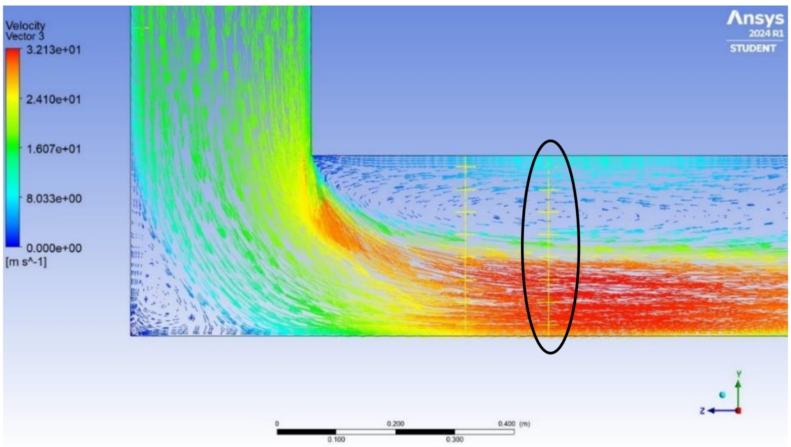

Figure 71: Velocity vectors across Plane 4 encircled

9.4.1 ANSYS Fluent - Plane 4

Figure 72 illustrates the velocity profile modelled using the results from ANSYS Fluent CFD model. Across plane 4 in the CFD model, the velocity was ranged from a minimum velocity of 8.14 m/s to a maximum velocity of 31.97 m/s. The mean velocity was calculated as 16.93 m/s and the mass flow rate across the plane, using the equal area method, was 1.59 kg/s.

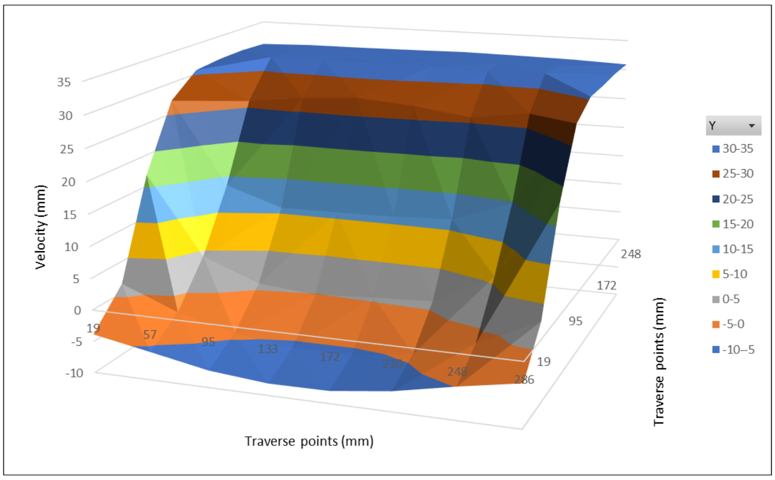

Figure 72: Velocity profile at plane 4 - ANSYS fluent

9.4.2 Omniprobe – Plane 4

Figure 73 illustrates the velocity profile derived from the Omniprobe traverse measurements at plane 4. The velocity ranges from -6.9m/s to 31.51 m/s with the mean velocity of 16.77 m/s and the mass flow rate approximated at 1.55 kg/s across plane 4.

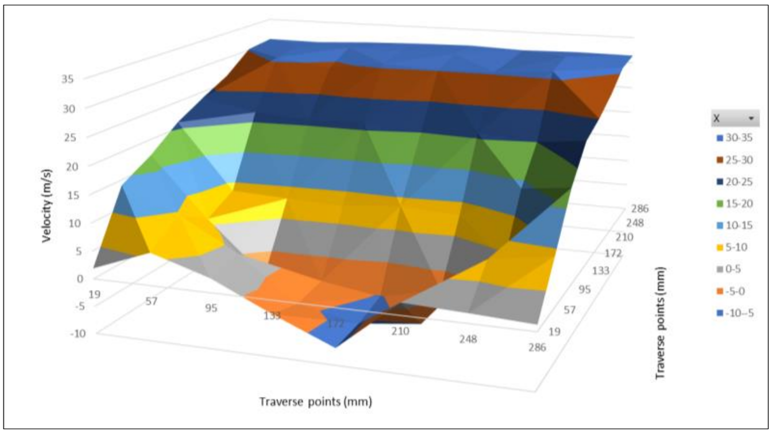

Figure 73: Velocity profile at plane 4 – omniprobe

Like plane 3, the Omniprobe measured reverse flow in plane 4 and the velocity profile illustrates that the flow is recovering.

9.4.3 Discussion – Plane 4

From the results of the traverse using the Omniprobe, the flow is recovering from the 90° bend flow disturbance when compared to plane 3. This was established by comparing the sum of velocity components in reverse flow in plane 3 with similar velocity vectors in reverse flow in plane 4.

Table 9 lists the calculated mass flow rates from CFD simulation and actual experimental measurements using the Omniprobe. These were compared to the mass flow rate derived using the Pitot Static Probe in plane 1 and were found to be comparable to within the acceptable variance limit of 5% for this study.

Table 9: Plane 4 - Mass flow rates

	Average velocity (m/s)	**Mass flow rate (kg/s)**	**Percentage difference**
Ansys Fluent	16.93	1.59	3.1%
Omniprobe	16.76	1.54	0%

9.5 Plane 5

From the CFD model as illustrated in Figure 74, across plane 5 the flow is recovering from the flow disturbance with no reverse flow. The Pitot Static Probe and the Five-hole probe were applied in this plane for traverse measurements.

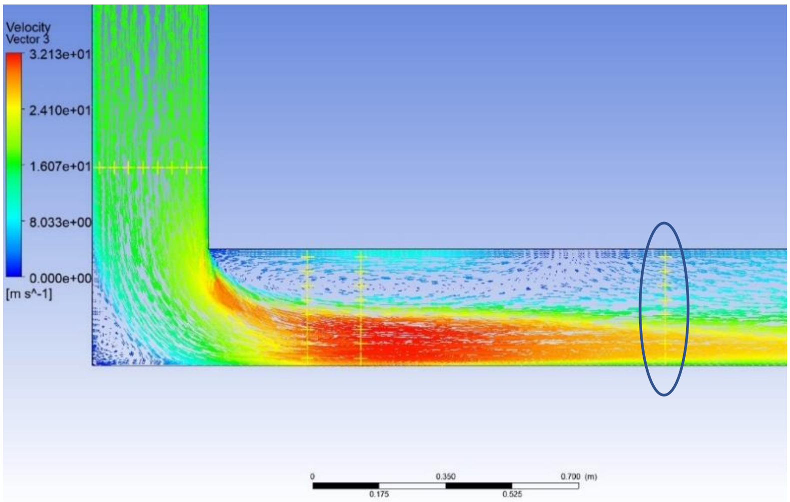

Figure 74: Velocity vectors across plane 5

9.5.1 Pitot Static Probe – Plane 5

Figure 75 illustrates the velocity profile generated from the traverse measurements of plane 5 using a Pitot Static tube. The velocities as measured by the Pitot Static Probe ranged between a minimum velocity $v_{min)}$ of 7.5 m/s to a maximum velocity ($v_{max)}$ of 24.51 m/s with the mean velocity (v_{mean}) was calculated to be 17.12 m/s, and the mass flow rate was calculated to be 1.56 kg/s.

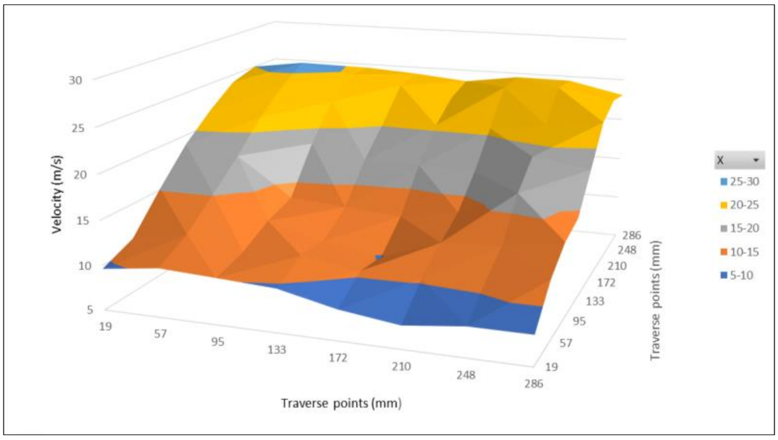

Figure 75: Velocity profile at plane 5 - Pitot static tube

9.5.2 CFD – Plane 5

Figure 76 illustrates the velocity profile of plane 5 generated from ANYS Fluent traverse. The velocity ranged from a minimum velocity of 4.55m/s to a maximum velocity of 27.5 m/s. The average velocity was found to be 17.08 m/s and the mass flow rate was approximated to be 1.61 kg/s. From the simulation results as illustrated by the velocity profile, at plane 5 of the duct, the flow is still recovering with no reverse flow. The flow is still highly distorted in this region.

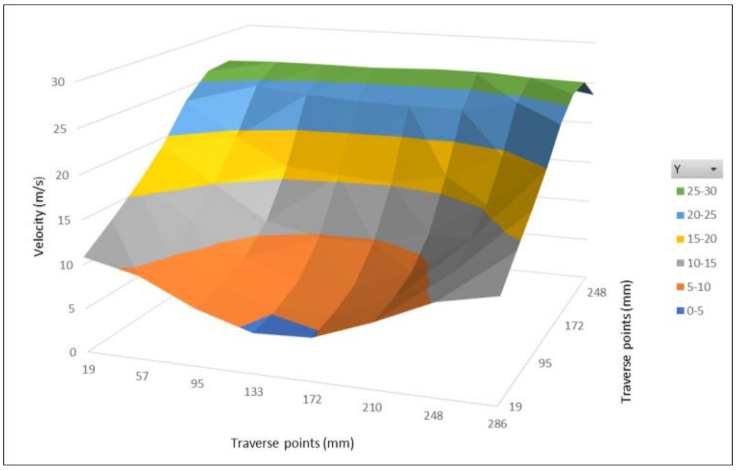

Figure 76: Velocity profile plane 5 – Ansys Fluent

9.5.3 Five-hole Probe – Plane 5

Figure 77 illustrates the velocity profile generated from the traverse measurements using a Five-hole probe. The velocity ranged from a minimum velocity of 0.2 to a maximum velocity of 26 m/s with the mean velocity of 25.20 m/s. The mass flow rate was estimated to be 1.34 kg/s. The velocity profile indicates that the flow is still highly distorted at plane 5 with x2 traverse measurements of 0 m/s. The traverse was repeated, and similar measurements resulted.

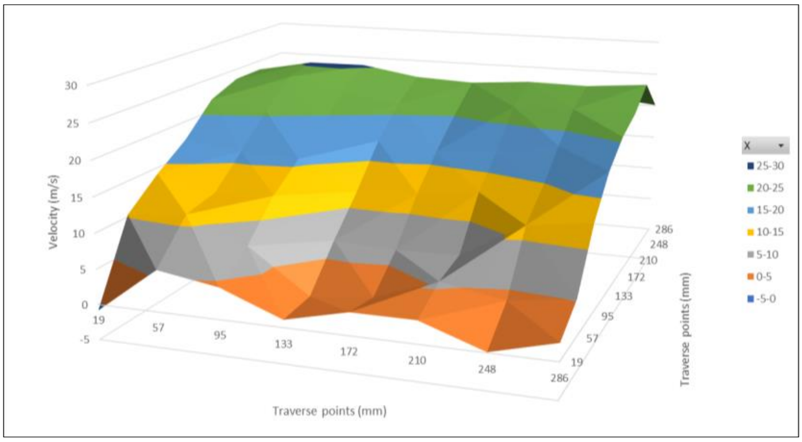

Figure 77: Velocity profile at plane 5 - Five-hole probe

9.5.4 Omniprobe – Plane 5

Figure 78 illustrates the velocity profile of the flow field modelled from the results of an omniprobe at plane 5. The velocity ranged from 7.89 m/s to 24.27 m/s with the average being 16.96 m/s. The mass flow rate is estimated to be 1.57 kg/s through equal area method. At this plane the effect of wall proximity is not clear. The velocity profile suggests a distorted flow field recovering from a flow disturbance. The omniprobe traverse measurements at this plane suggest that there is no reverse flow in the measurement plane 5.

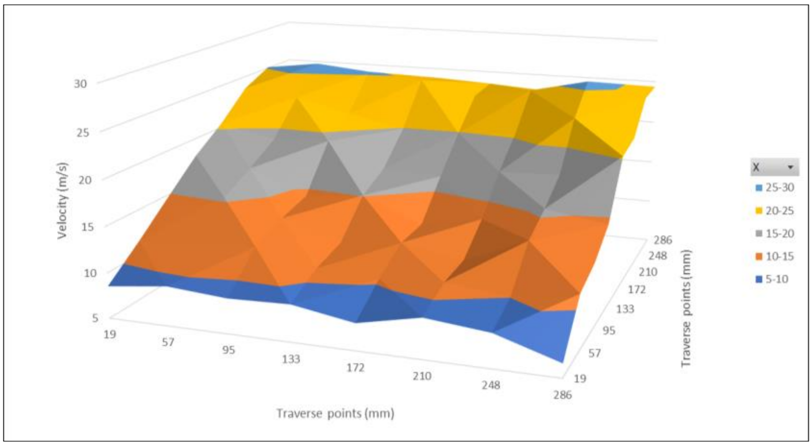

Figure 78: Velocity profile of plane 5 - omniprobe

9.5.5 Discussion – plane 5

From the CFD and experimentally derived flow velocity profiles, the flow at plane 5 is highly distorted. The traverse measurements conducted on this plane by the omniprobe suggests that there is no reverse flow.

Table 10 lists the calculated mass flow rates across the plane 5 and are within the acceptable variance limit of 5% for this study, except for the Five-hole probe with a 13% difference to the mass flow rate as measured by the reference probe. This can be attributed to the highly distorted flow profile in Plane 5 which may be out of the measuring range of a Five-hole probe calibration; the Yaw and Pitch range of -30º to 30º.

Table 10: Plane 5 - Mass flow rates

	Average velocity (m/s)	Mass flow rate (kg/s)	Percentage difference
Pitot Static Tube	17.15	1.56	1.3%
Ansys Fluent	17.08	1.61	4.3%
Five-hole probe	14.96	1.34	13%
Omniprobe	16.96	1.57	1.91%

9.6 Plane 6

Plane 6 is 1200 mm from the 90⁰ bend and 400 mm from the air duct exit. The flow is still recovering from the flow disturbance and one directional according to CFD. Figure 79 shows that the flow is still highly distorted and recovering with duct length. Similarly, in industry it is not practical to have a duct length that is long enough to allow for full development of the velocity profile.

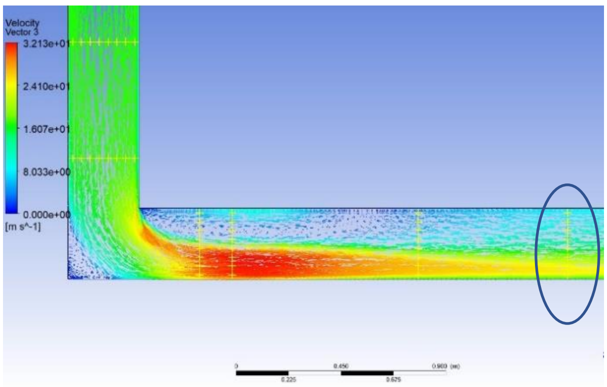

Figure 79: Velocity vector distribution across plane 6

The aim of this experiment is to establish the effectiveness of the Omniprobe, Five-hole probe in flow conditions where the velocity profile is distorted.

9.6.1 Pitot Static Probe – Plane 6

The Pitot Static probe traverse measurements in plane 6 range from a minimum velocity of 10.25 m/s to a maximum velocity of 21.41 m/s and averaging at 17.18 m/s. The mass flow rate is estimated to be 1.56 kg/s. The results indicate that the velocity is recovering from the 90° bend flow disturbance as can be seen in Figure 80.

The mass flow rate calculated with the results from the Pitot Static probe remain consistently within the 5% variance limit for the study and supports the use of a Pitot Static probe as a reference probe for the current study.

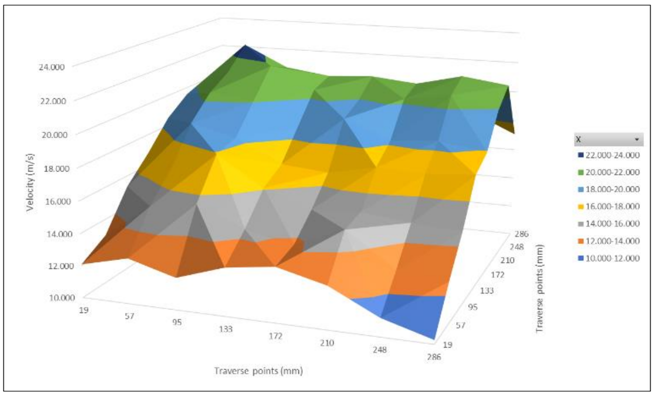

Figure 80: Velocity profile at plane 6 - Pitot Static Tube

9.6.2 Omniprobe – Plane 6

Figure 81 illustrates the velocity profile generated from the traverse velocity measurements of plane 6 in CFD. The velocity ranged from 8.43 m/s to 24.87 m/s. The mean velocity across the plane is 17.03 m/s. The mass flow rate is estimated to be 1.6 kg/s.

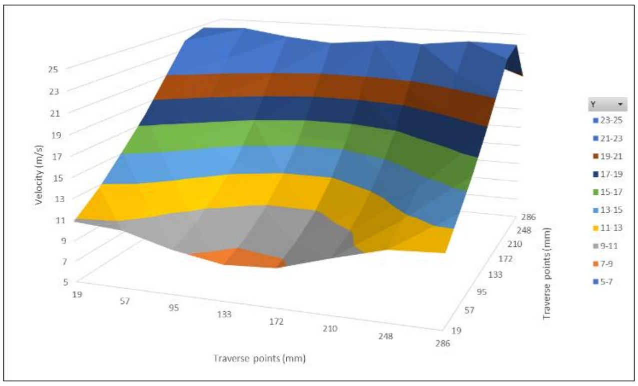

Figure 81: Velocity profile at plane 6 - Ansys fluent

Figure 81 shows that the velocity profile is recovering and requires extra length of duct for full recovery.

9.6.3 Five-hole Probe – Plane 6

Figure 82 shows the velocity profile generated from the traverse measurements of a Five-hole probe. The velocity ranged from a minimum velocity of 2.03 to a maximum velocity of 21.79 m/s. The mean velocity across the plane is 15.2 m/s and mass flow rate of 1.36 kg/s.

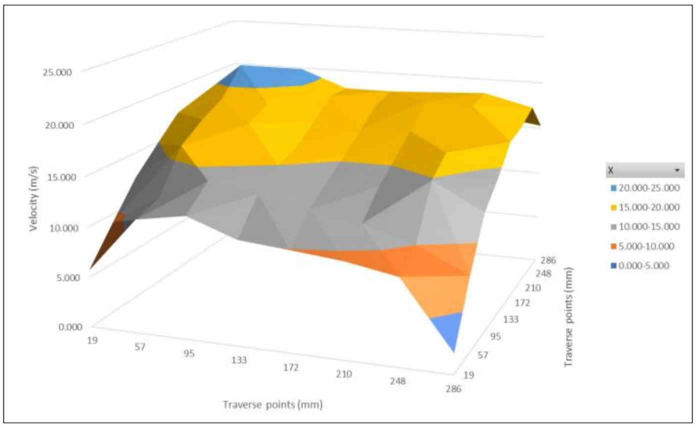

Figure 82: Velocity profile at plane 6 – Five-hole probe

9.6.4 Omniprobe – Plane 6

Figure 83 illustrates the velocity profile at plane 6, derived from the traverse measurements of the Omniprobe. The velocity was found to range from a minimum velocity of 9.04 m/s to a maximum velocity of 21.97 m/s. The average velocity was calculated as 17 m/s; the mass flow was estimated to be 1.57 kg/s.

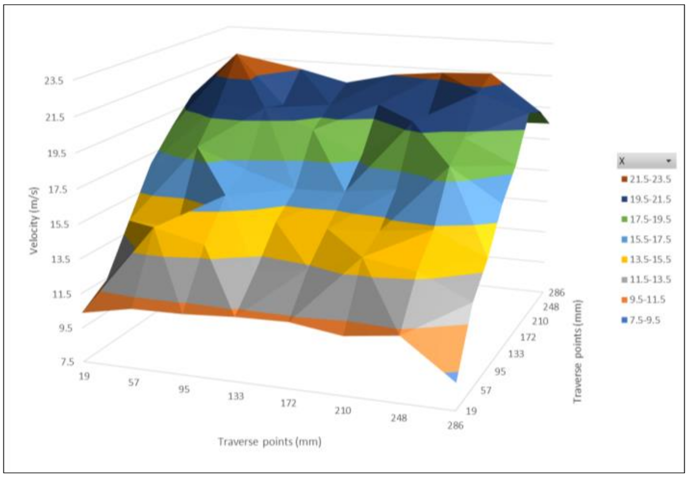

Figure 83: Velocity profile at plane 6 – Omniprobe

9.6.5 Discussion – Plane 6

When comparing the velocity profiles of the CFD with the velocity profiles derived from experimental results, the velocity profile from CFD is recovering slowly than the experimental velocity profile. The mass flow rate calculated from the traverse measurements using a Five-hole probe across plane 6 exceeds the 5% when compared with the mass flow rate derived from Pitot Static Probe measurements in plane 1. From the results, this is due to flow angles exceeding the Yaw and Pitch range of +/-30º.

Table 11: Plane 6 - Mass flow rates

	Average velocity (m/s)	**Mass flow rate (kg/s)**	**Percentage difference**
Pitot Static Tube	17.00	1.5	1.9%
Ansys Fluent	17.02	1.60	3.75%
Five-hole probe	15.2	1.36	11.7%
Omniprobe	17.00	1.57	1.9%

10. CONCLUSION

The objective of the research study was to investigate the velocity flow profiles and mass flow rates of air flow through square wind tunnel (duct) using equal area method. The aim was to establish the accuracy and reliability of measuring instruments in complicated flow patterns.

As part of the study, a five-hole probe was calibrated for use in measuring and reproducing flow profiles in square ducts. The Pitot Static tube and an orifice were used for the calibration of the Five-hole probe and for verification of the Omniprobe. An Omniprobe with fourteen holes capable of measuring reverse flow and flow angles was acquired and verified for use in complex flows. A duct prototype was developed for the study and 6 planes of interest were identified for the recreation of the velocity profiles. Planes 1 and 2 are located before a 90º bend, these are reference planes.

The experimental study found the estimation of the mass flow rate from the traverse of a Pitot Static Tube to be uniform throughout the air duct. The mass flow rates across the various planes were compared with the mass flow rate derived from the measurements of the Pitot Static Probe in plane 1. The Pitot Static Tube could not be used in planes 3 and 4 as these planes fall in the region where there is flow recirculation. With plane 1 being the reference plane, the mass flow rates at plane 2, 5, and 6 differs from plane 1 by at most 1.9%. Thus, the measurements of the Pitot Static Tube can be reliable in terms of accuracy and for the estimation of the mass flow rate through the duct. The resulting mass flow rate also compares well with the mass flow rate as derived from Ansys Fluent flow simulation with the variance being 4.3% at most.

The velocity profiles generated from the Omniprobe traverse at planes 1 and 2 show lower velocity for the 1st and 2nd traverse points. This can be attributed to proximity to the wall as the probe itself deflects the flow. It is for this reason that the collapse of flow is observed in the velocity profile.

To avoid this effect, the supplier has recommended a clearance of at least 4 times the head diameter, that is 4*8.5 = 34 mm from any other geometry. For this study, the first traverse point was 19.06 mm from the wall and the second 57.19 mm from the wall.

It was noted during the experiment that the velocity measured by the Omniprobe at the centre of the duct at plane was higher when compared to the measurement using the Pitot-static tube with the variance ranging from 8% to 12%. It is for this reason that the flow collapse is not reflected in the mass flow rate. In the open stream wind tunnel, the mass flow rate variance as measured by the orifice, Pitot-static tube and Omniprobe was found not to be more than 5%. In a closed conduit, the variance between the Omniprobe and the pitot static tube rises to at least 8%. The equal area method using the Omniprobe are not reliable.

For this study, the Five-hole probe was calibrated in the open stream wind tunnel for Yaw and Pitch range of -30º to 30º. From the verification results, the Five-hole varied at most by 4% when compared to the Pitot-static tube. The angularity for the range was found to be within 2% accurate when compared to numerical calculations.

The application of the Five-hole probe at planes 1 and 2 compares well with the Pitot-static tube with the mass flow variance 2.6%. The probe was not applicable to plane 3 and 4 due to the recirculation zone. At planes 5 and 6, the mass flow rate derived from the Five-hole probe dropped 13% with the reference flow rate at plane 1.

From the results of this study, the 14-hole Omniprobe did not yield accurate results when compared with the Pitot-static tube. The Five-hole probe was found to be accurate in the zone where the flow is evenly distributed. However, the variance when compared with the reference increased when the Five-hole was applied in zones after a flow disturbance.

The Pitot-static tube yielded accurate flow rates when compared to the numerical simulation and remains the preferred instrument for mass flow rate measurements is square ducts.

11. FUTURE WORK

Future work related to this study for further investigation:

- 14-hole Omniprobe application in large industrial ducts.
- Detailed CFD modelling of industrial ducts.
- Effects of measuring flow field using the Omniprobe in proximity to an obstruction.
- Market search for advanced measuring technologies in highly distorted flow fields.

REFERENCES

[1] W. Pierce, M. Le Roux, Statistics of utility-scale power generation in South Africa, February 2023, accessed July 2023

[2] Generation Division, Plant Mix, https://www.eskom.co.za/wp-content/uploads/2022/03/GX-0001-Generation-Plant-Mix-Rev-25.docx.pdf. December 2021 accessed July 2023.

[3] Generation Communication. August 2021. How Electricity is Produced at a coal-fired power station. CO 0002 Revision 13: 1-5.

[4] Thermodyne, https://www.thermodyneboilers.com/components-working-thermal-power-plant/ Last accessed 25 Sptember 2024

[5] Nasa Glenn Research Center, The Process of Combustion, https://www.grc.nasa.gov/www/k-12/airplane/combst1.html, Last accessed on 23 October 2023

[6] Products of combustion, Penn State College of Earth and Mineral Sciences, https://www.e-education.psu.edu/egee102/node/1951, Last accessed July 2023

[7] E Tawil, P.E., Leed AP. Boiler Basics, Operation and Maintenance. Course no.: M08-009

[8] E. Rieschel, A study of viscous fluids is a square duct, 13 July 2016

[9] Eskom. Fossil Fuel Firing Regulation FFFR, 240-105453648. December 2021

[10] International Standard, ISO 3966, Measurement of fluid in closed conduits – Velocity area method using Pitot-static tubes, 2nd edition, 2008-07-15

[11] K. Rayaprolu, Boilers A Practical Reference, Version date 20121026

[12] Eskom: Arnot Power Station. https://www.eskom.co.za/heritage/history-in-decades/escom-1963-1972/arnot-power-station/. Accessed 10 September 2024

[13] ISO 10780, Stationery Source Emissions – Measurement of velocity and volume flowrate of gas streams in ducts. 1st Edition 1994-11-15

[14] V. Elliot, Introductory Applied Thermodynamics, 1998, 2-16.

[15] M. Shapiro. Principles of Engineering Thermodynamics, 8th, SI Version, 694-700, 2015

[16] ANSYS. Introduction to CFD methodology, Introduction to ANSYS Fluent, Lecture 2, Release 13, December 2010

[17] A. S. Murali, C. B. Suresh, Flow Measurement in Large Ducts and Pipes, August 28-30 2017.

[18] https://www.flowcontrolnetwork.com/instrumentation/flow-measurement/thermal/article/15561367/multipoint-thermal-vs-dp-flowmeters-for-combustion-air-flow-applications; Last date Accessed on the 5th March 2024

[19] P. Ostrowski, L. Remiorz. Measurement of gas flow in short ducts also rectangular, 2012

[20] F. M. White, Fluid Mechanics,7th Edition, 347-351, 2008

[21] S. K. Norfleet, Robert E. Barton, RMB Consulting & Research, Inc, Impact of wall effects on flue gas velocities in rectangular ducts and recommended revisions to EPA Reference method 2H

[22] Cengel A.Y. Cimbala J.M. Fluid Mechanics, Fundamentals and Applications. 3rd Edition Mc Graw Hill, 2014

[23] C. Zhou, Estimation of Volumetric Flow Rate in Square Duct: Equal Area Versus Log-Tchebycheff Methods, 2005

[24] R. W. Miller, Journal of Fluids Engineering, The Stolz and ASME-AGA Orifice Equations Compared to Laboratory Data, Vol 101, December 1979

[25] David M. Birch, Multi-hole Pressure Probes, Technical note TN -0616-2016, rev. 1.4b

[26] Vectoflow, https://vectoflow.de/en/produkt/omniprobe/ Last accessed 02 September 2024

[27] Vectoflow measurements in fluids, Vectovis Probe Manual, Version 2021-10-27

[28] Governing Equations of Fluid Dynamics, https://courses.ansys.com/index.php/courses/governing-equations-of-fluid-dynamics/, 28 Jul 2020, accessed December 2023

[29] Manchester CFD Team, https://www.manchestercfd.co.uk/post/all-there-is-to-know-about-different-mesh-types-in-cfd#:~:text=A%20mesh%20divides%20a%20geometry,which%20domain%20is%20broken%20up. Last accessed 02 September 202

[30] S.V.M. Tec. PSC8 PSC16 PSC24 Pressure scanner data sheet. Version date 09.10.2010

[31] L. M. Davkin. The aerodynamic effect of wheel fairing applied to a generic formula one car, May 2022

[32] Government Gazette, Act No 39 of 2004: National Environmental Management: Air Quality Act. 2004, 24 February 2005

APPENDICES

APPENDIX 1: Five-Hole Probe Calibration polynomials

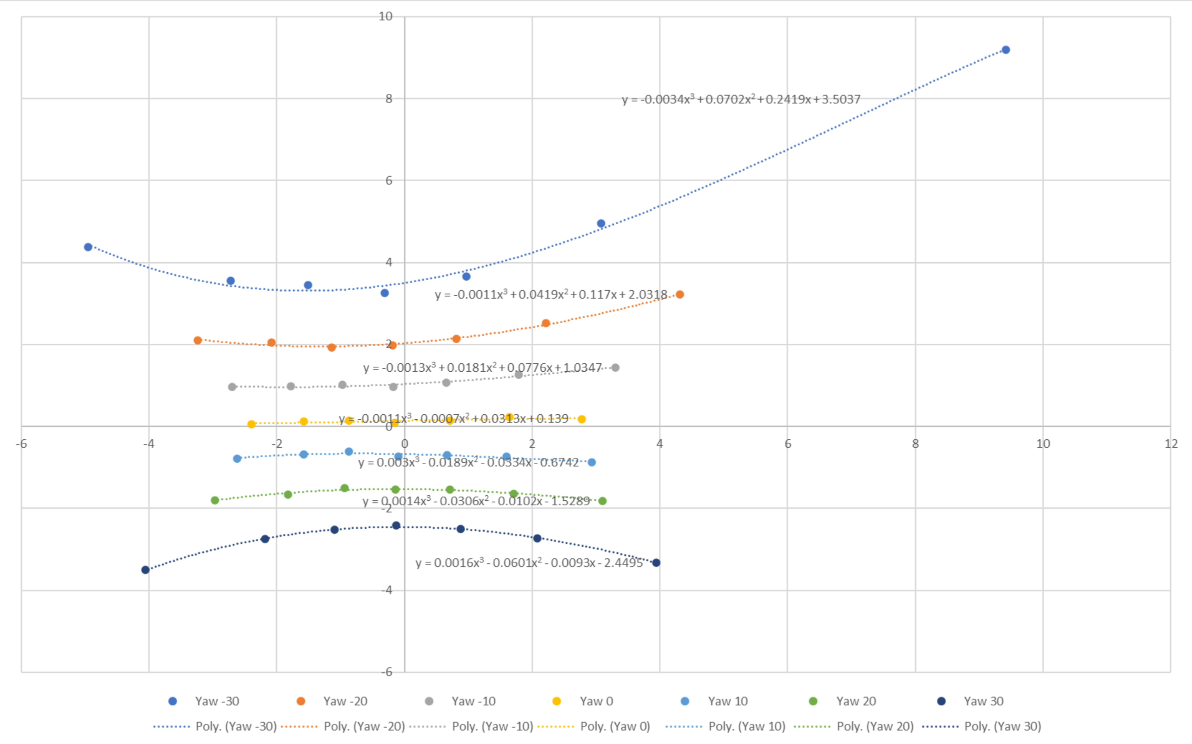

Figure 84: Pitch Coefficient

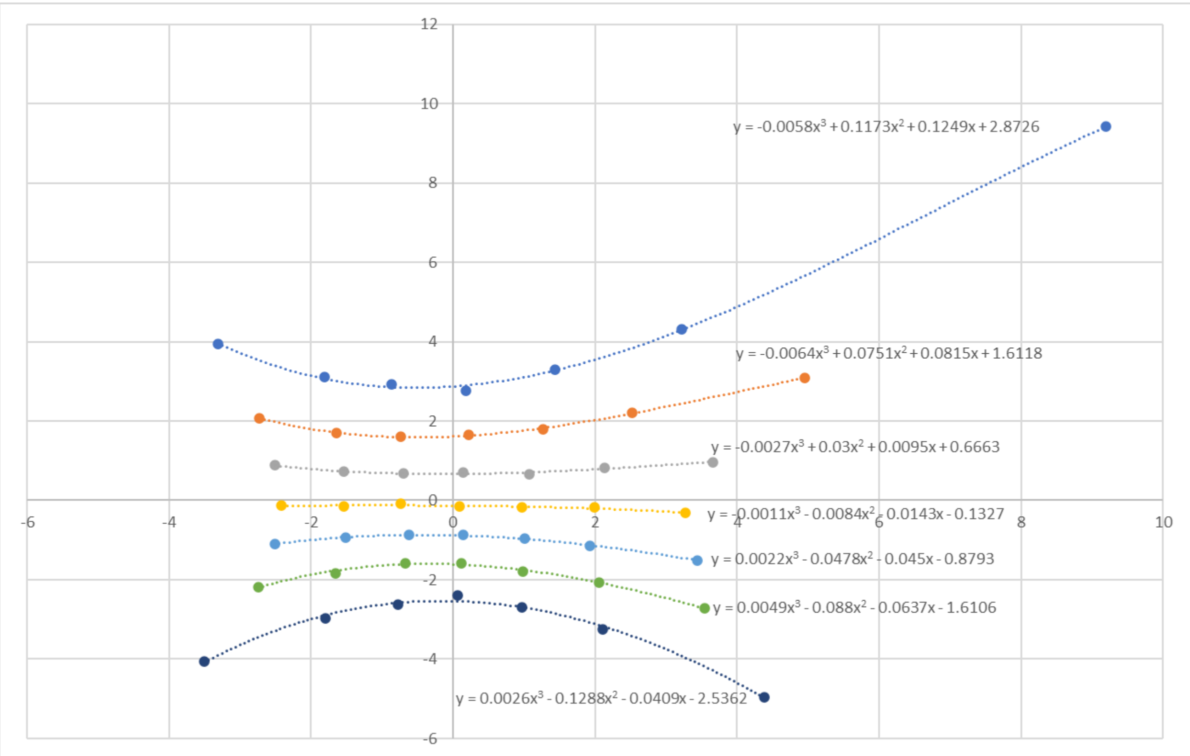

Figure 85: Yaw Coefficient

APPENDIX 2: Actual calibration wind tunnel

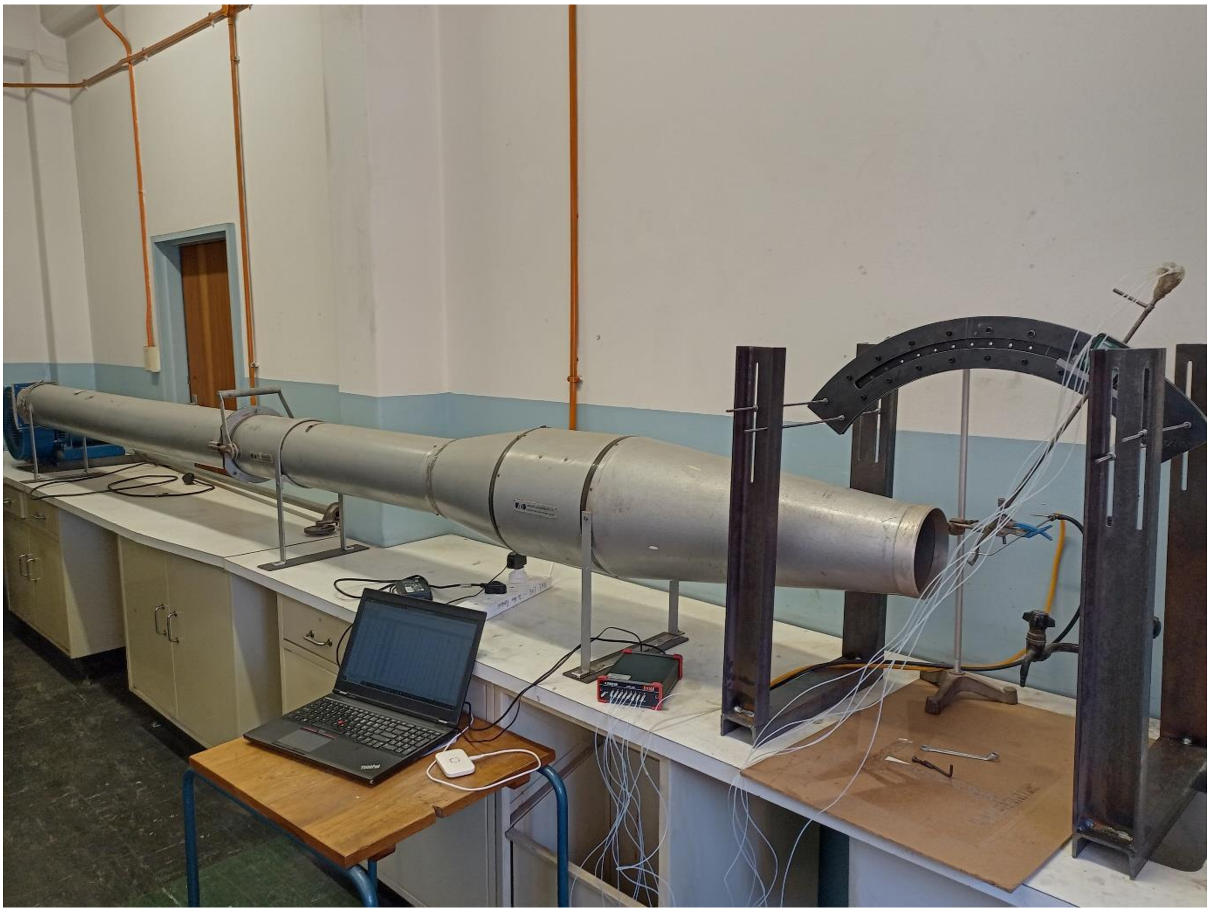

Figure 86: Free stream Calibration wind tunnel

APPENDIX 3: Sample calculation of Cp_{yaw}, Cp_{pitch}, Cpo, Cps, Yaw β, and Pitch α. Involves interpolation.

1	PITCH				1	YAW		
Y	Cy	3.6654	**ANGLE**		Y	Cp	-3.2079	**ANGLE**
X	Cp	-3.2079	**-28.665**		X	Cy	3.6654	**29.96663**
-30	Y1	3.870502			-30	Y1	5.166103	
-20	Y2	2.334464			-20	Y2	2.969432	
-10	Y3	1.033678			-10	Y3	1.4983	
0	Y4	-0.13696			0	Y4	0.190152	
10	Y5	-1.29947			10	Y5	-0.90282	
20	Y6	-2.4736			20	Y6	-1.90847	
30	Y7	-3.81627			30	Y7	-3.21227	

Cpo &Cps Polynomials			
	Aver Cpo		Aver Cps
	Pitch -30		Pitch -30
30	-2.08247	30	0.262578
20	-1.25431	20	0.454839
10	-1.07609	10	0.544667
0	-0.98215	0	0.574419
-10	-1.39163	-10	0.574181
-20	-2.30727	-20	0.480192
-30	-7.09358	-30	-0.0797
	Pitch -20		Pitch -20

	1	PITCH	-28.665				PITCH	-28.665
		YAW	29.96663				YAW	29.96663
		Cps	**-0.0398**				Cpo	**-2.86463**
-30	EQ1	0.080557117			-30	EQ1	-5.98883	
-20	EQ2	0.426072417			-20	EQ2	-2.32654	
-10	EQ3	0.424608258			-10	EQ3	0.634991	
0	EQ4	0.449918756			0	EQ4	-1.0203	
10	EQ5	0.519356871			10	EQ5	-0.84309	
20	EQ6	0.140552817			20	EQ6	-1.5353	
30	EQ7	-0.04040016			30	EQ7	-2.86908	

APPENDIX 4: Orifice calculation sample

Potentiometer	vp	qmc	dp	density	Viscosity	C	E	α	qm	vc	Rec	
70	10.04803	0.181781	235	0.990463	1.792E-05	0.616478	1.086307	0.669685	0.177316	14.58815	62991.58	
						0.622705	1.086307	0.676449	0.179107	14.7355	63627.85	
						0.622652	1.086307	0.676391	0.179092	14.73424	63622.38	
						0.622652	1.086307	0.676392	0.179092	14.73425	63622.43	
						0.622652	1.086307	0.676392	0.179092	14.73425	63622.43	
						0.622652	1.086307	0.676392	0.179092	14.73425	63622.43	
						0.622652	1.086307	0.676392	0.179092	14.73425	63622.43	
						0.622652	1.086307	0.676392	0.179092	14.73425	63622.43	
						0.622652	1.086307	0.676392	0.179092	14.73425	63622.43	
						0.622652	1.086307	0.676392	0.179092	14.73425	63622.43	-1.50153
Potentiometer	vp	qmc	dp	density	Viscosity	C	E	α	qm	vc	Rec	
60	12.30627	0.222635	363	0.990463	1.792E-05	0.616478	1.086307	0.669685	0.220378	18.13091	78289.2	
						0.621634	1.086307	0.675285	0.222221	18.28253	78943.9	
						0.621596	1.086307	0.675244	0.222207	18.28142	78939.12	
						0.621596	1.086307	0.675244	0.222207	18.28143	78939.15	
						0.621596	1.086307	0.675244	0.222207	18.28143	78939.15	
						0.621596	1.086307	0.675244	0.222207	18.28143	78939.15	
						0.621596	1.086307	0.675244	0.222207	18.28143	78939.15	
						0.621596	1.086307	0.675244	0.222207	18.28143	78939.15	
						0.621596	1.086307	0.675244	0.222207	18.28143	78939.15	
						0.621596	1.086307	0.675244	0.222207	18.28143	78939.15	-0.19268

APPENDIX 5: Sample verification calculation

Density (kg/m^3)	Atm kPa	R	T
0.990462964	83.73	287.05	294.5

Potentiometer Setting	P_{pitot} (Pa)	v_{pitot}(m/s)	Mass Flow rate - Pitot Static Tube (kg/s)	Mass Flow rate - Orifice (kg/s)	Mass Flow rate - Omniprobe (kg/s)	Discrepency between Orifice and Pitot Static Tube (%)	Discrepency between Orifice and Omniprobe (%)	Discrepency between Pitot Static Tube and Omniprobe (%)
0	50	10.04803	0.184	0.179	0.174	-2.479	-5.642	-5.340
10	75	12.30627	0.223	0.222	0.214	-0.193	-4.126	-3.963
20	109	14.83574	0.268	0.269	0.257	0.284	-4.467	-4.276
30	149	17.34559	0.314	0.315	0.301	0.533	-4.397	-4.211
40	192	19.69004	0.356	0.359	0.344	0.720	-3.702	-3.569
50	247	22.33286	0.404	0.405	0.389	0.184	-3.886	-3.741
60	307	24.89803	0.450	0.452	0.434	0.344	-3.786	-3.648
70	371	27.37051	0.495	0.499	0.474	0.720	-4.382	-4.198

APPENDIX 6: Pressure Scanner Data Sheet

SVMtec

PSC8 • PSC16 • PSC24 Pressure Scanner Datasheet

PSC8 • PSC16 • PSC24

Multichannel Pressure Scanner Simultaneous acquisition of 4 or 5 pressure signals

- Measuring ranges selectable from 125 Pa to 15 kPa (0.25 to 150 mbar) uni- and bi-directional, higher range on request
- Non-linearity & hysteresis: max. ±0.25% FSS
- Data transfer via USB without external power supply
- CAN bus, LAN and RS232 versions available
- Sampling rate per channel up to max. 50Hz
- Software and driver for LabVIEW and DBC files are included

General Description

The PSC pressure scanners are capable of measuring multiple pressure signals simultaneously. Temperature-compensated transducers feature high accuracy and minimal offset drift. In all devices each pressure channel range can be customized individually according to customer specifications.

The PSC24 has 24 pressure channels. Reference pressure lines of all sensors are connected to a single pressure port in standard configuration. A special differential version with reference ports for each line is also available.

The data is transmitted as ASCII text in the unit Pascal [Pa]. The transmission rate can be set in the range between 1 and 50 Hz.

A tare function can be triggered either by pressing the TARE button or by a software command.

Power for PSC devices equipped with USB or CAN interface is supplied via USB or respectively via CAN-port. For the version with built-in magnetic valves and LAN interface an external power supply (9-24 V, 1 A) has to be connected with the device.

All PSC versions are equipped with an USB interface, allowing easy configuratio. When connected via USB the pressure scanner identifies itself to the host PC as virtual COM port. Thus, any software supporting serial protocols can be used for communication. The LAN-version sends the data using the TCP-IP protocol. A direct connection can be set up via Telnet (Port 10001).

A recording software and an example program in LabVIEW (source code) are shipped with the device. For devices with CAN bus interface a DBC-file is included in the shipment.

On request there are different customization options:

- selection of different sensor pressure ranges
- parallel connection of sensors with different ranges for application where high accuracy is required

PSC8 • PSC16 • PSC24 Pressure Scanner
Datasheet

Technical Specifications

Measurement Range			Max. Proof Pressure		Availability
kPa	mbar	Bereich	kPa	bar	
0,125	100	uni/bi	200	0,25	
0,25	2.5	uni/bi	25	0.25	
0,5	5.0	uni/bi	25	0.25	
1,25	12.5	uni/bi	50	0.50	
2,5	25	uni/bi	50	0.50	
5,0	50	uni/bi	50	0.75	
7,5	75	uni/bi	50	1.20	
15	150	uni/bi	50	1.20	
≥34	≥340				On request
Accuracy and scan rates					
Nonlinearity & Hysterese		max. ±0.25% FSS			
Scan rate per channel		1-50 Hz (PSC8: 100Hz)			
Power supply					
via USB		USB-powered (no additional power supply required)			
PSC-LAN / PSC-CAN		7-24 V, 50 mA			
Environmental conditions					
Temperature		5° C…50° C			
Humidity		0…95%, non-condensing			
Operating medium		Air and non-corrosive gases			
Dimensions					
Housing (standard)		130 x 55 x 170 mm (B x H x T)			
Pressure connectors		hose nozzles D = 2,0 mm			
Recommended tubes		Soft-PE and silicone tubes 1.5 x 3.5 mm			
Software and drivers					
Virtual COM-Port-Driver					
Configuration software					
LabVIEW-example program as sourcecode					
Supported operation systems					
Windows XP, 7, 8, 10, Linux					
Options					
All PSC systems can be optionally equipped with CAN bus, LAN or RS232					

SVMtec GmbH | Bergnelkenstraße 7 | 70563 Stuttgart | Germany | www.svm-tec.de
contact: +49 (0)711 391867-0 | info@svm-tec.de
Version date: 09.10.2020

Serial Interface

The virtual COM port can be operated at any baud rate. We recommend 19200, 8 data bits, no parity, 1 stop bit. DTR (Data Terminal Ready) must be asserted.

Command	Function	Answer
`CAL a x`	Set scaling factor for sensor a to value x	`#Scaler=… Offset=…`
`CAL? A`	Read scaling factors for sensor a	`#Scaler=… Offset=…`
`EE_LOAD`	Load calibration data from EEPROM	`#EEPROM:loaded`
`EE_SAVE`	Save calibration data to EEPROM	`#EEPROM:saved`
`*IDN?`	Read device ID	`#PSC24-LAN 2.4.0 #SN35000`
`RATE x`	Define sample rate range x = 20 …5000 [ms] standard: 1000 [ms] → 1 [Hz]	`#Rate=x ms` `#Error: Rate-Range`
`RATE 0`	Activate request and trigger mode actual values are read only after manual command "?" is sent	`#Request-Mode active`
`?`	Read actual value (request-mode only)	
`*RST`	Load default settings	`#RESET`

`SCAN_A x`
`SCAN_B x`
`SCAN_C x`
	Defines a scanlist (channel selection)
	binary, each bit represents one channel	

`TARA`	Zero adjustment for all sensors	`#TARA`
`FILTER x`	Activate exponential filter 0 = deactivated; >0 = filter ranage in ms	`#FILTER=x`
Every command is terminated by a line break (CR, LF or CR+LF). The sensor enumeration of all devices starts at 1.		

-for CAN bus version only-		
`CAN_ID x`	Set CAN-ID	`#OK`
`CAN_IT x`	Set interface x = 0: normal (11 bit, CAN 2.0A) x = 1 extended 23 bit (23 bit, CAN 2.0B)	`#OK`
`CAN?`	Request CAN configuration	`#ID:0x[…]_Speed:[baud]_IDT:[0,1]`
`CAN_Speed x`	Set CAN bus rate 0: 125 kBaud 1: 250 kBaud 2: 500 kBaud 3: 1 MBaud	`#OK`

SVMtec GmbH | Bergnelkenstraße 7 | 70563 Stuttgart | Germany | www.svm-tec.de
contact: +49 (0)711 391867-0 | info@svm-tec.de
Version date: 09.10.2020

Technical Drawing

Dimensions for a PSC24 device can be taken from the following drawing.

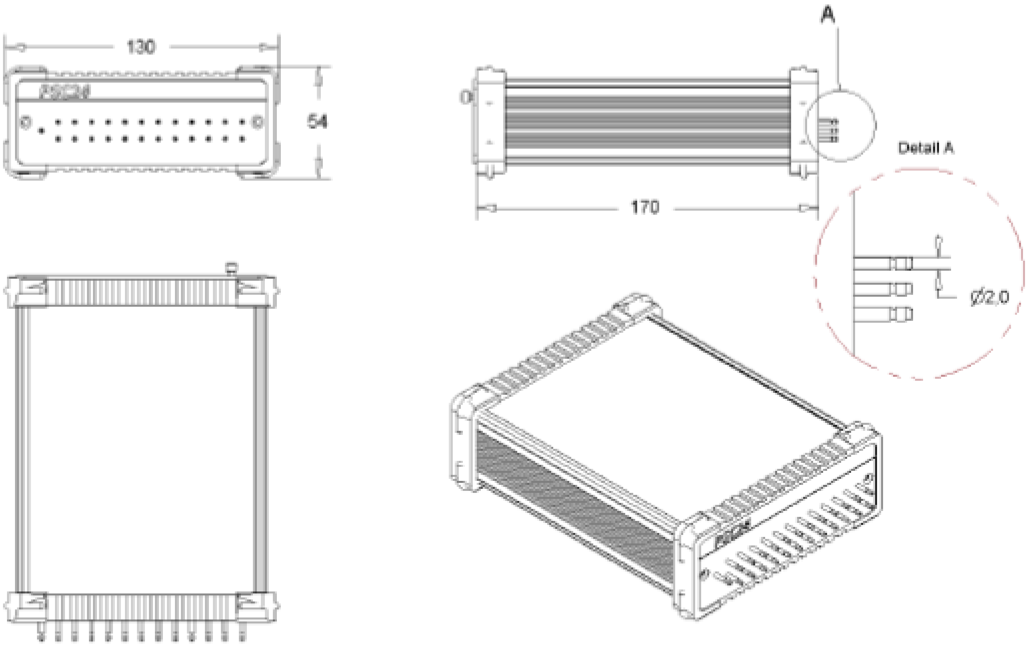

Figure: technical drawing and dimensions for a PSC24 pressure scanner.

SVMtec GmbH | Bergnelkenstraße 7 | 70563 Stuttgart | Germany | www.svm-tec.de
contact: +49 (0)711 391867-0 | info@svm-tec.de
Version date: 09.10.2020

APPENDIX 7: Sample calculation of Yaw, Pitch and Roll for multi-hole probes

Roll	20																
YAW with reference to wind tunnel - Conical Angle	0	10	20	30	40	45	50	60	70	80	90	100	110	120	130	140	150
V=	10	10	10	10	10	10	10	10	10	10	10	10	10	10	10	10	10
u=	10.00	9.85	9.40	8.66	7.66	7.07	6.43	5.00	3.42	1.74	0.00	-1.74	-3.42	-5.00	-6.43	-7.66	-8.66
a=	0.00	1.74	3.42	5.00	6.43	7.07	7.66	8.66	9.40	9.85	10.00	9.85	9.40	8.66	7.66	6.43	5.00
v=	0.00	1.63	3.21	4.70	6.04	6.64	7.20	8.14	8.83	9.25	9.40	9.25	8.83	8.14	7.20	6.04	4.70
w=	0.00	0.59	1.17	1.71	2.20	2.42	2.62	2.96	3.21	3.37	3.42	3.37	3.21	2.96	2.62	2.20	1.71
b=	10.00	9.87	9.47	8.83	7.97	7.47	6.94	5.81	4.69	3.79	3.42	3.79	4.69	5.81	6.94	7.97	8.83
BETA	0.00	9.39	18.75	28.02	37.16	41.64	46.04	54.47	62.01	67.73	70.00	112.27	117.99	125.53	133.96	142.84	151.98
ALPHA	0.00	3.45	7.10	11.17	16.01	18.88	22.18	30.64	43.22	62.73	90.00	-62.73	-43.22	-30.64	-22.18	-16.01	-11.17

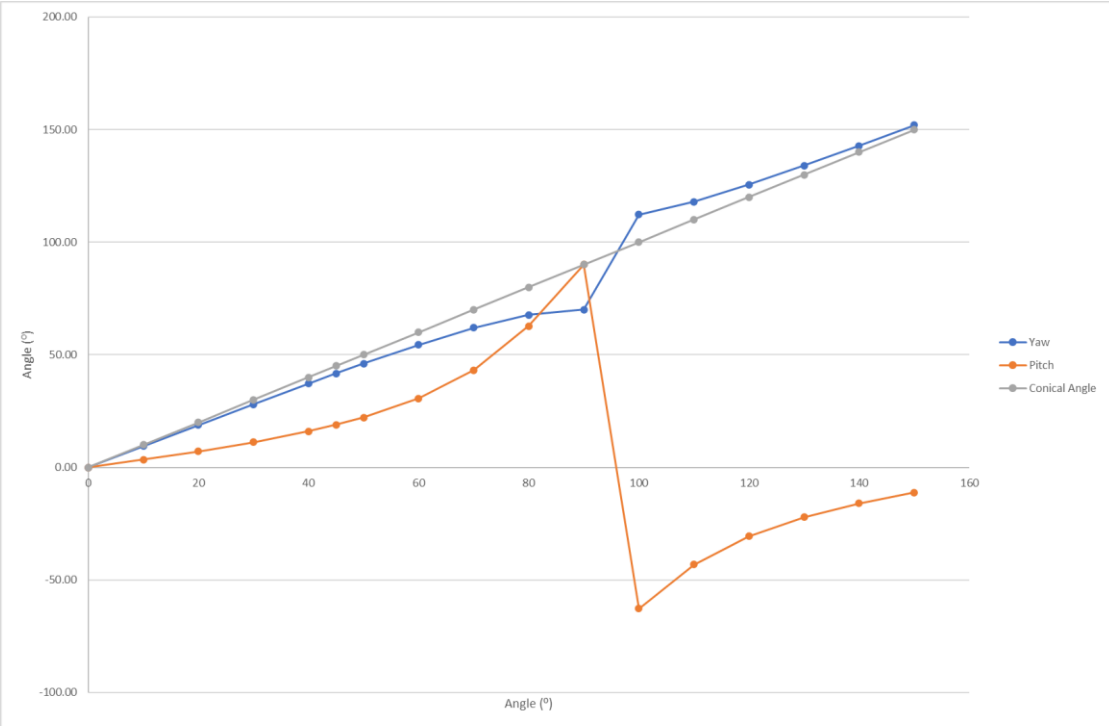

Figure 87: Roll fixed at 20º Yaw varied from 0º to 140º

APPENDIX 8: Sample of measurement results using Omniprobe

Date;7.7.2023
Time;11:30:31
Settling Time [s];0.000
Acquisition Time [s];10.000
Acquisition frequency [Hz];10
Serial number;S_14HP_k6t78k
Pressure channels;_A_chn01;_A_chn02;_A_chn03;_A_chn04;_A_chn05;_A_chn06;_A_chn07;_A_chn08;_B_chn01;_B_chn02;_B_chn03;_B_chn04;_B_chn05;_B_chn06
Reference pressure channel;(none)
Temperature channel;(none)
Calibration files;c:\Users\manqels\OneDrive\Research_June 2022\Wits\2022-03-28_S_14HP_k6t78k_1_M_0045.cal;c:\Users\manqels\OneDrive\Research_June 2022\Wits\2022-06-08_S_14HP_k6t78k_1_M_0100.cal
Traverse name;(none);(none);(none)

t [ms]	P1 [Pa]	P2 [Pa]	P3 [Pa]	P4 [Pa]	P5 [Pa]	P6 [Pa]	P7 [Pa]	P8 [Pa]	P9 [Pa]	P10 [Pa]	P11 [Pa]	P12 [Pa]	P13 [Pa]	P14 [Pa]	Theta [deg	Phi [degre	Alpha [deg	Beta [degr	Vmag [m/s	u [m/s]	v [m/s]	w [m/s]
0	-14.05	-12.15	33.98	35.3	-26.77	-15.38	-15.56	-27.91	-14.62	-15.94	-15	-14.8	-15.57	-14.61	23.03	-46.07	-17.02	15.75	10.45	9.62	2.84	-2.94
100	-13.67	-11.96	33.79	35.3	-26.77	-15.38	-15.56	-27.53	-14.62	-15.56	-15.19	-14.8	-15.19	-14.42	22.9	-46.01	-16.9	15.68	10.45	9.62	2.82	-2.93
200	-13.67	-11.2	34.74	35.86	-26.77	-15.19	-15.94	-27.53	-14.05	-15.56	-15	-14.61	-14.24	-14.04	23.06	-46.47	-17.15	15.65	10.5	9.66	2.83	-2.98
300	-13.67	-11.2	34.74	35.86	-26.77	-15.19	-15.94	-27.53	-14.05	-15.56	-15	-14.61	-14.24	-14.04	23.06	-46.47	-17.15	15.65	10.5	9.66	2.83	-2.98
400	-13.67	-11.77	33.79	34.92	-26.39	-15	-15.56	-27.53	-14.43	-15.56	-15	-14.42	-15	-14.8	22.94	-46.3	-17.01	15.62	10.4	9.58	2.8	-2.93
500	-13.67	-11.77	33.79	34.54	-26.39	-15.38	-15.56	-27.72	-14.81	-15.94	-15.57	-14.99	-15.19	-14.61	22.77	-46.67	-16.98	15.4	10.41	9.6	2.76	-2.93
600	-13.29	-11.77	34.17	35.3	-26.39	-15.38	-15.56	-27.72	-14.62	-15.94	-15.76	-14.8	-15.19	-14.61	22.73	-46.38	-16.87	15.46	10.45	9.64	2.79	-2.92
700	-13.1	-11.77	33.98	35.3	-26.01	-15.38	-15.18	-27.53	-14.05	-15.56	-15	-14.61	-15	-14.04	22.59	-47.94	-17.17	14.91	10.4	9.6	2.68	-2.97
800	-13.1	-11.77	34.17	34.92	-26.2	-15.95	-15.37	-27.53	-14.43	-15.94	-15.19	-14.61	-15	-14.04	22.69	-46.84	-16.96	15.3	10.43	9.62	2.75	-2.93